UNIVERSITÀ DI PAVIA

Dipartimento di Scienze della Terra e dell'Ambiente

eurac research

Istituto per l'Osservazione della Terra

SCUOLA DI ALTA FORMAZIONE DOTTORALE

Dottorato di Ricerca in Scienze della Terra e dell'Ambiente

Bertone Aldo

Slow movements in alpine terrains analysed combining different technologies: SAR interferometry, UAV-based remote sensing and GPS measurements

Anno Accademico 2018-2019
Ciclo XXXII

Coordinatore

Prof. Roberto Sacchi

Tutor:

Prof. Roberto Seppi

Co-tutors:

Dott. Mattia Callegari

Prof. Francesco Zucca

December, 2019

Doctoral thesis in Earth and Environmental Science.

Primary Institution:

University of Pavia, Department of Earth and Environmental Science. Pavia (Italy)

Secondary Institution:

EURAC research, Institute for Earth Observation. Bolzano (Italy)

Supervisors:

Roberto Seppi, University of Pavia

Mattia Callegari, EURAC research

Francesco Zucca, University of Pavia

Academic year 2018/2019

Abstract

Rock glaciers are the most visible geomorphological evidence of permafrost in mountain regions, frequently shaping the high-relief landscape. Active landforms show downslope displacement due to the creeping of permafrost, with surface speed ranging from a few centimetres to some meters per year. In the last decades, a considerable acceleration has been observed on many rock glaciers of the Alps, with several examples of destabilization and collapse, causing in some circumstances potential geomorphological hazards. The kinematic behaviour of rock glaciers is mainly controlled by climate variables and their recent acceleration has been attributed to a change in the climate-related drivers. Therefore, in a perspective of climate change, investigating the rock glaciers activity at large spatial scale (i.e. at the scale of mountain range) possibly combining different in-situ and remote sensing techniques is required for understanding the response of these high mountain geosystems.

In this thesis, the kinematics of rock glaciers is analysed at two different spatial scales, from regional to site-specific, and combining remote, proximal and in-situ sensing techniques.

The activity of rock glaciers at regional scale was investigated through satellite remote sensing, able to provide large spatial coverage. To this end, the freely available Sentinel-1 Synthetic Aperture Radar (SAR) images were used, developing two unsupervised and replicable methods to distinguish moving (i.e. with detectable displacement) and no-moving (i.e. without detectable displacement) landforms. These methods were developed and tested in a large area of the Eastern European Alps (South Tyrol and Trentino), where rock glaciers were already mapped and inventoried. The first method exploits the SAR interferometric coherence and, out of the 1665 rock glaciers mapped in South Tyrol, enabled to classify 270 landforms as moving and 1314 as no-moving. The second method exploits two well-known multitemporal interferometric techniques (Persistent Scatter and Small Baseline Subset), classifying 144 landforms as moving and 1165 as no-moving. Depending on them constrains, the two methods were able to classify 95% and 79% of the inventoried rock glaciers in South Tyrol, respectively. Thanks to the wide availability of Sentinel-1 imagery, these two powerful tools could be applied on any alpine area where rock glaciers are already mapped but their activity is not defined.

At a site-specific scale, the kinematic behaviour of an active rock glacier located in Val Senales (South Tyrol) was investigated at different time scales (from interannual to hourly), exploiting in-situ, proximal and remote sensing techniques such as GPS, UAV, Ground-Based and satellite SAR. On an interannual basis, a slight velocity decrease (from about 3.3 mm/d to about 2.7 mm/d) was observed between 2016-2017 and 2017-2018. An increase in velocity was observed on a seasonal basis, i.e. from early summer to late summer/early autumn 2017 and 2018. Ground-Based SAR, which for the first time was used to study the movement of a

rock glacier, revealed an hourly “step-like” pattern of the cumulative movement, which occurs in particular periods of few hours, separated by periods with no displacement. Advantages and limitations of each technique were discussed, revealing that the combination of different techniques is crucial to increase the robustness of results. In this study site, the main environmental variables were collected during the investigation period to investigate their role in the dynamic response of the rock glacier. The results were not conclusive, suggesting that a longer-term monitoring is essential to better understand the role of environmental drivers in the short-term rock glacier dynamics.

Contents

Summary

Chapter 1

Introduction

1.1 Background and motivations

In alpine areas, slope instability is a phenomenon related to superficial landslides, deep-seated gravitational slope deformations (DGSD) and permafrost creep (i.e. rock glaciers). The systematic observation of changes over time caused by the slope movements is of high importance for a proactive management of the natural hazards related to these phenomena. It allows making prediction on the evolution of the phenomena that can be used for defining risk scenario especially when urban areas and infrastructures (e.g. roads, cable cars, etc.) are involved. In addition, as also pointed out by the IPCC (Intergovernmental Panel on Climate Change), permafrost is recognized to be an important natural sensor of the climatic variability and thus an evident expression of the climate change ("Summary for Policymakers — Special Report on the Ocean and Cryosphere in a Changing Climate," 2019). Therefore, the observation and monitoring of permafrost creep, may give new insights on the current impact of changing climate conditions.

Permafrost includes all the ground which remains at or below 0 °C for at least two consecutive years (Van Everdingen, 1998). In mid-latitude mountain regions such as the European Alps, permafrost is patchy or discontinuous above 2200-2400 m a.s.l., while it can be continuous above 3500 m a.s.l. (Barsch, 1996). Its presence and thickness strongly depends on local microclimatic conditions, which are mainly controlled by elevation, slope exposure, and snow distribution. Permafrost is present below an active layer, defined as the top layer of the soil that thaws during summer and freezes again in winter (Burn, 1998). Alpine permafrost has a thickness typically ranging from 50 to more than 100 meters and it extends from the bottom of the active layer to the permafrost base, where the geothermal heat flow brings the temperature of the soil above 0 °C (Barsch, 1996).

Rock glaciers are the most visible geomorphological evidence of permafrost in mountain regions, frequently shaping the high-relief landscapes (Berthling, 2011; Haeberli et al., 2006). Berthling (2011), defined rock glaciers as "the visible expression of cumulative deformation by long-term creep of ice/debris mixtures under permafrost conditions". These landforms display frontal and lateral slopes, and often ridges and furrows on the surface (Barsch, 1992; Haeberli, 1985; Haeberli et al., 2006). Depending on their permafrost content and movement, rock glacier are typically classified into three different classes (e.g. (Barsch, 1996)): (i) active rock glaciers, in which the internal deformation and shear processes of internal ice produce a detectable surface displacement; (ii) inactive rock glaciers, still containing ice but without displacement; and (iii) relict rock glaciers, without internal ice and consequently with no movement. Active landforms are affected by

downslope displacement due to the creeping of permafrost, with surface speed rates ranging from a few centimetres to some meters per year (Delaloye et al., 2010). Seasonal and sub-seasonal velocity variations have been investigated for some rock glaciers (Kenner et al., 2017; Wirz et al., 2016), detecting the minimum velocity during the spring and maximum velocity in autumn. Interannual velocity variations are related with climatic variables such as air temperature, while sub-seasonal displacement variations are related with shorter time-scale events such as rainfall, snow melting and other environmental factors (Delaloye et al., 2010; Kääb et al., 2007; Kellerer-Pirklbauer et al., 2018; Kenner et al., 2017).

The study of rock glaciers is a very important task for several reasons. In the last decades, a considerable acceleration has been observed on many rock glaciers of the Alps (Bosson and Lambiel, 2016; Delaloye et al., 2010; Kenner et al., 2019; Kenner and Magnusson, 2017; Seppi et al., 2019), with several examples of destabilization and collapse of the landforms, causing in some circumstances potential geomorphological hazards (Bodin et al., 2017; Delaloye et al., 2012; Lugon and Stoffel, 2010; Marcer et al., 2019; Scotti et al., 2017; Vivero and Lambiel, 2019). Since rock glaciers respond sensitively to climate forcing, their recent acceleration has been attributed to a change in the climate-related drivers (Kääb et al., 2007). Therefore, in a perspective of climate change, investigating the rock glaciers activity at large spatial scale (i.e. at the scale of mountain range or wider) is becoming increasingly relevant for the management of high mountain geosystems. Over large areas this information can be included in rock glacier inventories and can support to answer the “where” question in hazard assessments (Alcántara and Goudie, 2010). From a hydrological point of view, rock glaciers may act as ice storage features, which may play a significant role on the hydrological regime of high elevation river/stream catchments, especially in dry areas (Brighenti et al., 2019; Jones et al., 2019, 2018b, 2018a). In addition, rock glaciers control the pace of periglacial mountain landscape evolution and are geomorphological indicators of the occurrence of permafrost conditions, therefore they can be used as proxies for estimating paleo-permafrost extents.

The main topic of this PhD thesis is the analysis of the kinematics of rock glaciers, focusing on two main points: the first is the activity estimation of rock glaciers at a large scale, the second concerns the kinematic analysis of a specific rock glacier, including its seasonal pace and the relation with external drivers that influence its velocity variations. The study area is located in the South Tyrol (Italy), an Alpine region located in the Eastern European Alps. The thesis was conducted in the framework of the project ALPSMOTION (ALPine Slow slope Movement moniTorIng and detectiON with remote and proximal sensing), which funded the PhD activities. The project was coordinated by Eurac Research, Bolzano (Institute for Earth Observation) and funded by the Autonomous province of Bolzano “Ripartizione Diritto allo Studio, Università e Ricerca Scientifica”.

The main aim of the ALPSMOTION project was to develop a cost-effective and automatic methodology for applying SAR interferometry to detect and measure slope movements over the non-vegetated areas of the

South Tyrol region. This first objective was addressed thanks to the new open data Sentinel-1, the C-band SAR sensor that has been launched in orbit by the European Space Agency (ESA) in April 2014. The second aim of the project was to develop a method that integrates different kind of sensors and techniques for measuring the slope movements with high precision in specific areas. This second aim focused on two different test sites in South Tyrol, i.e. the Corvara landslide in Badia Valley and the Lazaun rock glacier in Schnals Valley. The availability of other SAR data, such as X-band Cosmo-SkyMed and TerraSAR-X, were exploited for a proper integration of the Sentinel-1 data in these two test sites in order to overcome some of the limitations of the single sensor SAR interferometry approach. In addition to SAR data, field measurements were conducted in both sites, validating and integrating the products resulting from interferometry. These measurements included 1) the use of feature tracking techniques applied to UAV (Unmanned Aerial Vehicle) optical images, 2) the use of a ground-based Ku-band SAR and 3) topographic measurements with total stations and GPS.

1.2 State of art for the analysis of rock glacier activity

This section presents a brief overview of the methods and techniques available for monitoring the kinematic of rock glaciers. These techniques can be divided in three main categories: in-situ direct measurements, proximal sensing techniques and remote sensing techniques.

In-situ direct measurements are conducted using ground-based topographic instruments such as Global Positioning System (GPS) and total station (Buchli et al., 2018; Delaloye et al., 2010; Kenner et al., 2017; Seppi et al., 2019; Strozzi et al., 2010; Wirz et al., 2016). Topographic total station and GPS surveys provide very accurate displacement information of the investigated survey points. However, the displacement information can be obtained only for the surveyed points and a large and well-distributed number of points is required for obtaining an adequate spatial coverage. The temporal resolution is low because frequent (e.g. weekly or monthly) field surveys are not feasible in these environments. The velocity variations of rock glaciers have been recently investigates at high time resolution with continuous GPS monitoring systems (Kenner et al., 2019, 2017; Wirz et al., 2016), which are however often expensive and difficult to install, and record data only at single points

The Image Cross-Correlation (ICC) technique, applied to multitemporal high resolution orthophotos or Digital Terrain Models (DTMs), is able to partially solve the limitations of the in-situ measurements (Groh and Blöthe, 2019; Kaab, 2000; Kääb et al., 2003; Roer et al., 2008; Strozzi et al., 2010, 2004). This technique is able to detect surface displacements using laser scanner or photogrammetric data (Bauer et al., 2003; Westoby et al., 2012), which can be acquired from the ground, airplane or Unmanned Aerial Vehicles (UAV). Another proximal sensing technique used to detect surface displacement in high elevation areas is the Terrestrial

Radar Interferometry (TRI). This technique, derived from the satellite technology, is able to acquire radar images with a very high frequency, providing displacement information with very high time resolution and thus overcoming the drawback of the large revisit period of satellite platforms (Buchli et al., 2018; Monserrat et al., 2014; Riesen et al., 2011). Overall, the main limitation of proximal detection techniques is that they can only be applied on small areas and in selected time periods, reducing the number of investigable landforms.

Earth Observation (EO) satellite data represent a promising tool to analyse the rock glacier kinematics combining large spatial coverage and high temporal resolution, without having to carry out field campaigns. Several methods using satellite Synthetic Aperture Radar (SAR) data, alone or in combination with optical data, were developed in the last decades (Barboux et al., 2015; Kenyi and Kaufmann, 2003; Lambiel et al., 2008; Necsoiu et al., 2016; Strozzi et al., 2004). For example, landforms characterized by surface displacement can be analysed by supervised analysis of data exploiting Differential Interferometry (DIn-SAR) (Barboux et al., 2015; Liu et al., 2013; Strozzi et al., 2004; Villarroel et al., 2018; Wang et al., 2017). As a support to SAR, optical data are frequently used to define the type of investigated landforms (e.g. rock glaciers, debris-covered glaciers, push moraines) (Villarroel et al., 2018). However, SAR products are affected by some limitations that should be properly taken into account. These are decorrelation effects caused by the terrain conditions (e.g. presence of snow, vegetation cover), as well as atmospheric artefacts and issues related to the complex topography of the investigated areas (Bamler and Hartl, 1998; Barboux et al., 2014; Klees and Massonnet, 1998).

1.3 Objectives and methods

The overall objective of this thesis was the study of the rock glacier kinematics, according to the objectives given by the ALPSMOTION project. The study area is the South Tyrol Region (Italy), where a large number of rock glaciers have been already mapped within an existing inventory (Mair V., Zischg A., Krainer K., Stötter J., Zilger J., Belitz K., 2008). The objective was achieved by using in-situ measurements, proximal sensing techniques and remote sensing techniques, trying to combine the high accuracy of direct ground observations with the wide spatial coverage and high frequency of proximal and remote sensing data.

In detail, the study was aimed at achieving two main objectives, with different temporal and spatial scales.

The first one was to investigate the activity of rock glaciers at the regional scale. The rock glacier inventories recently compiled in the European Alps only partially provide the activity information and lack displacement estimations at large scale (Colucci et al., 2016; Cremonese et al., 2011; Krainer and Ribis, 2012; Mair V., Zischg A., Krainer K., Stötter J., Zilger J., Belitz K., 2008; Scotti et al., 2013; Seppi et al., 2012). Over large areas, understanding the activity of each rock glacier and distinguishing between active landforms (characterized

by displacement) from those without displacement (inactive and relict landforms) is often complicated. The key to solve this gap is possibly a remote sensing approach, and in particular the satellite-based imagery that provide good spatial coverage. Therefore, the first objective of this thesis was the development of new methods to classify the rock glaciers activity over large areas using remote sensing techniques. Two SAR-based, unsupervised, replicable, and quite simple methods to describe the activity of rock glaciers over large areas were proposed, both able to distinguish moving (i.e. with detectable displacement) and no-moving (i.e. without detectable displacement) landforms. The first method exploits the interferometric coherence of SAR images, the second is based on the multitemporal interferometric SAR techniques. The information extracted from these methods were used to update the activity information within the existing rock glacier inventory of South Tyrol.

The second objective of this thesis was to investigate the kinematic behaviour of a specific rock glacier located in South Tyrol, at different temporal scales. The internal structure of this rock glacier is well known thanks to geophysics and drilling conducted in the last years (Krainer et al., 2015), but its flow pattern is still poorly investigated. In literature, interannual and sub-seasonal rock glacier velocity variations are often investigated exploiting several techniques, e.g. GPS, photogrammetry, terrestrial laser scanner (TLS) and radar (Bosson and Lambiel, 2016; Buchli et al., 2018, 2013; Delaloye et al., 2010; Ikeda et al., 2008; Kääb et al., 2005; Kenner et al., 2019, 2017; Roer et al., 2005; Wirz et al., 2016). The kinematic behaviour of this specific rock glacier was investigated exploiting in-situ measurements, proximal sensing techniques and remote sensing techniques. The results of these different approaches were combined and cross-compared in order to increase their robustness. Furthermore, some environmental variables were investigated in order to understand their possible relations with the rock glacier surface velocity variations.

1.4 Outline of the Thesis

The thesis is structured into two main parts. Chapters 2 describes two methods developed to reach the first objective of this thesis, i.e. the definition of the rock glacier activity at the regional scale. In particular, one method was developed exploiting the interferometric coherence of SAR images and one method was developed using the multitemporal interferometric SAR techniques. Chapter 3 describes the methods that have been developed to reach the second objective of this thesis, i.e. the analyses of the kinematic behaviour of a specific rock glacier over different temporal scales, and the obtained results. In detail, in-situ measurements, proximal sensing techniques and satellite remote sensing techniques where used to analyse the kinematic variations, as well as the possible interactions with the environmental variables influencing the kinematic behaviour. Chapter 4 is dedicated to the general conclusions.

Chapter 2

Unsupervised methods to detect rock glacier activity by using Sentinel-1 SAR images: a regional-scale study in the Eastern European Alps

This chapter is partially published in:

Bertone, A.; Zucca, F.; Marin, C.; Notarnicola, C.; Cuozzo, G.; Krainer, K.; Mair, V.; Riccardi, P.; Callegari, M.; Seppi, R. An Unsupervised Method to Detect Rock Glacier Activity by Using Sentinel-1 SAR Interferometric Coherence: A Regional-Scale Study in the Eastern European Alps. *Remote Sens.* **2019**, *11*, 1711.

2.1 Introduction

Many rock glacier inventories have been recently completed in the European Alps (Colucci et al., 2016; Cremonese et al., 2011; Krainer and Ribis, 2012; Mair V., Zischg A., Krainer K., Stötter J., Zilger J., Belitz K., 2008; Scotti et al., 2013; Seppi et al., 2012). They contain the rock glacier outlines, that are directly drawn from visual analysis of optical satellite images, aerial orthophotos, and Digital Terrain Models (DTMs), frequently checked with field surveys (Barsch, 1996; Blöthe et al., 2019; Falaschi et al., 2015; Onaca et al., 2017; Rangecroft et al., 2014; Roer and Nyenhuis, 2007). Furthermore, the activity information is frequently included in the inventories, distinguishing between active landforms (characterized by displacement) from those without displacement (inactive and relict landforms).

The identification of active rock glaciers within inventories is usually accomplished on the basis of geomorphological evidences (Colucci et al., 2016; Jones et al., 2018b; Roer and Nyenhuis, 2007). Quantitative information are generally obtained by direct measurements of surface displacement using ground-based or proximal sensing techniques (e.g. topographic, Global Positioning System and Terrestrial Laser Scanner surveys) (Buchli et al., 2018; Strozzi et al., 2010; Wirz et al., 2016). However, as rock glaciers are located in remote areas, direct measurements can be carried out only on a limited number of landforms. Even the application of remote sensing techniques such as Cross-Correlation on multi temporal, high resolution orthophotos and DTMs can be applied only on small areas or on selected time periods due to the limited availability of data (Kaab, 2000; Kääb and Vollmer, 2000; Monnier and Kinnard, 2017; Strozzi et al., 2004). Therefore, the detection of moving rock glaciers over wider areas (i.e. at a regional-scale) remains largely unresolved.

Earth Observation (EO) satellite data can represent an adequate tool to fill-up this gap of knowledge, especially with the increasing availability of high spatial and temporal resolution data over large areas. Satellite Synthetic Aperture Radar (SAR) platforms, thanks to their day-and-night and all-weather-conditions availability, may help to overcome the above-mentioned constraints. In fact several approaches exploiting SAR data, alone or in combination with optical data, were developed in the last decades (Barboux et al., 2015; Kenyi and Kaufmann, 2003; Lambiel et al., 2008; Necsoiu et al., 2016; Strozzi et al., 2004; Villarroel et al., 2018). For example, landforms characterized by surface displacements can be detected by supervised analysis of data exploiting Differential Interferometry (DIn-SAR) to detect phase variations related to the displacement (Barboux et al., 2015; Liu et al., 2013; Strozzi et al., 2004; Villarroel et al., 2018; Wang et al., 2017). As a support to SAR, optical data are frequently used to define the type of investigated landforms (e.g. rock glaciers, debris-covered glaciers, push moraines) (Villarroel et al., 2018). However, DIn-SAR products are affected by some limitations that should be properly taken into account. These are decorrelation effects caused by the terrain conditions (presence of snow, vegetation cover), as well as atmospheric artefacts and issues related to the complex topography of the investigated areas (Barboux et al., 2014). An adequate tool

to fill-up these limitations are the multitemporal interferometric SAR techniques, which provide the surface displacement maps exploiting a large number of SAR images to limit the atmospheric artefacts. However, the application of specific multitemporal SAR techniques in high mountain areas (Berardino et al., 2002; Ferretti et al., 2001) is often restricted, if not hampered, by the scarce number of suitable SAR images available in the snow-free period, which could be particularly short.

In this chapter, we propose two new SAR-based, unsupervised, replicable, and quite easy approaches to describe the activity of rock glaciers over large spatial areas, distinguishing moving and no-moving landforms. The methods were developed and tested on a wide mountainous area located in the Eastern European Alps, using Sentinel-1 SAR data.

The first method exploits the interferometric coherence information, and takes into account all the factors that may limit the effectiveness of the coherence in describing the rock glaciers activity. The original application of interferometric coherence, estimated using the rock glacier outlines as boundaries instead of regular kernel windows, was used as key indicator of displacement. This new approach is able to compensate for the drawbacks of existing methods based on subjective analysis of geomorphological evidences, providing additional information to the widely used interferometric approaches, such as the DIn-SAR technique.

The second method was developed exploiting the SAR multitemporal interferometric techniques. A large number of SAR images is not often available on mountain regions, because of the extended snow cover periods. However, starting from October 2016 for the first time of earth observation, Sentinel-1 A and B allow to acquire a sufficient number of SAR images during the snow-free periods, in order to apply multitemporal interferometric techniques. The obtained displacement information was used to classify the rock glaciers in moving (i.e. with detectable displacement) and no-moving (i.e. without detectable displacement). This new approach is able to compensate for the time-consuming analysis of the SAR products.

2.2 Materials and methods

2.2.1 Study area and dataset

The proposed methods were developed and tested over a mountainous area, encompassing the entire South Tyrol and the western part of Trentino (Italian Alps).

South Tyrol is located in the eastern Italian Alps (Fig. 2.1). A rock glacier inventory (South Tyrol Inventory – STI) was recently compiled in this region, considering only the area located above 1600 m a.s.l. (Mair V., Zischg A., Krainer K., Stötter J., Zilger J., Belitz K., 2008; Zischg et al., 2012). The landforms were identified and mapped using a LIDAR (Light Detection and Ranging) DTMs (2.5 m GSD, Ground Sample Distance) and orthophotos of different dates. Descriptive features, both numerical and qualitative, were associated to each

rock glacier, including a classification into active, inactive and relict forms. The inventory includes 1665 rock glaciers, 230 of them (14%) were classified by the authors as active, 198 (12%) as inactive, 1099 (66%) as relict, and 138 (8%) were not classified (Fig. 2.2a). Altitudinal and aspect distributions of active, inactive and relict rock glaciers are showed in figures 2.2b and 2.2c. The STI provided the landform outlines on which our analysis was developed. Moreover, the rock glaciers classification obtained by our methods were compared with the classification provided by the inventory.

In Trentino, a set of 57 rock glaciers extracted from an inventory (Seppi et al., 2012) (Fig. 2.1) was used to validate the method based on interferometric coherence (section 2.3.1), thanks to their activity status known from field observations (Seppi, 2019), direct measurements (Seppi et al., 2019) and visual analysis of multi temporal data. In detail, the visual analysis was conducted using high-resolution aerial orthophotos (2006 and 2014, 0.5 m and 0.2 m GSD, respectively) and LIDAR DTMs (2006 and 2013, 2 m and 0.5 m GSD, respectively); geomorphological evidences such as the general deformation of the landform and the visible movements of large blocks were evaluated as signs of displacement. As a result, 29 rock glaciers were classified as moving (i.e. exhibiting certain evidence of surface movement) and 28 as no-moving (i.e. lacking surface movement). Since the vegetation influences the effectiveness of our method based on interferometric coherence (see section 2.2.2), all the rock glaciers selected in Trentino were without vegetation cover. Over the South Tyrol, vegetated rock glaciers were recognized using a land cover map and excluded from the analysis ("Land Use Information System South Tyrol," n.d.).

Two Sentinel-1 tracks, i.e. relative orbit 117 (ascending) and 168 (descending), cover the entire study area since 2014 (Fig. 2.1a). The images are acquired in Interferometric Wide swath (IW) mode with a 250 km swath at 5 m by 20 m spatial resolution. Single Look Complex (SLC) product type and Vertical transmit Vertical receive (VV) polarization data were used for this analysis. The availability of both Sentinel-1A and 1B data ensure a temporal resolution of 6 days for each track. As the snow cover is a severe limitation for using satellite SAR data, our methods were developed to analyse the rock glaciers activity during the snow-free period. In detail, the method based on interferometric coherence was developed taking into account all the images from the beginning of August to the end of September 2017 (Fig. 2.3), while the method based on multitemporal interferometry techniques we used the images acquired during the summer 2017 from mid-June to mid-October 2017 (about 21 images, Fig. 2.3). A LIDAR-derived DTM ("South Tyrol Digital Terrain Model (DTM)," n.d.), with 2.5 m GSD was used to remove the topographic-related component during the SAR phase differences computation.

As additional independent dataset to evaluate the obtained results, we used a permafrost probability map available from the GLOBpermafrost project (Bartsch et al., 2016) (Fig. 2.1a). This dataset was produced by using satellite data, land cover information and ground surface temperature (Westermann et al., 2017), without considering the rock glacier location. Information on permafrost distribution at a global scale, with

a spatial resolution of 1 Km, are provided by a numerical index ranging from 0 to 1. The higher is the index, the higher is the probability that permafrost exists in a given area.

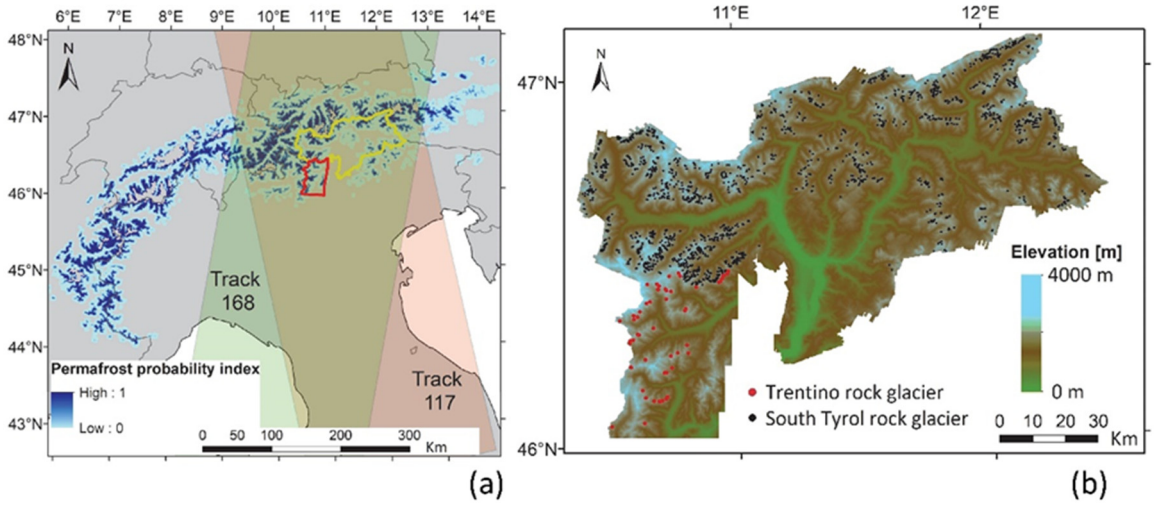

Figure 2.1: Geographical setting of the study area. (a) Area covered by the Sentinel-1 tracks 117 and 168, overlaid on the permafrost probability distribution on the entire Alps according to the index provided by the GLOBpermafrost project (Bartsch et al., 2016)*. The red and yellow lines represent the geographical outlines of the Trentino and South Tyrol, respectively. (b) Elevation map of the study area and distribution of rock glaciers (red and black dots).*

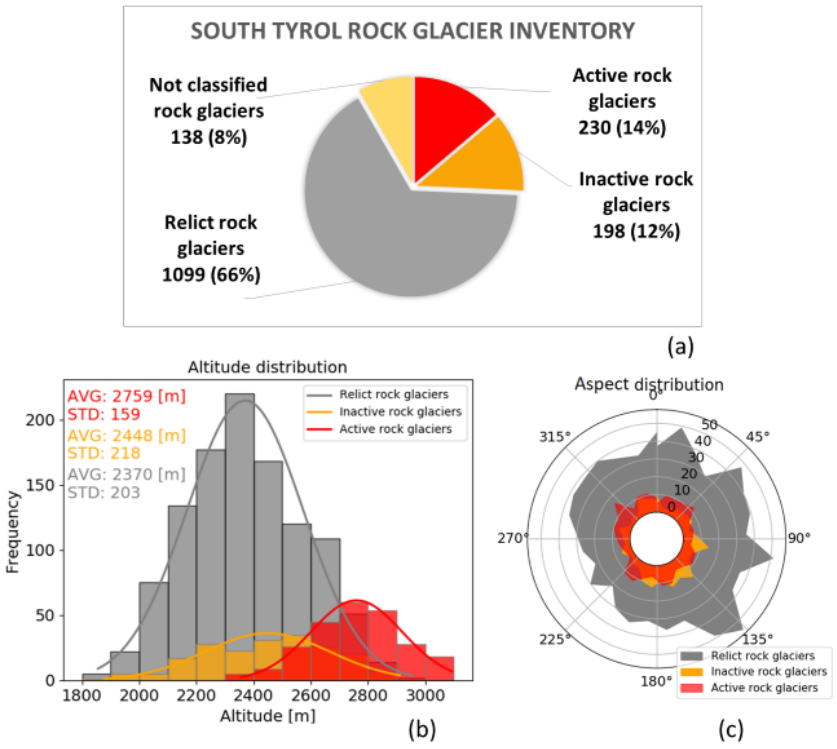

Figure 2.2: Summary data from the rock glacier inventory of South Tyrol (Mair V., Zischg A., Krainer K., Stötter J., Zilger J., Belitz K., 2008)*. (a) Percentage of active, inactive and relict rock glaciers; (b) altitudinal distribution; (c) aspect distribution. In figure (b) the average (AVG) and the standard deviation (STD) of the altitude for the three classes are shown.*

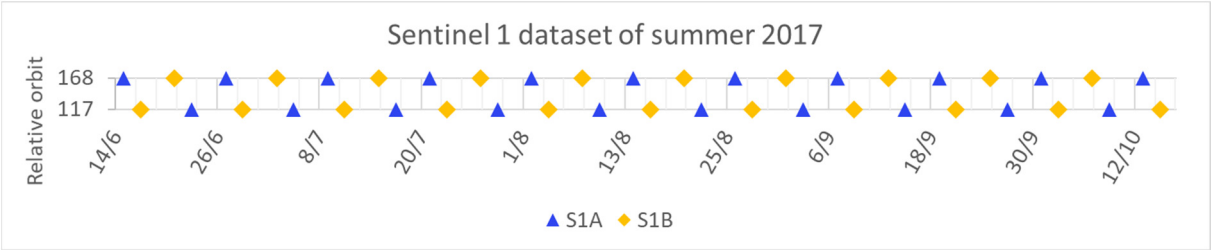

Figure 2.3: List of Sentinel-1 images acquired during the snow-free period of 2017.

2.2.2 Description of the method based on interferometric coherence

In order to fulfil the requirements of the activity classification of rock glaciers as envisaged in the former chapter (e.g. wide area, topographic issue, short snow-free period), we propose an original application of interferometric coherence as a key indicator of displacement, able to label a large number of rock glaciers with their activity features. For the purposes of our work and according to our exclusively kinematic approach, we adopted two classes of rock glaciers: (i) "moving" rock glaciers, i.e. those with displacement detectable by our method, and (ii) "no-moving" rock glaciers, i.e. those with no detectable displacement. This classification assumes to aggregate from a kinematic point of view the "inactive" and "relict" classes proposed by Barsch (Barsch, 1996) under the class "no-moving", and the "active" class under the class "moving", without considering the permafrost content.

The coherence is a measure of the similarity between a pair of images (i.e. master and slave) (Klees and Massonnet, 1998; Massonnet and Souyris, 2008; Moreira et al., 2013; Yague-Martinez et al., 2016). Although the coherence is usually estimated on regular kernel windows (Touzi et al., 1999), in this work we used the rock glacier outlines as boundaries to compute this value. This was done to avoid the average estimation of coherence and the consequent bias towards higher coherence values due to the introduction of small areas of calculation. Furthermore, in this way each rock glacier can be associated with a single SAR coherence value, representative of the entire area of the investigated landform. Low coherence values indicate low or no similarity between the images, and this may be due to (i) the presence of vegetation, (ii) changes of the target properties (i.e. changes of the physical ground conditions), (iii) changes of surface shape (i.e. displacement) (Corbane et al., 2018; Klees and Massonnet, 1998; Massonnet and Feigl, 1998; Necsoiu et al., 2016; Nolan and Fatland, 2003; Smith, 2002; Strozzi et al., 1999; Yague-Martinez et al., 2016). High coherence values indicate, instead, similarity between the images (i.e. no movement and no changes in the surface properties of the rock glacier). Low coherence values due to vegetation cover can be avoided excluding vegetated rock glaciers from the classification process, for example by means of a high-resolution land cover map.

To distinguish if a low coherence value between two images was related to the surface displacement or to a change in the physical properties of the ground (e.g. soil moisture changes due to rainfall or melt water from summer wet snowfalls), we used the intensity of the backscattering inside the rock glacier outline. Indeed,

the backscattering change between two images can be related to changes of (i) target shape, (ii) orientation or (iii) dielectric properties of the ground (Bergstedt et al., 2018; Massonnet and Souyris, 2008). Field and remote sensing observations demonstrated that the rock glacier displacements during the summer season is much lower than the resolution of Sentinel-1 images used in this work (20 m GSD) (Buchli et al., 2018; Necsoiu et al., 2016; Strozzi et al., 2010; Wirz et al., 2016). Therefore, assuming that changes in shape and orientation of the rock glaciers are much lower than the resolution of SAR images during the investigated period, the only source of backscattering change is the difference in the dielectric properties of the ground, which is mainly caused by changes in moisture due to rainfall or summer snowfalls (Bergstedt et al., 2018; Nagler and Rott, 2000). Backscattering information can therefore be used as key indicator to select the most suitable SAR images (i.e. without rainfall or summer snowfalls) on which to compute the coherence.

The overall scheme followed to develop the method is shown in figure 2.4, where the classification procedure is divided in three parts: the SAR data pre-processing, the data selection, the coherence calculation and the classification.

2.2.2.1 SAR data pre-processing

The Sentinel-1 SAR images acquired from the beginning of August to the end of September 2017 (Fig. 2.3) were multi-looked with a window size of 4 in azimuth and coregistered (Bamler and Hartl, 1998; Yague-Martinez et al., 2016). Then, backscattering images and layover and shadow masks were generated. All the possible pairs of images with temporal baselines of 6, 12, 18, 24, 30, 36, 42, 48 and 54 days were combined, and for each pair the phase difference was computed between a master and a slave image. Topographic corrections for the phase difference and backscattering, as well as geolocation of the data were accomplished using LIDAR DTM and Precise Orbit Auxiliary Files (Bamler and Hartl, 1998; Klees and Massonnet, 1998; Moreira et al., 2013; Tarayre and Massonnet, 1996; Yague-Martinez et al., 2016; Zebker et al., 1997). Datasets of images from two different relative orbits were available for the investigated area (i.e. relative orbits 117 and 168), providing different Line Of Sight (LOS). Therefore, the SAR data pre-processing was applied by computing backscattering, layover and shadow masks and phase differences for each relative orbit dataset.

2.2.2.2 Data selection

Depending on the rock glacier orientation, topographic effects such as layover and shadow can be reduced using a favourable satellite geometric view (i.e. ascending or descending) (Hu et al., 2014; Klees and Massonnet, 1998). Therefore, for each rock glacier the relative orbit dataset with the smallest layover and shadow areas and the largest number of SAR pixels inside the rock glacier boundary was selected for the classification procedure.

Rock glaciers covered by vegetation were excluded from the classification procedure. Over the South Tyrol this was accomplished using a land cover map (“Land Use Information System South Tyrol,” n.d.), which

includes the vegetation classes “grass”, “shrubs” and “wood”. In particular, we considered as vegetated the rock glaciers with more than 15% of the surface covered by at least one of these vegetation classes. As inactive and relict rock glaciers have no movement and are often densely covered by vegetation (Ikeda and Matsuoka, 2002; Strozzi et al., 2004), we assumed that the vegetated rock glaciers excluded from our classification are not in motion, and therefore they were added to the class of no-moving at the end of the classification procedure.

As small rock glaciers are more affected by decorrelation effects (Barboux et al., 2014) that reduce the reliability of coherence, we excluded those landforms with an area less than 80 SAR pixels from the analysis. Furthermore, also rock glaciers with a layover-shadow area larger than 50% of the total area were excluded. These thresholds were chosen as a trade-off between robustness, reliability of coherence estimation and number of excluded rock glaciers, i.e. non-classified.

In order to use the most suitable images to estimate the coherence, we selected for each rock glacier and for each temporal baseline one pair of images (i.e. master and slave) with the most similar mean backscattering values related to a reference SAR backscattering image acquired under dry meteorological conditions. To operate this selection, we identified periods with no snowfall and rainfall events using the precipitation and snow depth data collected by 17 weather stations distributed over the investigated area between 2000 m and 3200 m a.s.l. In this way, one reference backscattering image for each of the two relative orbits covering the investigated area was selected. In particular, the reference backscattering image acquired on 22nd August 2017 was chosen for the track 117, and the image acquired on 14th August 2017 for the track 168 (Fig. 2.3).

For each rock glacier, we computed the Sum of the Absolute Backscattering Differences (SABD) between the reference backscattering image and the master and slave images of each pair for any temporal baseline. The SABD was computed as follows (equation 2.1):

$$SABD = \left|10 \cdot \log_{10}\left(\frac{\langle I_r \rangle}{\langle I_m \rangle}\right)\right| + \left|10 \cdot \log_{10}\left(\frac{\langle I_r \rangle}{\langle I_s \rangle}\right)\right| \quad (2.1)$$

Where, inside the rock glacier outline, $\langle \mathrm{I_r} \rangle$ is the mean intensity value of backscattering of the reference image, and $\langle \mathrm{I_m} \rangle$ and $\langle \mathrm{I_s} \rangle$ are the mean intensity values of backscattering of the master and slave images, respectively. The lower the SABD value, the higher physical ground conditions similarity between the reference image and the pair of images. Then, for each rock glacier and for each temporal baseline, the pair of images with the lowest SABD value was selected to perform the coherence estimation.

2.2.2.3 Coherence estimation and rock glacier classification

For the selected pairs of images, the coherence was estimated for each rock glacier using their outlines as follows (Massonnet and Souyris, 2008) (equation 2.2):

$$CC = \left| \frac{\sum_{i=1}^{N} r_{1i} r_{2i}\, e^{j(\Delta\varphi_i)}}{\sqrt{\sum_{i=1}^{N} {r_{1i}}^2} \sqrt{\sum_{i=1}^{N} {r_{2i}}^2}} \right| \tag{2.2}$$

Where r_{1i} and r_{2i} are the amplitudes of the complex signals of the master and slave images at pixel *i* inside the rock glacier outline, $\Delta\varphi_i$ is the phase difference obtained at pixel *i* inside the rock glacier area, *N* is the number of pixels inside the rock glacier outlines. Therefore, one coherence value for each rock glacier and temporal baseline was estimated by using the selected pair of images.

Then, the unsupervised classification of rock glaciers was performed, labelling as "no-moving" the rock glaciers with high coherence values and as "moving" those with low coherence values. In particular, coherence values computed with long temporal baselines enabled to detect rock glaciers characterized by low movement rates, even if they are more affected by decorrelation effects unrelated with displacement (Barboux et al., 2014; Corbane et al., 2018; Klees and Massonnet, 1998; Lee et al., 2013; Massonnet and Souyris, 2008). On the contrary, coherence values computed with short baselines are less affected by decorrelation effects, but in this case small displacements are undetectable (Villarroel et al., 2018). To identify the activity of a rock glacier, all the temporal baselines need to be exploited during the classification. In our method, this is done by using all the coherence values as features for an unsupervised classification based on Bayesian inferencing, thus avoiding having to select arbitrary thresholds. In detail, the well-known Expectation Maximization algorithm (EM) (Gupta et al., 2011; Moon, 1996) was used as an iterative method to find the maximum likelihood estimates between moving and no-moving rock glaciers and select an adaptive decision threshold to minimize the overall classification error. Assuming that rock glaciers are spatially independent and that moving and a no-moving classes are represented by Gaussian distributions of the coherence values computed with different temporal baselines, the EM algorithm was applied for the activity classification (Fig. 2.5).

2.2.2.4 Validation and performance test

To validate the method and highlight the wrongly-classified rock glaciers, we compared the results of our classification with the set of rock glaciers from Trentino, whose activity status was previously defined (section 2.2.1). We computed confusion matrices, accuracies (i.e. percent of correctly classified rock glaciers with respect to the total number) and Kappa coefficient. The last one is a more robust measure than simple percent accuracy calculation, because it takes into account the possibility of the accuracy occurring by

chance. The coefficient ranges between 0 and 1, the higher the value, the higher is the quality of the classification. Good classifications have kappa coefficient higher than 0.6 (Pontius and Millones, 2011).

A large and suitable dataset of SAR images is not always available for high mountain regions, where the snow-free period can be very short. Therefore, in order to simulate the conditions of a region with an extended snow cover period, we tested the performance of our method on a shorter period, using Sentinel-1 images acquired in only one, snow-free month. We performed two separate tests, using images from August and September 2017; hence the maximum temporal baseline available was 24 days. As with the former complete dataset, the analysis was performed on the whole study area and the results were validated on the set of rock glaciers from Trentino.

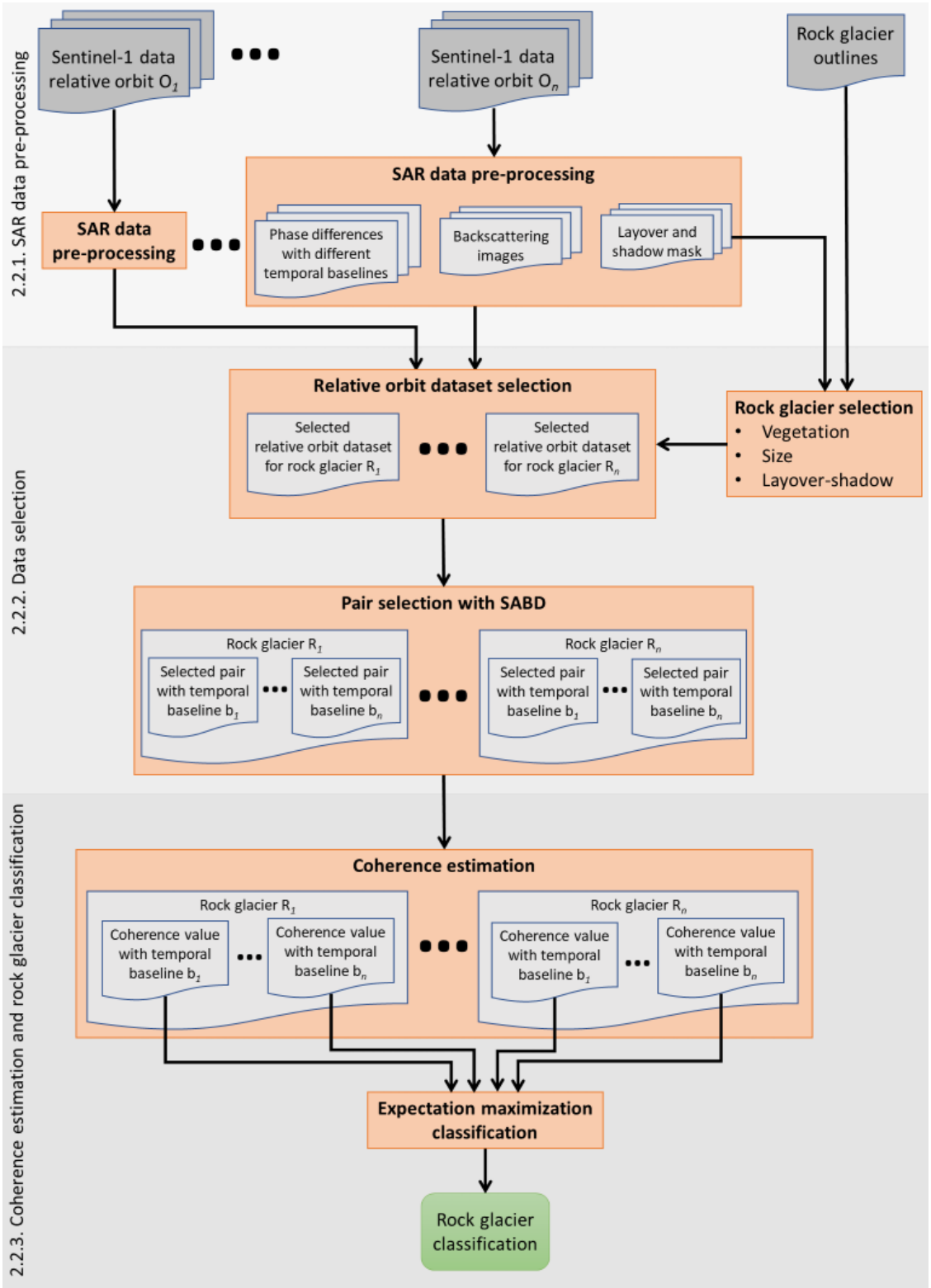

Figure 2.4: General block scheme of the rock glaciers classification. Pairs of Sentinel-1 images from different relative orbit were pre-processed to obtain backscattering, phase differences and layover-shadow mask, using different temporal baselines. Then for each rock glacier, the most favourable relative orbit dataset was used. Small or vegetated rock glaciers or with extended layover-shadow areas were discarded. For each rock glacier and for each temporal baseline the pair of images with the sum of the absolute backscattering difference of master and slave images close to zero was selected. Coherence is then estimated for the selected pairs of images. Then rock glaciers were classified by the expectation maximization algorithm using the coherence values estimated with different temporal baselines.

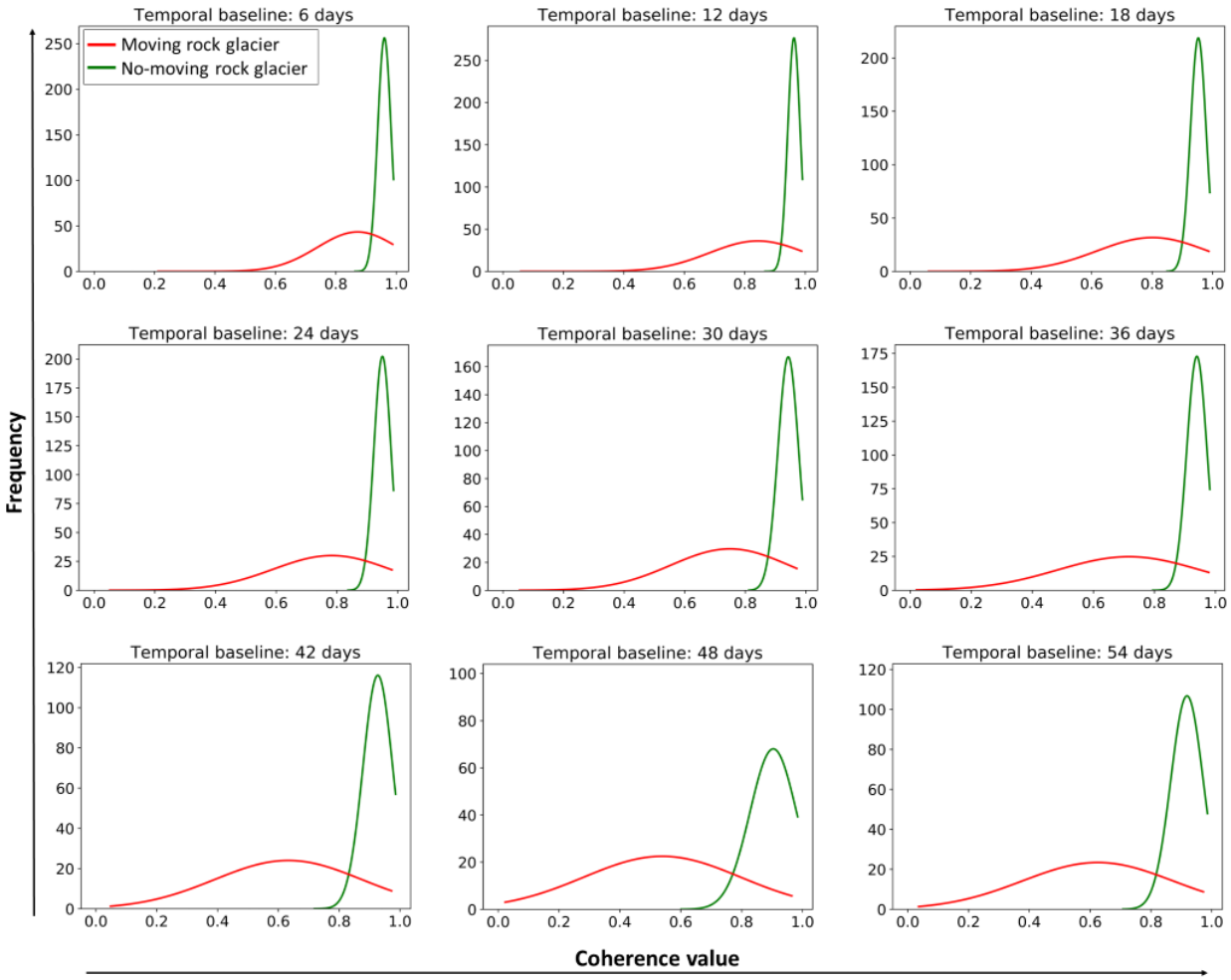

Figure 2.5: Gaussian distributions of the coherence values. The coherence values are showed by the x axis, the frequency values by the y axis. The Gaussian distribution of moving and no-moving rock glaciers obtained by the application of the EM algorithm are showed by red and green lines, respectively. Each graph shows the coherence distributions obtained with the same temporal baseline

2.2.3 Description of the method based on multitemporal interferometric techniques

Multitemporal interferometric techniques were used to compute surface displacement maps, from which to extract kinematic information to classify rock glaciers into “moving” and “no-moving” (as already proposed for the interferometric coherence approach).

The method was composed of several steps: generation of displacement maps, displacement maps evaluation, and unsupervised classification (Fig. 2.6).

2.2.3.1 Generation of displacement maps

The first step was the generation of displacement maps. For this purpose, each Sentinel-1 datasets (i.e. ascending and descending) collected in summer 2017 from mid-June to mid-October (about 21 images,

Figure 2.3) were processed using two different multitemporal interferometric techniques: Permanent Scatterers (PS) (Ferretti et al., 2001, 2000; Hooper et al., 2004) and Small BAseline Subset (SBAS) (Berardino et al., 2002). Both PS and SBAS provide quantitative displacement maps of the surface terrain along the Line Of Sight (LOS), but their theoretical principles are quite different. PS technique provides the displacement information exploiting particular scatterer points stable in phase and amplitude called permanent scatters. Therefore, this technique provides the punctual displacement information for each permanent scatter. SBAS technique provides the displacement information exploiting the spatial distribution of the phase information, therefore it provides the spatial displacement information for each SAR pixel of the investigated area. Both allow to mitigate effects such as atmospheric artefacts or topographic residuals exploiting the redundancy of a large number of SAR images (Berardino et al., 2002; Crosetto et al., 2016; Ferretti et al., 2001; Necsoiu et al., 2016; Osmanoğlu et al., 2016).

In this work, PS and SBAS techniques implemented in the SARscape software were used. At least 20 SAR images are recommended for the processing. The combination of Sentinel-1 A and Sentinel-1 B allow to acquire a sufficient number of SAR images during the snow-free periods, and apply multitemporal interferometric techniques.

The generation of displacement maps from PS technique is summarized in figure 2.7a. In the first step, the software selects the most suitable super master image. Then the network of the interferograms connection is generated, which connects each acquisition with the super master image; the images are coregistered with the super master, and each interferogram is computed. The third step is the selection of persistent scatter candidates, i.e. particular pixels that constantly have a similar, relatively large, amplitude during all acquisitions and a small phase dispersion. The displacement of each persistent scatter is computed, and then the atmospheric effects are estimated and subtracted from the original persistent scatter displacement. The next steps are the conversion of displacement and the geocoding, in order to project the satellite SAR images in geographic coordinates.

The generation of displacement maps from SBAS technique is summarized in figure 2.7b. The first step consists on the interferogram generation. In this step the network of the interferograms connection is generated, which connects each acquisition with others in order to achieve high redundancy, and the images are coregistered between them. Each possible pair of interferograms is computed. In this study case, since the displacement rates of rock glaciers are very wide, a maximum temporal baseline of 18 days is used, in order to avoid errors during phase unwrapping steps. The second step is phase unwrapping, to solve the phase ambiguity. The obtained interferograms are then corrected for atmospheric effects estimating and subtracting the atmospheric phase and re-computing the unwrapping. The next steps are the conversion from phase to displacement and the geocoding, in order to project the satellite SAR images in geographic coordinates.

2.2.3.2 Displacement maps evaluation

The second step was the visual evaluation of the displacement maps. Since the number of the SAR images used (21 images for each relative orbit) was close to the minimum number of images required by the software, an additional evaluation was conducted on the displacement maps. The evaluation was conducted checking that stable areas identified by geomorphological elements such as bedrock outcrops, evident striated rock and human infrastructures were not affected by movements. This evaluation step was conducted on the displacement maps obtained by the PS and SBAS techniques with both ascending and descending satellite geometric views. In this study case, the displacement maps obtained by the SBAS techniques proved to be less reliable and therefore were discarded by the classification procedure.

2.2.3.3 Unsupervised classification

The third step was the unsupervised classification of rock glaciers activity. The classification was conducted using the displacement maps obtained from the two satellite geometric views.

Depending on the rock glacier orientation, topographic effects occur such as layover and shadow (Hu et al., 2014; Klees and Massonnet, 1998). Therefore, rock glaciers with a layover-shadow area larger than 50% of the total area on both the geometric views were excluded. This threshold was chosen as a trade-off between robustness and number of excluded rock glaciers, i.e. non-classified.

Since the displacements are detected along the LOS, the most favourable satellite geometric view (i.e. ascending or descending) should be used depending on the rock glacier orientation (Hu et al., 2014; Klees and Massonnet, 1998). Since rock glaciers move mainly along the maximum slope direction (Bosson and Lambiel, 2016; Delaloye et al., 2010; Ikeda et al., 2008; Kääb and Weber, 2004), the angle between the LOS direction and the maximum slope direction was taken into account to identify the most favourable satellite geometric view. For each rock glacier the displacement map obtained from the geometric view with the smallest angle between the LOS direction and the maximum slope direction was selected. Thus, for each rock glacier only a displacement map was used for the classification procedure. Rock glaciers with angle greater than 60° between the LOS direction and the maximum slope direction on both the geometric views were excluded.

The classification of rock glaciers required the definition of a threshold in the displacement maps, which was chosen depending on their precision. We estimated this threshold using the displacement information along the LOS inside areas supposed as stable close to each rock glacier, identified by visual analysis of aerial orthophotos. These areas showed a certain displacement, due to errors during the SAR processing. In this study case, the displacement values from the PS technique had a gaussian distribution and a standard deviation (σ_{LOS}) of 45 mm along the LOS, for both the geometric views, on a total stable area around 4 Km^2. Then we assumed the double of LOS displacement standard deviation ($2\sigma_{LOS}$, i.e. 90 mm) as a valid displacement threshold to distinguish rock glacier displacements from residual errors.

Because the displacement is not homogeneous inside rock glaciers, the classification was performed taking into account also the spatial distribution of the displacement inside the rock glacier area. Only rock glaciers with LOS displacements higher than 90 mm on more than half of permanent scatters inside the rock glacier were classified as moving. For rock glaciers with LOS displacements lower than 90 mm on more than half of permanent scatters inside the rock glacier we are not able to understand if the displacement can be due to real slight displacements or errors during the SAR processing, because the measured LOS displacement is very similar or lower to the precision measured on the areas supposed as stable. This classification aggregates rock glacier without displacement or with minor displacement under the same class (i.e. no-moving) because of the precision of SAR measurements.

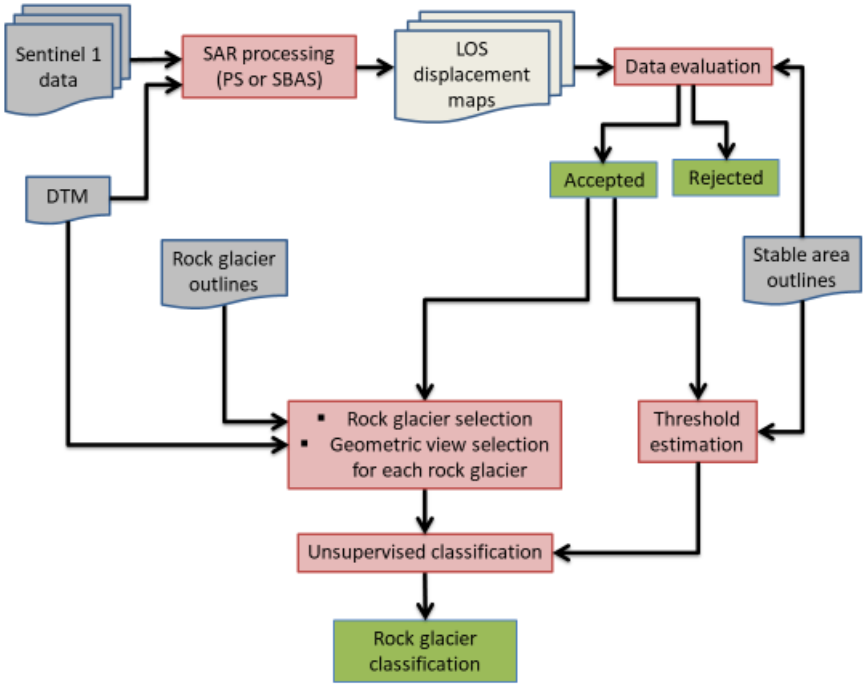

Figure 2.6: conceptual scheme of multitemporal interferometric approach. Sentinel-1 datasets are process with PS or SBAS techniques. The obtained displacement maps are visual evaluated. Displacement values are extracted from rock glaciers and areas assumed as stable, and the displacement threshold along the LOS is computed. Rock glaciers with LOS displacements higher than the threshold on more than half of pixels or permanent scatters inside the rock glacier were classified as moving. Rock glaciers with LOS displacements lower than the threshold on more than half of pixels or permanent scatters inside the rock glacier were classified as no-moving.

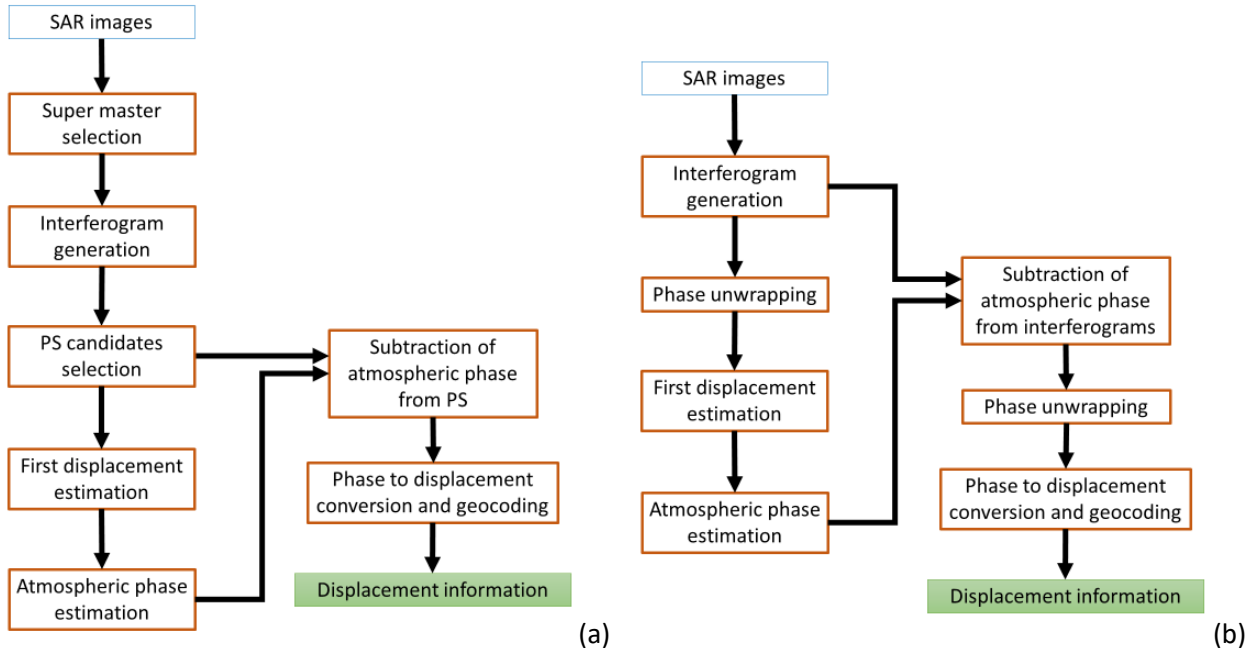

Figure 2.7: schema of PS (a) and SBAS (b) processing.

2.2.4 Evaluation of the proposed methods

Assuming that moving rock glaciers are probably affected by permafrost, we adopted two different criteria to evaluate the classification results obtained with our methods. The first criterion takes into account that the moving rock glaciers are expected to be located at higher altitudes with respect to the no-moving ones (Jones et al., 2018b; Onaca et al., 2017; Scotti et al., 2013). According to this assumption, the classified rock glaciers were plotted based on their altitudinal distribution. As a second evaluation criterion, we compared our classifications with the permafrost probability map provided by the GLOBpermafrost project (Bartsch et al., 2016), expecting a higher permafrost probability for rock glaciers classified as moving.

2.3 Experimental results

2.3.1 Rock glaciers classification based on interferometric coherence

2.3.1.1 Rock glaciers classification and comparison with the South Tyrol inventory

In this section, we present the rock glacier classification using the landforms mapped in the STI. In addition, we show the comparison between our activity classification and that provided by the STI.

Out of the 1665 rock glaciers included in the inventory, 527 landforms (32%) were classified by our method. The remaining rock glaciers were not classified because they are covered by vegetation (1057), are too small (73), are in layover and shadow conditions (1) or are in both the two last conditions (7). According to our method, 270 rock glaciers were classified as moving and 257 as no-moving (Fig. 2.8 and 2.9b). The 1057

vegetated rock glaciers excluded from our classification were added to the class of no-moving (Fig. 2.9c) (section 2.2.2). This assumption is supported by the classification of the STI, for which the 96% of the 1057 vegetated rock glaciers are labelled as inactive and relict (Fig. 2.8).

The comparative analysis between our classification and that included in the STI was carried out comparing our moving class with the active rock glaciers of the inventory, and our no-moving class with the inactive and relict. Out of the 270 rock glaciers classified as moving by our method, in the STI 152 (56%) were classified as active, i.e. in classification agreement, 72 (27%) as inactive or relict, i.e. disagreement (Fig. 2.8). The remaining (17%) were not labelled and only our classification could provide the activity information. We classified 257 rock glaciers as no-moving, and the agreement with STI (i.e. rock glacier labelled as inactive and relict) is 61%. The disagreement of 22% consists of rock glaciers which were labelled as active in the STI, while the remaining 17% of rock glacier in the STI were not labelled. Among the 81 rock glaciers not classified by our method, 4 (5%) were classified as active in the STI, 53 (65%) as inactive or relict, and 24 (30%) were not classified.

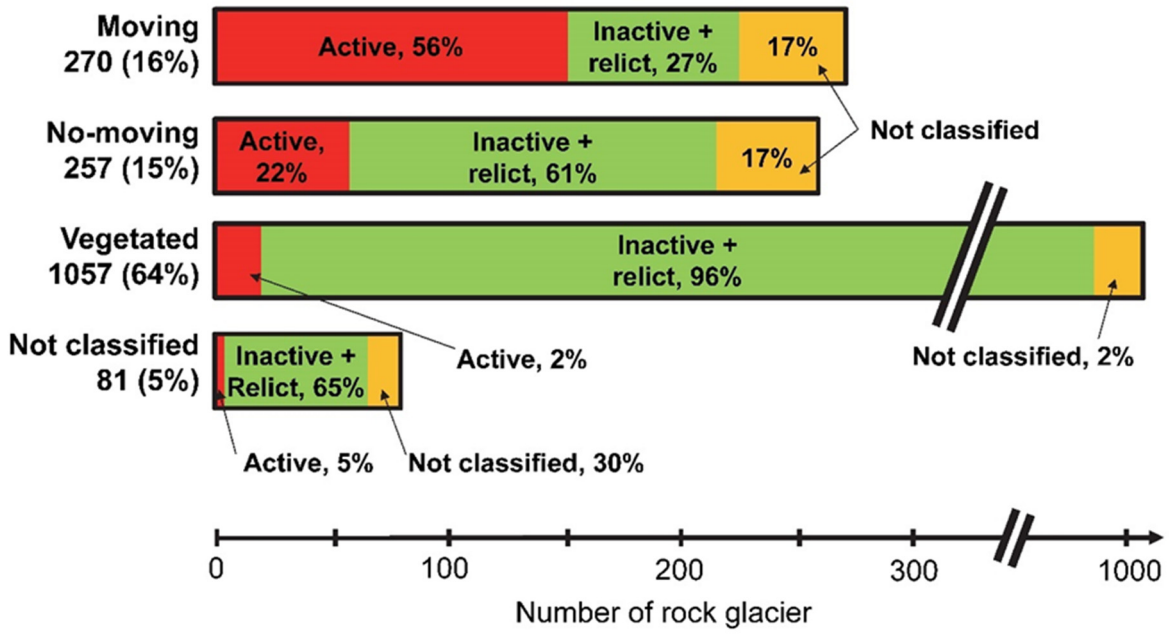

Figure 2.8: The length of the horizontal bars represents the number of rock glaciers classified as moving and no-moving by our method, the vegetated rock glaciers and the not-classified rock glaciers. Inside the horizontal bars the comparison between the number of labelled rock glaciers and the classification of the STI is shown by different colours, and the level of agreement is shown by the percentages.

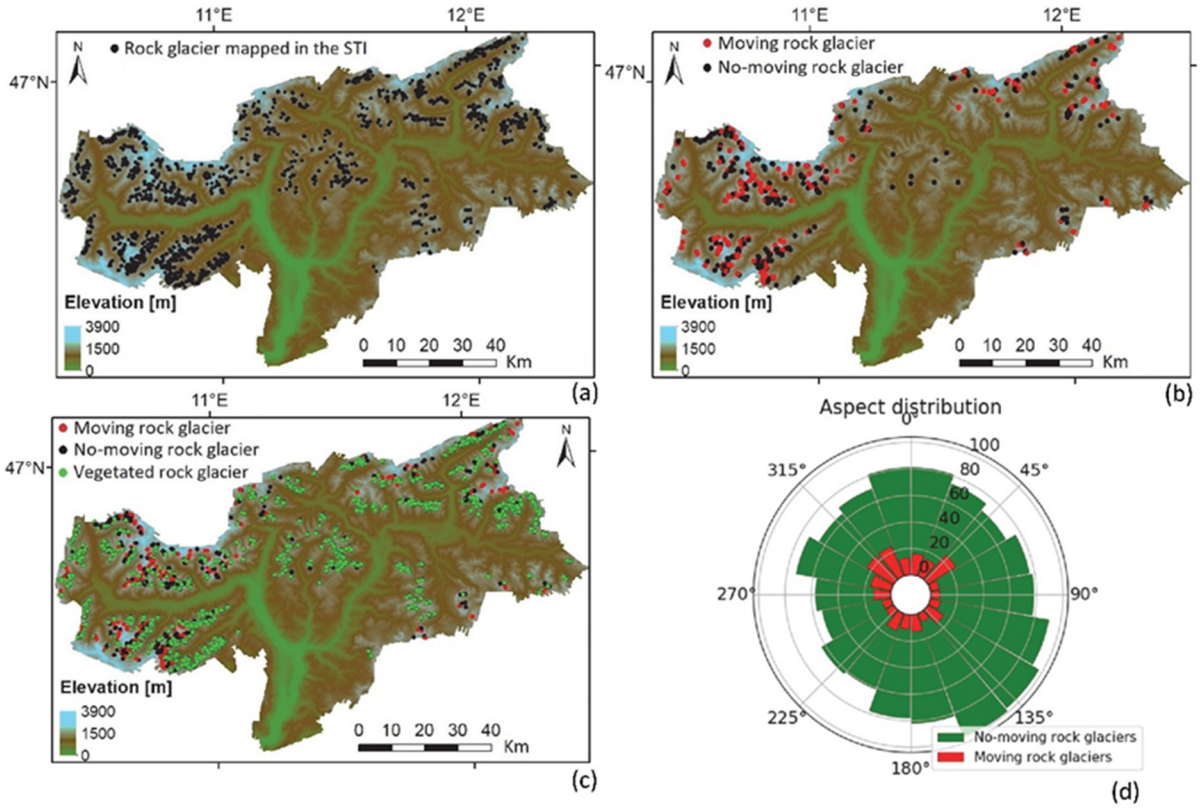

Figure 2.9: (a) rock glaciers mapped in the STI. (b) rock glaciers classified by our method and divided in moving (red dots) and no-moving (black dots). Vegetated rock glaciers are not displayed. (c) rock glaciers classified by our method and vegetated rock glaciers (green dots), which were added to the no-moving class. (d) rose diagram of aspect distribution of moving and no-moving forms, including the vegetated ones.

2.3.1.2 Validation with the Trentino dataset

Out of the 57 rock glaciers of Trentino, 21 were classified as moving and 28 as no-moving by the proposed method (Table 2.1). The remaining (eight rock glaciers) were not classified because they are too small (less than 80 SAR pixels) or have a layover or shadowing area higher than 50%. The validation results display an accuracy of 88% and a Kappa coefficient of 0.76 (Table 2.1). The number of rock glaciers misclassified as no-moving by our method (5) is overestimated with respect to the number of those misclassified as moving (1).

Table 2.1: Confusion matrix between the coherence-based classification and the Trentino dataset.

	Accuracy 88% Kappa 0.76	Trentino dataset	
		Moving	No-moving
Coherence classification	Moving 21 (39%)	20	1
	No-moving 28 (47%)	5	23
	Not classified 8 (14%)	4	4

2.3.1.3 Performance test with a restricted dataset of images

Using only the images of August 2017, 161 rock glaciers were classified as moving and 366 as no-moving in South Tyrol (Fig. 2.10a). The validation results obtained using the Trentino rock glaciers provided an accuracy value of 71% and a Kappa coefficient of 0.43, both being lower than the values obtained using the complete dataset (Table 2.1). The confusion matrix shows that our method correctly classified 14 rock glaciers as moving and 21 as no-moving, whereas the misclassification consists of 11 rock glaciers labelled as no-moving and 3 rock glaciers labelled as moving (Table 2.2).

The second performance test was conducted using only the images acquired in September 2017. In South Tyrol, 301 rock glaciers were classified as moving and 226 as no-moving (Fig. 2.10b). The validation performed using the set of Trentino rock glaciers showed an accuracy value of 86% and a Kappa coefficient of 0.72, which are only slightly lower than those obtained with the complete dataset (Table 1). As shown by the confusion matrix (Table 2.2), our method correctly classified 42 rock glaciers (19 as moving and 23 as no-moving), whereas the misclassification consists of seven rock glaciers. Therefore, using a restricted dataset of images, the no-moving rock glaciers are overestimated, and the accuracies and kappa coefficients are overall lower than those obtained with the complete dataset.

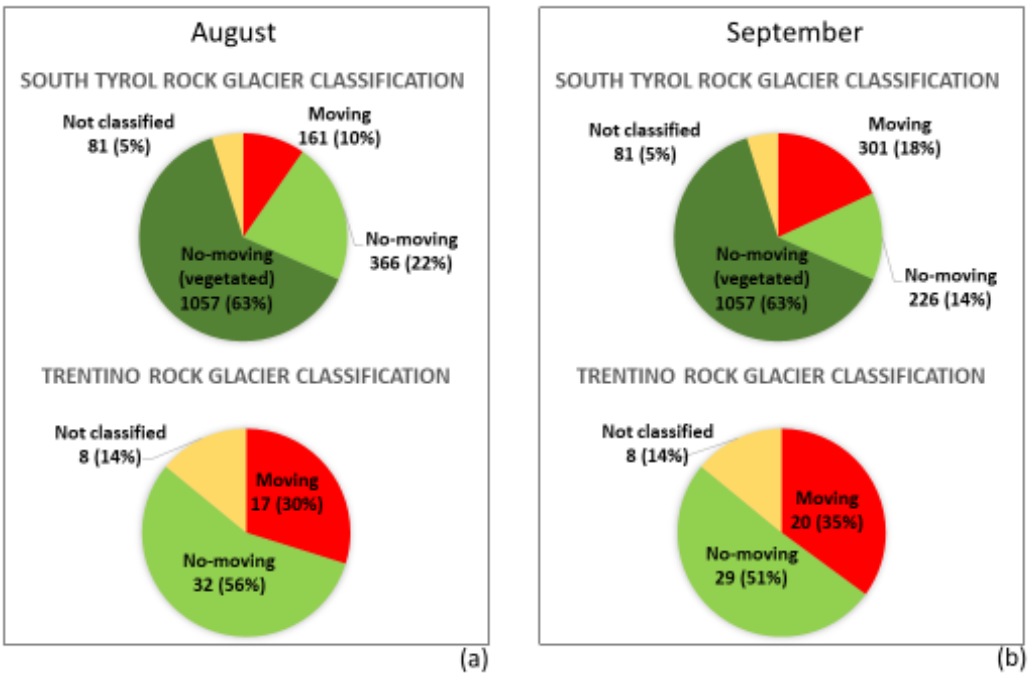

Figure 2.10: Results of the rock glacier classification in Trentino and South Tyrol using the restricted dataset of images acquired in August (a) and September (b) 2017.

Table 2.2: Confusion matrix between the coherence-based classification and the Trentino dataset using the images of August (left) and September (right) 2017.

		Trentino dataset			
		August		**September**	
		Accuracy 71%, Kappa 0.43		Accuracy 86%, Kappa 0.72	
Coherence classification		Moving	No-moving	Moving	No-moving
	Moving	14	3	19	1
	No-moving	11	21	6	23

As a useful example to clarify the better results of the tests conducted with the restricted datasets of images, the SABD and the coherence trends for two rock glaciers of Trentino recognized as moving (section 2.2.1) were plotted over time for three temporal baselines (6, 12, and 18 days) (Fig. 2.11). Results showed three evidences. First, an overall decrease in the coherence values by increasing the temporal baseline is observable. Second, as expected, an opposite trend between the SABD and the coherence is visible. In particular, a decrease in the coherence values from August to September is visible, especially for the shorter

temporal baselines (i.e. 6 and 12 days). Third, despite a SABD trend is observable, the SABD difference over time between the images selected by our method (using both the complete and reduced datasets) is very low, compared to the total variation.

The coherence trends shown in figure 2.11a are referred to a rock glacier classified as moving using both the complete dataset (two months) and the reduced dataset (August or September 2017). A decrease in the coherence values from August to September is visible along with a slight increase of SABD. The example shown in figure 2.11b is referred to a rock glacier classified as no-moving in the August images, and as moving in the September images. For each temporal baseline, the coherence values of the images selected for August are higher than those of September and this may explain the different classification. This rock glacier was classified as moving using the complete dataset, despite the images selected for the complete dataset (red circles) are the same to those selected for the reduced dataset of August (red diamonds). This different classification is due to the larger temporal baselines (i.e. 30, 36, 42, 48 and 54 days) used with the complete dataset.

Finally, the performance of our method was evaluated reducing the maximum temporal baseline up to 6 days. We evaluated the minimum temporal baseline that generate a decrease in the performance of our method. The performance trend is visualized in figure 2.12. With temporal baseline lower than 36 days the performance of our method decreases.

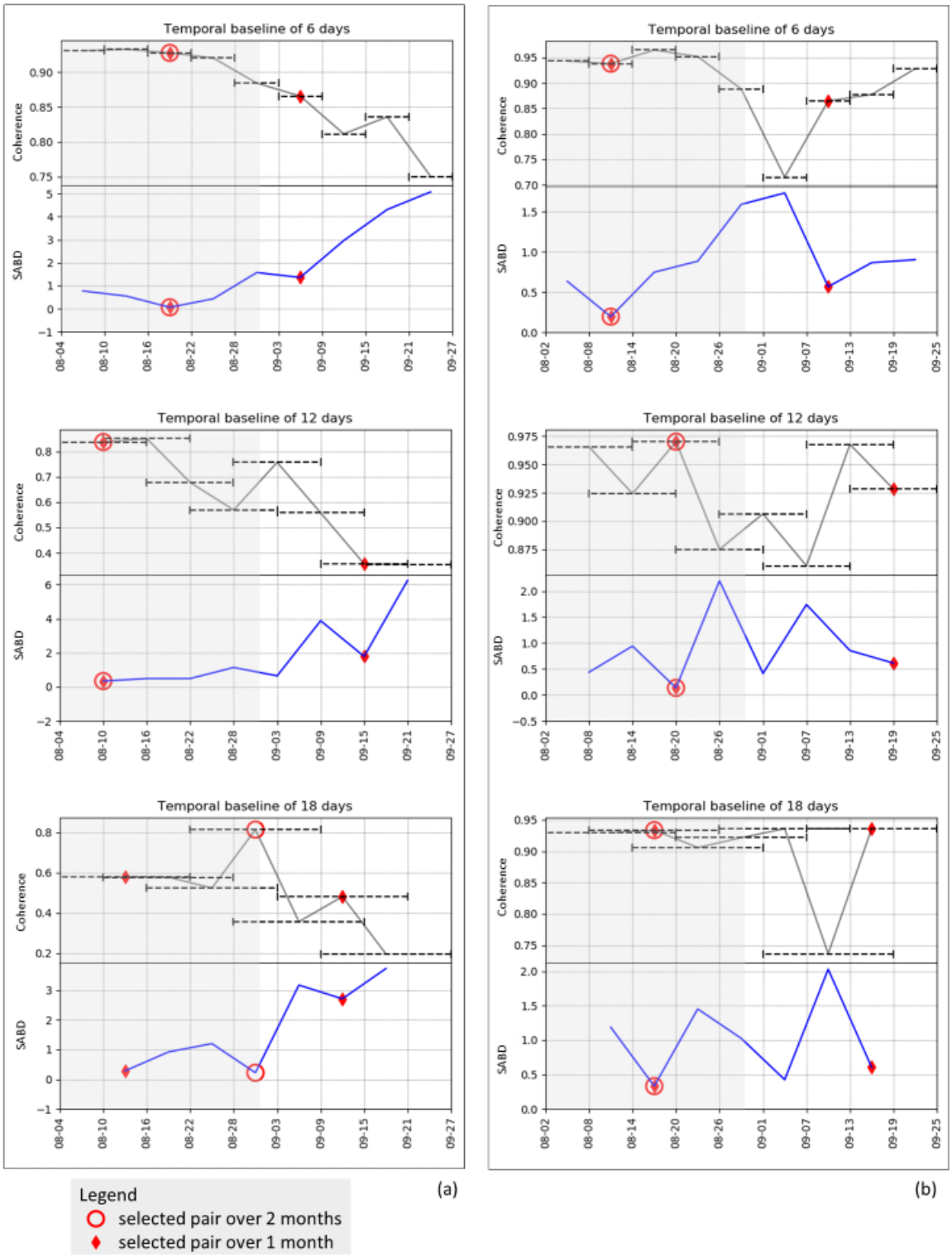

Figure 2.11: Coherence trends (black lines) and SABD trends (blues lines) for three temporal baselines (6, 12, and 18 days) of two selected rock glaciers in Trentino. Red circles indicate the pair of images selected with the complete dataset (two months), while the red diamonds indicate the pair of images selected with the reduced dataset (one month). Horizontal dashed lines indicate the time interval for each pair of images (master and slave). In most cases, the image selected for the complete dataset is the same to that selected for the reduced dataset. Left figure (a) is referred to a rock glacier classified as moving using both the complete dataset (two months) and the reduced dataset (August or September 2017). Right figure (b) is referred to a rock glacier classified as no-moving in the August images, and as moving in the September images. For the same temporal baseline, the ranges of coherence values between the figure (a) and (b) are different.

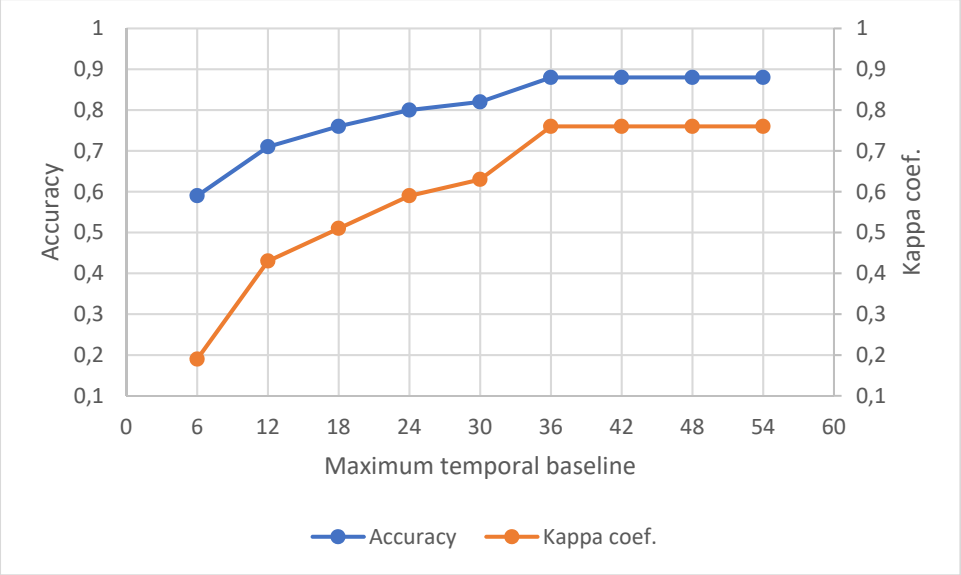

Figure 2.12: trend of accuracy and kappa coefficient for each maximum temporal baseline used.

2.3.2 Rock glaciers classification based on multitemporal interferometric techniques

2.3.2.1 Multitemporal interferometric results

Portions of displacement maps obtained by PS and SBAS processing are showed in figure 2.13. Large gaps into the valleys at low altitude are due to vegetation, which generates decorrelation effects. Observing the PS displacement maps we can observe that most areas have displacement close to zero, and small displacement areas are localized inside the rock glaciers boundaries, along the mountain slope, and on the ridges of the mountains. The latter are very unlikely, so it is possible that they are due to errors such as atmospheric artefacts or residual heights not removed during the SAR processing. Displacements detected inside the rock glaciers provide information on their kinematics, and outside them they allow to identify other creeping landforms, such as solifluction areas, debris creep, landslides. With the SBAS displacement maps, wide areas with displacements unrelated to visible geomorphological landforms are observed. Furthermore, these wide areas are not confirmed in the PS maps, and are not plausible because high displacement rates were detected also on stable areas. For this reason, SBAS maps were discarded and the rock glacier classification was carried out using only PS displacement maps.

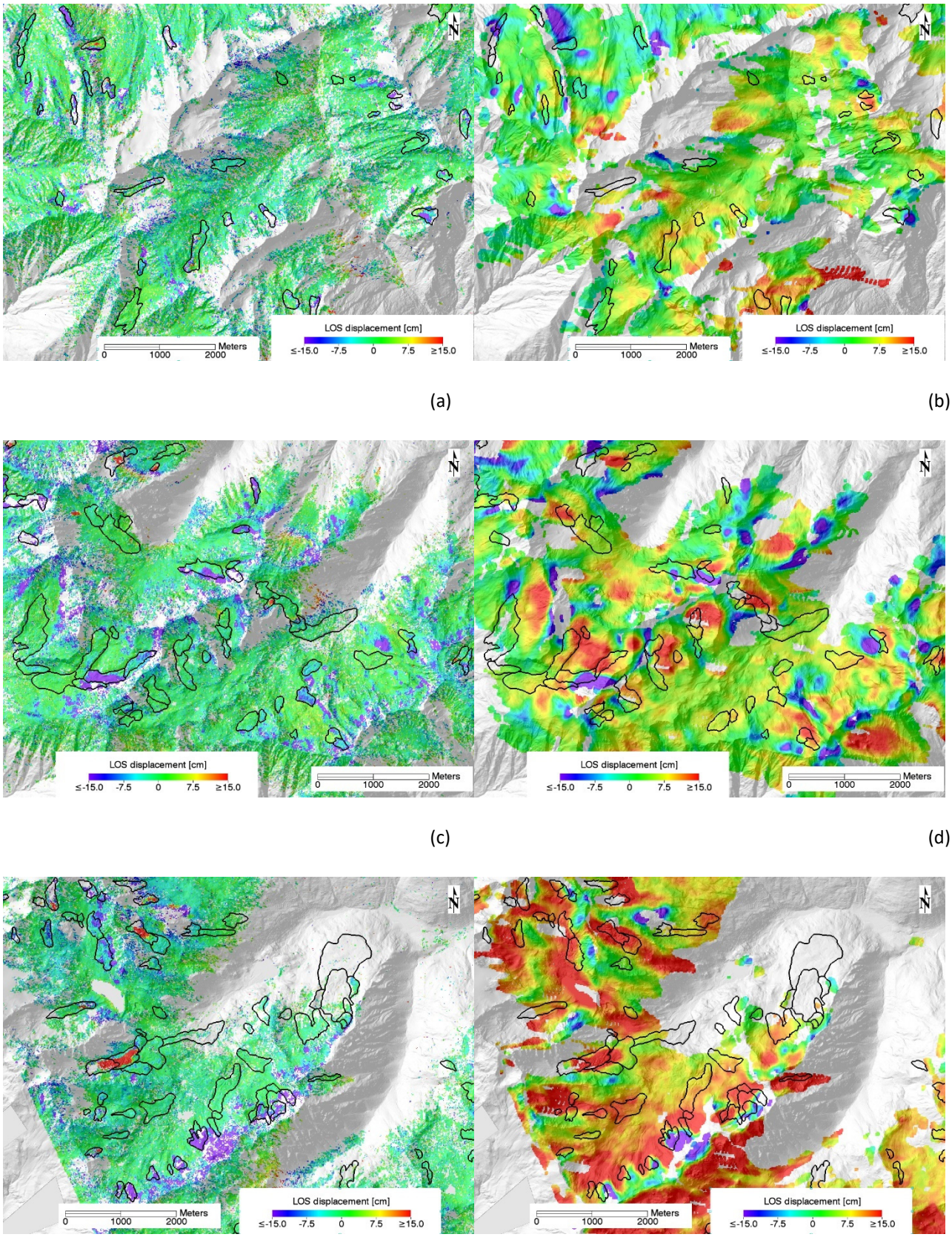

Figure 2.13: three different portions of displacement maps along the LOS direction, obtained by PS (left side, (a), (c) and (e)) and SBAS (right side, (b), (d) and (f)) with Sentinel-1 relative orbit 168. Black lines are the rock glaciers boundaries. Many large displacement areas in SBAS maps are not observable in PS maps, and most areas have displacement close to zero in PS displacement maps.

The orientation of the rock glacier compared to the LOS is a determining factor and the two different Sentinel-1 geometries produce different results (Fig. 2.14). Looking the PS displacement map from the relative orbit dataset 117 (ascending geometry) the West facing rock glaciers have not persistent scatters because of their orientation compared to the LOS, while East facing rock glaciers have persistent scatters. The opposite is true for the PS displacement map obtained with the relative orbit dataset 168 (descending geometry).

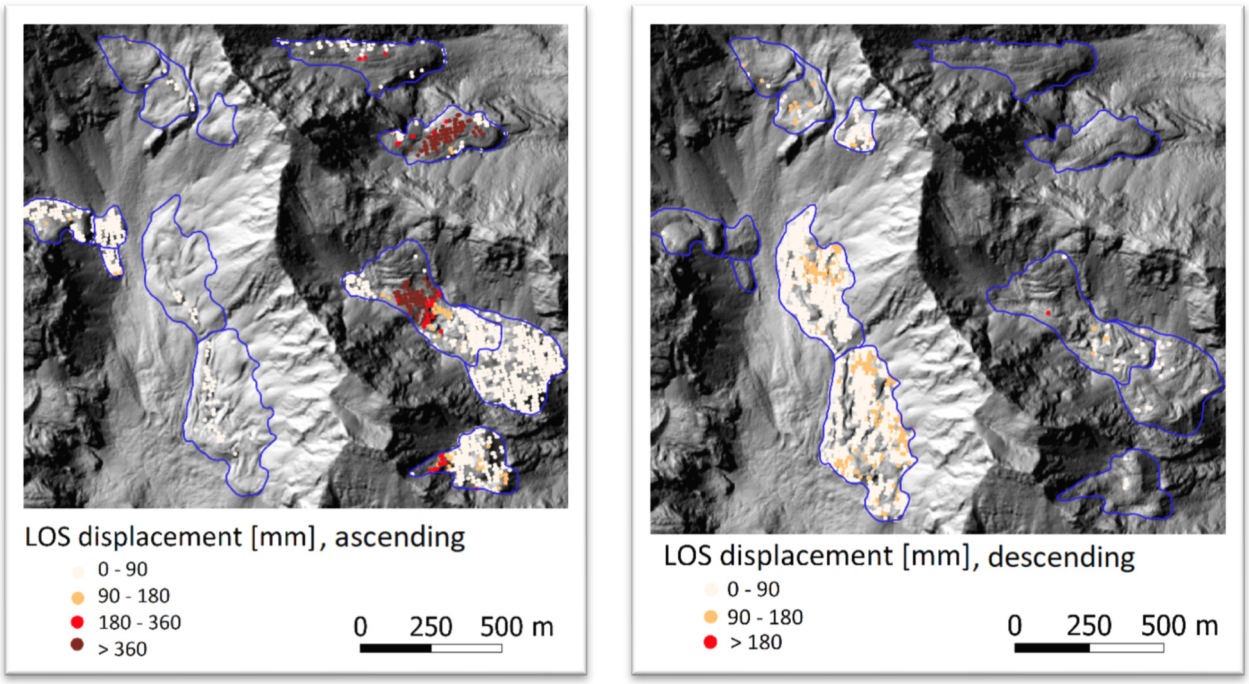

(a) (b)

Figure 2.14: zoom on several rock glaciers with different orientation. (a) PS displacement map from the relative orbit dataset 117 (ascending geometry). Rock glaciers West facing have not persistent scatters because of their orientation compared to the LOS, then are not classified by the ascending dataset. Rock glaciers East facing have persistent scatters. In some rock glaciers different displacement sectors are identifiable thanks to aggregation of persistent scatters with high displacement values. (b) PS displacement map from the relative orbit dataset 168 (descending geometry). With this geometry the rock glaciers East facing have not persistent scatters, while the rock glaciers West facing have persistent scatters.

2.3.2.2 Rock glaciers classification and comparison with the South Tyrol inventory

The classification was performed with the PS results obtained from the relative orbit dataset 117 and 168. Out of the 1665 rock glaciers included in the inventory, more than 1300 landforms were classified by our method. The remaining rock glaciers were not classified because they are in layover and shadow conditions (356). According to our method, 144 rock glaciers were classified as moving and 1165 as no-moving (Fig. 2.15).

The comparative analysis between our classification and the one included in the STI was carried out comparing our moving class with the active rock glaciers of the inventory, and our no-moving class with the inactive and relict. Out of the 144 rock glaciers classified as moving by our method, in the STI 58 (40%) were classified as active, i.e. in classification agreement, 58 (40%) as inactive or relict, i.e. disagreement (Fig. 2.15). The remaining (20%) were not labelled and only our classification could provide the activity information. We classified 1165 rock glaciers as no-moving, and the agreement with STI (i.e. rock glacier labelled as inactive and relict) is 85%. The disagreement of 9% consists of rock glaciers that were labelled as active in the STI, while the remaining 6% of rock glacier in the STI were not labelled. Among the 356 rock glaciers not classified by our method, 69 (19%) were classified as active in the STI, 246 (69%) as inactive or relict, and 41 (12%) were not classified.

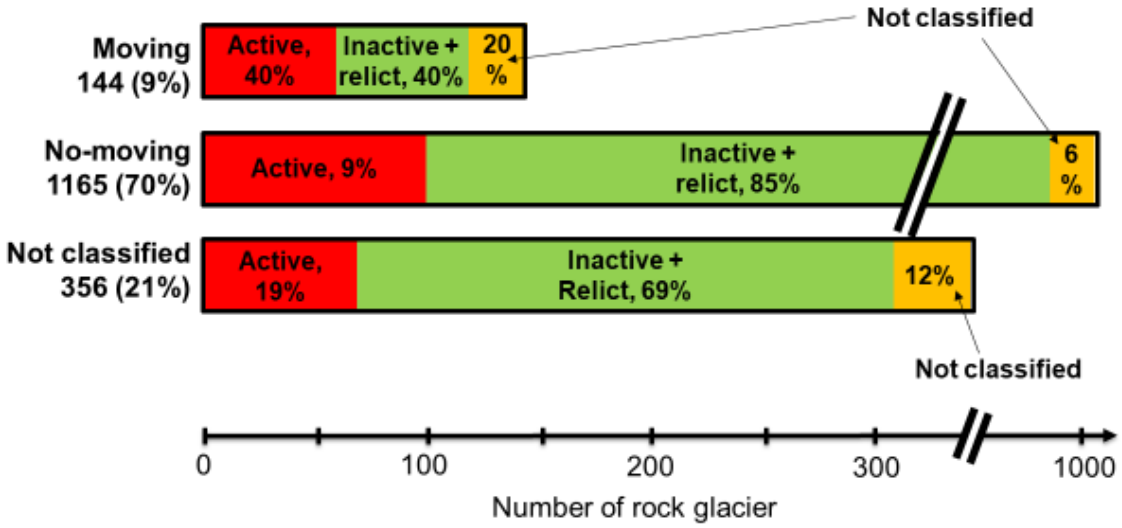

Figure 2.15: The length of the horizontal bars represents the number of rock glaciers classified as moving and no-moving by our method, and the not-classified rock glaciers. Inside the horizontal bars the comparison between the number of labelled rock glaciers and the classification of the STI is shown by different colours, and the level of agreement is shown by the percentages.

2.3.3 Evaluation of the rock glacier classifications with altitude and permafrost probability

According to the first evaluation criterion (section 2.2.4), the rock glaciers classified by our two method were plotted based on their altitudinal distribution (Fig. 2.16), including the classification of the STI. Landforms classified as no-moving are located at an altitude between 1800 and 3100 m, with a mean of 2409m for the coherence-based approach, and 2419m for the PS-based approach, while rock glaciers classified as inactive and relict in the STI are located at a mean altitude of 2376m. Moving landforms are located between 2300 and 3100 m of altitude, with a mean of 2700m for the coherence-based approach, and 2646m for the PS-based approach, while rock glaciers classified as active in the STI are located at a mean altitude of 2759m. Rock glaciers classified as moving are therefore located 300 m and 227 m above the no-moving ones for the

coherence- and PS -based approaches, respectively, and these differences support the robustness of our analyses.

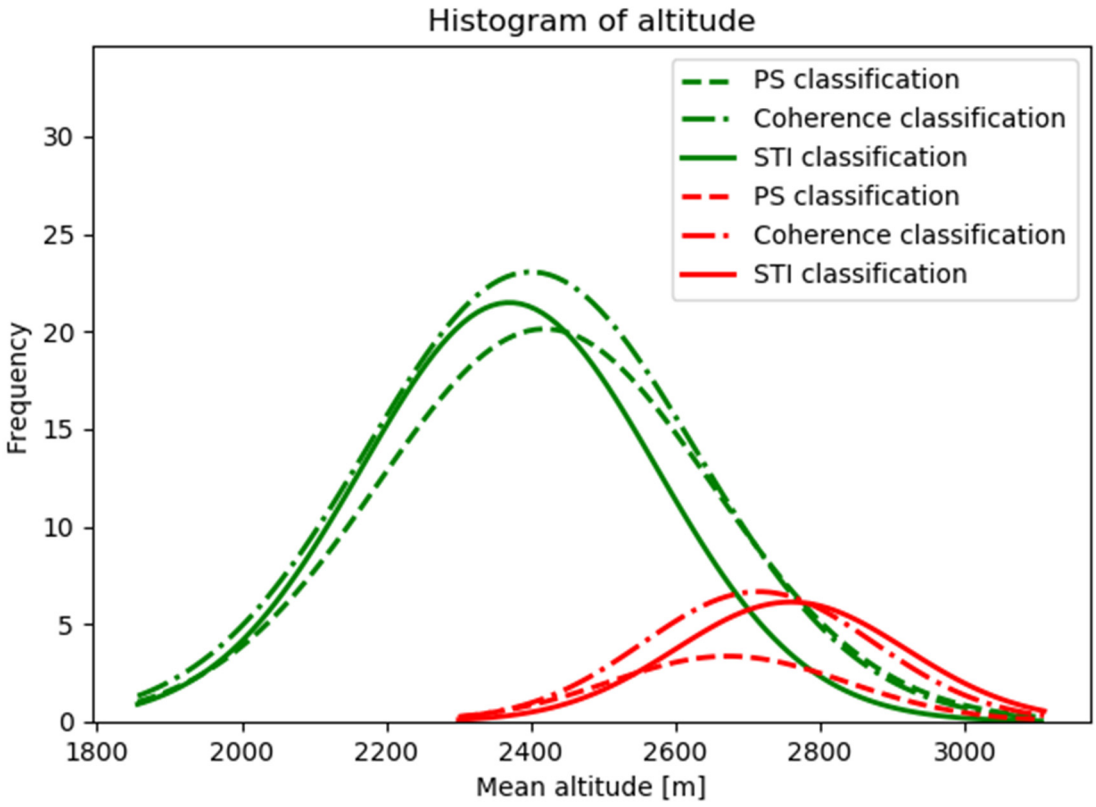

Figure 2.16: Altitudinal distribution of moving (red line) and no-moving rock glaciers (green line) classified from the interferometric coherence and PS approach. The altitudinal distribution of active (red line) and inactive/relict rock glaciers (green line) of the STI is also shown.

For the second evaluation criterion, we plotted the permafrost probability distribution of moving rock glaciers (Fig. 2.17). According to the probability map, the rock glaciers classified as moving are located in areas with high permafrost probability values, with an average of 0.81 (coherence-based) and 0.73 (PS-based). A small number of moving rock glaciers show low permafrost probability values. The low permafrost probability of some rock glaciers may be due to a combination of classification errors and the low resolution of the permafrost probability map (1 Km). Active rock glaciers from the STI are located in areas with mean permafrost probability of 0.86.

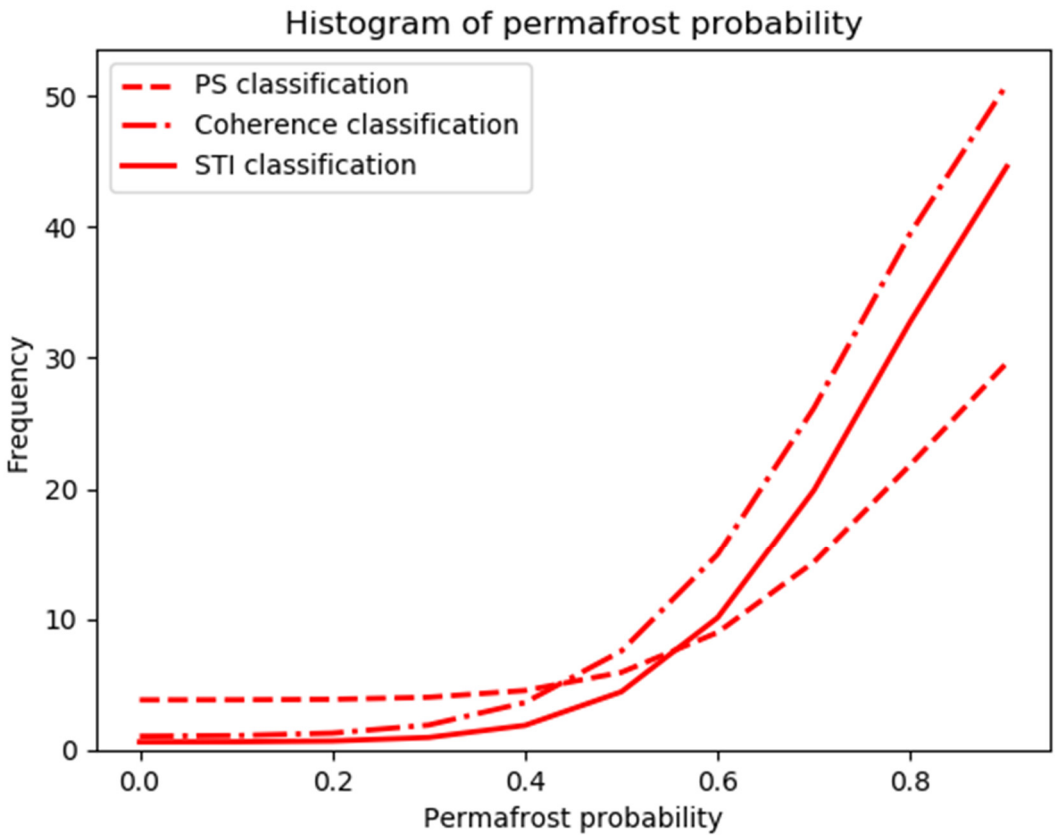

Figure 2.17: Permafrost probability distribution of moving rock glaciers classified from the interferometric coherence and PS approach according to the GLOBpermafrost map. The Permafrost probability distribution of active glaciers of the STI is also shown.

2.4 Discussion

In this work, two SAR-based, unsupervised methods to classify the activity of rock glaciers were developed. The potential of the interferometric SAR coherence of Sentinel-1 images, as well as the multitemporal interferometric techniques, were exploited to distinguish moving and no-moving landforms over large mountainous area. We developed and tested our methods in the Eastern Italian Alps, where the geographical location and the outline of rock glaciers was extracted from existing inventories (Mair V., Zischg A., Krainer K., Stötter J., Zilger J., Belitz K., 2008; Seppi et al., 2012).

As suggested by Villarroel et al. (2018), the information on the activity of rock glaciers can be derived from the analysis of multitemporal optical data and the interpretation of geomorphological evidences, such as, among others, the inclination of the frontal slope, presence or absence of vegetation, degree of development of furrows and ridges over the rock glacier surface. However, one of the main weakness of such criteria is that they are based on subjective interpretations and can therefore lead to erroneous classifications. At a large scale, displacement information can be obtained using differential interferometry (Barboux et al., 2015,

2014; Jones et al., 2018a; Liu et al., 2013; Rouyet et al., 2019; Strozzi et al., 2004; Wang et al., 2017). SAR data processing through the interferometric techniques is often difficult in high mountain regions, especially for the unwrapping processes (Barboux et al., 2014; Villarroel et al., 2018). Our coherence-based method provides an objective kinematic classification of landforms, thus avoiding the subjectivity of geomorphological analyses, and independent from complicated unwrapping processes. Our multitemporal interferometric approach is able to compensate for the drawbacks of existing methods based on simple differential interferometry, and successfully provides a kinematic classification of the landforms.

SAR-based approaches such as those used in our work are affected by layover and shadow effects, because of the SAR imaging geometry and the complex topography of high mountain regions (Bamler and Hartl, 1998; Rott et al., 1999). Consequently, extended areas with these effects can potentially decrease the number of landforms that can be investigated. In order to reduce these effects, Rott et al. (1999) and Strozzi et al (2004) suggest the use of the most appropriate image geometries (i.e. ascending and descending) depending on the orientation of the objects to be investigated. In this work, two datasets with different relative orbits were used, thus increasing the number of classified rock glaciers by using the most appropriate geometry. Indeed, our findings show that, exploiting the relative orbit 117 and 168 (Fig. 2.1a), only 17% (coherence-based approach) and 21% (PS-based approach) of all the investigated rock glaciers were excluded because of extensive layover and shadow effects. Therefore, at a large scale, a key element to reduce the number of unclassified landforms is the use of different relative orbit datasets.

2.4.1 Interferometric coherence approach

In our work, an original application of the interferometric coherence, estimated with different temporal baselines, was used to investigate the activity of rock glaciers. To define the activity status of rock glaciers, the strength of our approach relies in the use of the interferometric coherence, which can be easily estimated. Other widely used interferometric approaches, such as the DIn-SAR, allow obtaining displacement maps, from which indirectly estimate the activity of rock glaciers by visual interpretation (Liu et al., 2013; Rouyet et al., 2019; Strozzi et al., 2004). However, although these approaches are the most established, they could be somewhat subjective and may lead to misinterpretations. Therefore, our approach may help overcome these limitations.

An innovative point of our method is the use of the rock glacier outlines as boundaries to estimate the coherence, which is usually estimated using regular kernel windows (Bamler and Hartl, 1998; Touzi et al., 1999). In order to avoid the averaging estimation of coherence in the kernel window and the possible biases towards higher coherence values, we estimated the coherence using as window the outline of the rock glaciers (Equation 2.2). The single estimated SAR coherence value is therefore representative of the entire area of each investigated rock glacier. However, this outline-dependent approach requires an accurate definition of the rock glacier perimeters, and this may represent a limitation if this is poorly accomplished.

Indeed, the use of inaccurate rock glacier outlines (e.g. perimeters excluding parts of the landform or including external parts) may conduct to non-representative coherence measure, thus making an incorrect classification. Currently, the geographical outlines can be drawn from the analysis of orthophotos and DTMs (e.g. (Roer and Nyenhuis, 2007; Scotti et al., 2013; Seppi et al., 2012)), however, the criteria to map the rock glaciers are still not standardized and large margins of uncertainty and subjectivity still remain, especially for composite landforms (Brardinoni et al., 2018). In the inventory used for our work (i.e. the STI) (Mair V., Zischg A., Krainer K., Stötter J., Zilger J., Belitz K., 2008), the landforms were also mapped from the interpretation of aerial orthophotos and DTMs. The experience and training of the operators in compiling this good quality inventory have contributed to reduce the potential misclassifications due to the coarse definition of the rock glacier outlines.

The validation procedure with the Trentino dataset highlighted a slight overestimation of rock glaciers classified as no-moving by our method. This can be explained by three reasons.

The first is the SAR geometric view, because the LOS orientation compared to the rock glacier orientation is frequently not favourable to detect deformations (Rott et al., 1999; Strozzi et al., 2004). For example, for those rock glaciers with the main axis aligned around the North-South direction, the displacement may not be detectable. Therefore, in correspondence to the North-South direction, no-moving rock glaciers could be overestimated. This limiting factor can be reduced by using the most appropriate SAR geometry depending on the rock glacier orientation (Rott et al., 1999; Strozzi et al., 2004). In this work we used two different geometries (i.e. relative orbits 117 and 168) and the results show that, in correspondence to the North-South direction, no-moving rock glaciers are not overestimated, with the number of moving rock glaciers not strongly reduced (89 moving rock glaciers are distributed around the North-South direction +/- 30°, Figure 2.7d). Therefore, in our work, the SAR geometric view cannot explain the observed overestimation of no-moving rock glaciers.

The second reason is the particular spatial displacement pattern that characterizes some rock glaciers. As suggested by Touzi et al. (1999), a homogeneous displacement inside the boundary used to estimate the coherence does not lead to a decrease in the coherence value. Therefore, rock glaciers exhibiting a homogeneous displacement pattern are classified as no-moving, because the coherence values estimated in their perimeter do not decrease over time. This kind of displacement pattern was recognized for small- to medium-sized rock glaciers composed by a single debris lobe, which moves with similar velocities over time. They were called “monomorphic” rock glaciers (Frauenfelder and Kääb, 2000). Some of them were identified from multitemporal orthophotos and DTMs in the Trentino dataset, and this may partly explain the resulting overestimation of no-moving rock glaciers in the validation procedure.

The third reason is the existence of rock glaciers with very small displacement rates, that could not be detected using short temporal baselines (Bamler and Hartl, 1998). To detect small displacements, Villarroel et al. (2018) suggest using large temporal baselines (e.g. up to 60 days). In our work, different baselines were used, and the overestimation of no-moving rock glaciers was reduced using the larger ones (e.g. 30, 36, 42, 48 and 54 days), able to detect also very small displacements. Indeed, our findings showed that, among the three classification tests conducted using (i) the complete dataset of Sentinel-1 images, (ii) the images acquired only in August and (iii) those acquired only in September, the best classification performance was obtained using the complete dataset, and the number of no-moving rock glaciers was slightly overestimated using the two restricted datasets. For example, a rock glacier from the Trentino dataset surveyed with a laser total station and having an average velocity of 0.09 m y^{-1} (Seppi et al., 2019) was classified as moving using the complete dataset, while using the images acquired only in August (maximum temporal baseline of 24 days) the displacement was not detected.

On the contrary, an overestimation of moving rock glaciers could be generated by the presence of vegetation, because decorrelation effects due to vegetation reduce the coherence values (Balzter, 2001; Zebker and Villasenor, 1992). To mitigate this problem, heavily vegetated rock glaciers can be excluded from the processing by using, if available, a land cover map, as was done in our work. Alternatively, vegetated rock glaciers can be excluded based on the Normalized Difference Vegetation Index (NDVI). In this work, an overestimation of moving rock glaciers was not observed. A negligible number of rock glaciers were misclassified as no-moving by our method (Table 2.1 and 2.2), probably because of decorrelation effects unrelated with the displacement (Corbane et al., 2018; Klees and Massonnet, 1998; Lee et al., 2013).

An alternative hypothesis that can partly explain the observed overestimation of no-moving rock glaciers can be due to a possible change of the rock glaciers displacement rate between the period of the visual analysis conducted in Trentino (2006 – 2014) and the period investigated by SAR images (summer 2017). Direct measurements of surface displacements conducted on two rock glaciers, however, lead us to exclude this hypothesis (Seppi et al., 2019).

The two rock glaciers used as examples in the section 2.3.1.3 showed a decrease in the coherence values from August to September (Fig. 2.11). This loss of coherence may be explained by a different activity behaviour of the two landforms, with a possible acceleration in September. The number of studies documenting variations in rock glacier velocity over short periods (i.e. seasonal or sub-seasonal) is very limited. However, recent continuous measurements conducted on some rock glaciers in the Alps (Kenner et al., 2017; Wirz et al., 2016) suggest sub-seasonal velocity variations, with an increase during the summer and maximum velocities at the beginning of autumn. Therefore, our findings suggest that, at least for the two investigated landforms, the decreasing trend of the coherence is probably related to an increase of sub-

seasonal displacement rates, and suggest that the coherence can be sensitive to short-term displacement variations. However further investigations are required to confirm this result.

Among the two classification tests conducted by using the restricted dataset of Sentinel-1 images (i.e. the images acquired only in August and only in September), the validation procedure with the Trentino dataset obtained the best performance using the images of September, with an accuracy of 86% and a kappa coefficient of 0.72. In August, a higher overestimation of no-moving rock glaciers is observable. This result may be explained by the decrease in the coherence values from August to September observable from the two investigated rock glaciers (Fig. 2.11). As rock glacier velocities increase during the summer, displacement rates are lower in August and higher in September. Therefore, rock glaciers moving at low velocities are easier identified in September because their displacement rates are higher than in August. This may have caused an overestimation of the no-moving rock glaciers in the analyses based on the August dataset.

2.4.2 Multitemporal interferometric approach

Multitemporal interferometry was applied to classify the rock glaciers activity. In literature the activity of rock glaciers is often estimated by visual interpretation of displacement maps obtained from SAR processing (Liu et al., 2013; Rouyet et al., 2019; Strozzi et al., 2004). This work proposes an alternative unsupervised approach to obtain the rock glacier activity.

In high mountain areas, the application of specific multitemporal SAR techniques (Berardino et al., 2002; Ferretti et al., 2001) is often restricted, if not hampered, by the scarce number of suitable SAR images available in the snow-free period, which can be particularly short. The 6 days revisiting time of Sentinel-1 allowed acquiring a sufficient quantity of images during the snow-free period, and applying the multitemporal techniques. In this work, SBAS displacement maps were discarded because affected by errors such as displacements on stable areas and wide moving areas not related with geomorphological evidences. These errors are probably due to atmospheric phase components related with the topography and not removed during the processing. Similar effects were observed in other works (Yu et al., 2018, 2017). These authors suggest a manual correction of each interferograms to remove these atmospheric phase components. Topographic residuals errors are unlikely because a high resolution DTM was used. Other authors (Barboux et al., 2015; Liu et al., 2013; Necsoiu et al., 2016) applied successfully SBAS techniques in mountain areas, using other satellite data with different sensor wavelength and spatial resolutions. PS displacement maps did not show the same problems and have proved to be more reliable. The greater reliability of the PS processing is probably due to the low spatial resolution of Sentinel-1 data, because PS allows to study the displacement of scatterer points with dimensions smaller than the SAR cell. In addition, the SAR phase processing is more difficult on areas with high altitude variability and widespread vegetation; in this context PS is more powerful because it exploits both backscattering and phase information to study

the displacement, while SBAS only exploits the phase information. As a result, PS allows a better removal of atmospheric artefacts in mountain regions.

2.4.3 Comparison between the proposed approaches

Exploiting the relative orbit 117 and 168 (Fig. 2.3), 79% of the investigated rock glaciers were classified with the multitemporal interferometric approach. With the coherence-based approach a higher percentage (95%) of the investigated rock glaciers were classified, probably because vegetated rock glaciers excluded from the classification were added to the class of no-moving (see section 2.2.2). With the multitemporal interferometric approach vegetated rock glaciers were included in the classification procedure, but vegetation may induce decorrelation effects (Barboux et al., 2014; Touzi et al., 1999) and therefore reduce the surface displacement information. As result a lower number of rock glaciers were classified by the multitemporal interferometric approach.

Out of the 1665 rock glaciers included in the STI, 9% of rock glaciers were classified as moving and 70% as no-moving by the multitemporal interferometric approach, whereas the coherence method classified 16% of rock glaciers as moving and 79% as no-moving. The lower percentage of rock glacier classified as moving with the multitemporal interferometric approach depends on the low accuracy of the SAR products. Large displacements occur in stable areas, and the threshold value of 90 mm to detect displacement over rock glaciers is relatively high. Consequently, rock glaciers with displacements lower than the threshold were classified as no-moving, but this class probably includes rock glaciers with slight movements, not distinguishable from the no-moving ones because of the low accuracy of displacement maps. This explains the lower percentage of rock glaciers classified as moving with the multitemporal interferometric approach.

Rock glaciers classified as moving by the coherence approach are located at higher altitude compared to those classified as moving by the multitemporal interferometric approach (Fig. 2.16). The STI classification provides the highest altitude of active rock glaciers. Rock glaciers classified as no-moving by the coherence approach are located at lower altitude compared to those classified as no-moving by the multitemporal interferometric approach. The STI classification provides the lowest altitude of inactive and relict rock glaciers. The moving rock glaciers classified by the coherence approach are located in areas with higher permafrost probability values, compared to the moving rock glaciers classified by multitemporal interferometric approach (Fig. 2.17). The highest permafrost probability is obtained for the active rock glacier of the STI. These results support the robustness of our analyses, although some moving rock glaciers have low permafrost probability or are located at low altitudes.

2.5 Conclusions

In this study, two original, unsupervised methods to classify the activity of rock glaciers by using SAR remote sensing approaches were developed. Backscattering and coherence of Sentinel-1 data were exploited in order to classify rock glaciers in moving (i.e. with detectable displacement) and no-moving (i.e. without detectable displacement). PS and SBAS multitemporal interferometric techniques were applied with the Sentinel-1 data, and surface displacement maps were obtained. Greater reliability was achieved with the PS technique. Displacement information from PS technique was used to classify the rock glaciers in moving and no-moving. These methods are applicable at a regional scale, thus enabling the rock glacier classification over large areas, where only the geographical location and extent of the landforms is known and no information about their activity is available. If a rock glacier inventory already includes the information on activity, our methods are able to reduce the uncertainties and improve its reliability.

Our methods were developed in South Tyrol, where 1665 rock glaciers were mapped within an inventory, and we classified 270 landforms as moving and 1314 as no-moving with the coherence-based approach, while 144 were classified as moving and 1165 as no-moving with the multitemporal interferometric approach.

The SAR coherence approach has the main advantage to provide an objective detection of the rock glacier activity status, avoiding the subjectivity and the potential misinterpretations that characterize, for example, the visual interpretation of DIn-SAR products. In addition, a SAR coherence approach enables to overcome the complicated phase unwrapping process, required by the traditional DIn-SAR interferometry. The unsupervised approach based on multitemporal techniques allow to classify the rock glacier activity, avoiding the time-consuming classification based on visual evaluation of the SAR products.

Further work is needed to exhaustively define the activity status of rock glaciers at a regional scale (i.e. their activity and ice content), a key task that is still lacking in the inventories. Future work may involve the integration of the information on the activity obtained from our methods with other approaches for ice content detection, and the possibility of using our methods for detecting seasonal and sub-seasonal variations in displacement rates. Furthermore, since the quality of the multitemporal interferometric classification depends on the quality of the displacement maps, future work may involve the improvement of the processing of SAR data in order to obtain more accurate displacement information.

Chapter 3

Exploiting in-situ and satellite approaches to analyse the displacement of Lazaun rock glacier (South Tyrol, Italy) from interannual to hourly scale

Part of this chapter is a paper in preparation and will be submitted presumably to *Earth Surface Processes and Landforms*, by the end of February 2020, as:

Bertone, A.; Zucca, F.; Dematteis, N.; Marin, C.; Notarnicola, C.; Cuozzo, G.; Krainer, K.; Mair, V.; Riccardi, P.; Callegari, M.; Seppi, R. Exploiting in-situ approaches to analyse the displacement of Lazaun rock glacier (South Tyrol, Italy) from interannual to hourly scale.

3.1 Introduction

The interannual and sub-seasonal rock glacier velocities variations are often investigated exploiting in-situ and proximal sensing techniques. In-situ measurements, using ground-based instruments such as topographic total station and GPS surveys (Buchli et al., 2018; Seppi et al., 2019; Strozzi et al., 2010) provide accurate displacement information. However, the displacement information is obtained only on the investigated points, then a large number of points is required for a large spatial coverage. The data acquired from LiDAR and photogrammetry (Westoby et al., 2012), using aerial platforms or Unmanned Aerial Vehicles (UAV), can provide distributed displacement information over a wide area by employing Image Cross-Correlation (ICC) techniques (Groh and Blöthe, 2019; Kaab, 2000; Kääb et al., 2003; Roer et al., 2008; Strozzi et al., 2010, 2004) or comparing Digital Terrain Models (DTMs).

However, the accomplishment of fieldwork to collect in-situ and UAV data is often time-consuming, expensive and difficult to carry out because of the remote areas where the rock glaciers are located. Therefore, only a limited amount of data is typically acquired, which cannot provide the high time resolution required for characterizing the sub-seasonal kinematic variation, which remain poorly investigated.

The technologies that have been recently used to study the sub-seasonal velocity variations are the continuous GPS monitoring systems (Kenner et al., 2017; Wirz et al., 2016), and the Terrestrial Radar Interferometry (TRI) performed by Ground Based Synthetic Aperture Radar (GB-SAR) (Luzi et al., 2004; Monserrat et al., 2014; Pieraccini and Miccinesi, 2019; Rudolf et al., 1999). This instrument can acquire Synthetic Aperture Radar (SAR) images with a very high frequency, providing hourly time series and overcoming the drawback of the low temporal resolution typical of satellite-based SAR interferometry, due to the large revisit period (Monserrat et al., 2014). The potentiality of the GB-SAR to study hourly displacement variations in mountain environments was already tested over landslides (Antonello et al., 2004; Bardi et al., 2016; Corsini et al., 2006; Monserrat et al., 2014; Rouyet et al., 2017; Tarchi et al., 2003) and glaciers (Dematteis et al., 2018, 2017; LIU et al., 2019; LÓPEZ-MORENO et al., 2019), but the application of this instrument over rock glaciers was limited (Buchli et al., 2018) because of the remote areas – often difficult to access – where these landforms are located, and the cost and the availability of this instrument.

An alternative to the ground-based techniques are the remote sensing techniques based on satellite Synthetic Aperture Radar (SAR) (Barboux et al., 2015, 2014; Lambiel et al., 2008; Liu et al., 2013; Necsoiu et al., 2016; Strozzi et al., 2010). SAR satellites provide data over remote areas without field activities, independently from weather conditions and with high temporal frequency (revisit time of few days). Interannual and sub-seasonal velocity variations can be investigated exploiting satellite SAR approaches, avoiding expensive and time-consuming field activities (Barboux et al., 2015, 2014; Necsoiu et al., 2016; Strozzi et al., 2004). However, this technology is affected by issues and limitations, such as the effects of snow and vegetation, atmospheric artefacts, the SAR viewing geometry, and the issues related to the complex

topography of the investigated areas, especially in mountain regions (Barboux et al., 2014). Therefore, the displacement information obtained by this technology should be validated with additional techniques, such as direct measurements.

In this work, we investigated the kinematics of a rock glacier located in Val Senales (South Tyrol, Italy, fig. 3.1), whose internal structure is well known thanks to detailed analysis conducted in the last years (Krainer et al., 2015). In detail, we investigated the rock glacier velocity variations over different temporal scales, exploiting different technologies. Interannual (i.e. from late summer/early autumn to late spring/early summer) and sub-seasonal velocity variations during the summer were analysed using GPS measurements and ICC technique with UAV products. Hourly velocity variations were investigated using the GB-SAR instrument. The results obtained from these different techniques were cross-compared in order to increase their robustness and to extract additional information about the fluctuations in rock glacier velocity.

In order to understand if the rock glacier kinematic can be analysed also when field activities to acquire data cannot be conducted, we exploited several approaches with satellite SAR data acquired from different platforms with different characteristics (i.e. different wavelength, spatial and temporal resolution). In detail, we analysed the seasonal and sub-seasonal rock glacier kinematic using (i) Sentinel-1 data processed with multitemporal interferometric techniques and (ii) TerraSAR X data processed with differential interferometry (DIn-SAR) techniques. We also analysed the annual and interannual rock glacier displacements, by means of TerraSAR X data processed with amplitude tracking techniques Furthermore, the main environmental variables were investigated during the observation period (air and ground temperature, rainfall, spring water temperature), in order to explore their possible interactions with the kinematic behaviour of the rock glacier at the different time scales.

3.2 Study site and methods

3.2.1 Overview of Lazaun rock glacier

The Lazaun rock glacier is located in the upper Val Senales (South Tyrol, northern Italy), coordinates 46°44’49” N and 10°45’20” E (Fig. 3.1). Its elevation ranges from 2480 m to 2700 m asl and its area is of 0.2 km^2. The internal structure of this 700 meters long rock glacier is well known thanks to previous investigation (Krainer et al., 2015), including the study of two boreholes drilled in summer 2010 (Fig. 3.1d). This study investigated the geology of the catchment area, the hydrology of the spring at the front of the rock glacier, and the geomorphology of the rock glacier. Furthermore, a model of the internal structure of the rock glacier was proposed, using the inclinometer measurements, the thermal characteristics of the boreholes, the grain size, ice content, geochemistry, and isotope analyses of the ice cores. Radiocarbon dating and paleoecological studies provided the age of the start of the accumulation phase that is 10250 years old. In the internal model

proposed by Krainer et al (2015), most of the deformation occurs at two shear horizons located close to the base of the rock glacier, and the internal deformation is of comparatively minor importance. The surface displacement was measured between 2006 and 2012 by GNSS measurements, obtaining velocities ranging between 1.4 and 4.5 mm per day. The researches were restarted in the last three years (2016-2018) as part of the ALPSMOTION project, with the aim of further investigate the kinematic behaviour of the rock glacier at finer temporal resolutions (i.e. from hourly to interannual).

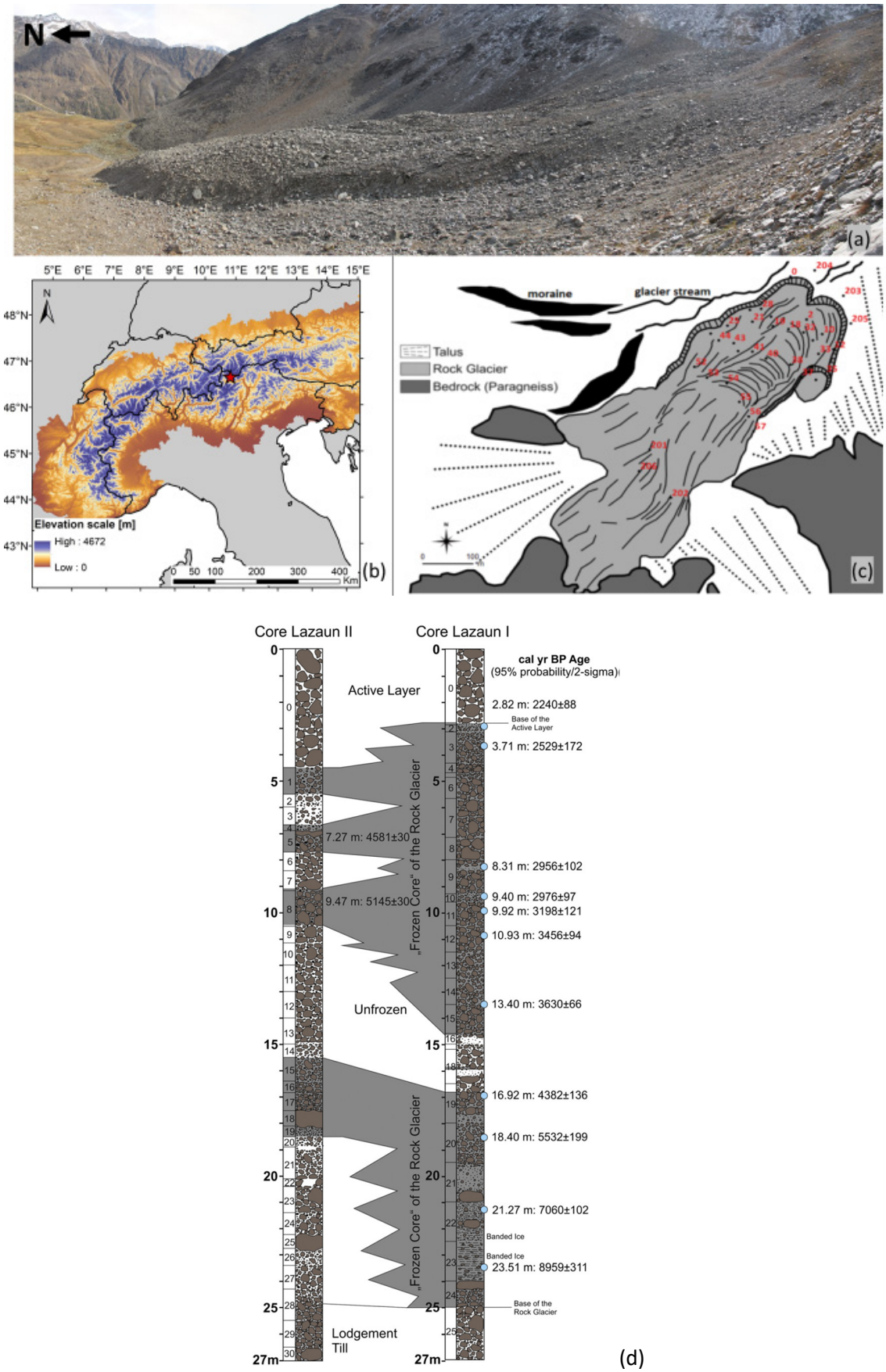

Figure 3.1: (a) picture of the Lazaun rock glacier. (b) Geographical setting and location of the investigated area (red star) in Val Senales, South Tyrol, Italy. (c) Geological scheme of the Lazaun area. Red dots are the GNSS survey markers. (d) Stratigraphy of the two cores extracted from Lazaun rock glacier (from Krainer et al., 2015).

3.2.2 Ground-Based SAR

Three Ground-Based SAR (GB-SAR) field campaigns were conducted using an IBIS-L (Image By Interferometric Survey) instrument in Ku frequency band, designed by IDS (Ingegneria Dei Sistemi) (Fig. 3.2a). GB-SAR images were acquired at 5-minute intervals in VV polarization with a Ground Sample Distance (GSD) of 0.5 meter in range and 4.4 milliradians in azimuth. The field campaigns were conducted from 26/07/2017 to 06/08/2017, from 09/08/2018 to 18/08/2018, and from 13/09/2018 to 03/10/2018 (Tab. 3.1), acquiring 2742, 2365 and 5407 images, respectively. The sensitivity of the IBIS-L GB-SAR instrument is around 0.1 mm and the accuracy depends on the Signal to Noise Ratio (SNR) (Monserrat et al., 2014). In order to increase the SNR (Tarchi et al., 2003), we installed three corner reflectors (CRs) made by aluminium plates, one over bedrock outside the rock glacier, and two on the rock glacier at different distance in range direction (Fig. 3.3). The CR outside the rock glacier was used as reference point during the data processing, while the two CRs on the rock glacier were used to obtain reliable and accurate time series of the surface displacement.

The images acquired by the GB-SAR were processed using Differential Interferometric (DIn-SAR) technique (Luzi et al., 2006, 2004; Monserrat et al., 2014; Noferini et al., 2008). This technique allows to detect the displacement exploiting the difference between the phase of the SAR images acquired at different times. The main advantage of the GB-SAR instrument is the very high acquisition frequency (5 minutes), which enables to analyse the rock glacier displacement at hourly resolution. However, the results are frequently affected by atmospheric effects, especially related to humidity and wind, which has to be properly taken into account.

The processing was conducted using a DIn-SAR interferometric workflow, composed of several steps (Fig. 3.4). The first step is the data selection, to discard the images potentially affected by noise due to short-term variations of the atmospheric conditions (within minutes). The data selection was done choosing a couple of images from stacks of 12 images acquired during each hour. Since the interferometric phase variation over stable areas is due to atmospheric or noise components (Monserrat et al., 2014), we selected the images with the lowest phase variation over stable areas. Therefore, for each stack of 12 images, all the possible interferograms were computed, and the interferogram with the minimum phase variation over the stable area surrounding the rock glacier was chosen. Then, in order to increase the SNR, a coherent sum of the master and slave selected images for each stack was computed. The images obtained by the coherent sum of each stack were used in the DIn-SAR interferometric workflow, in order to compute the final interferograms.

The second and third steps were the interferogram generation and the phase unwrapping, allowing to solve the phase ambiguity. In this last step the interferogram fringes – ranging between $-\pi$ and $+\pi$ – were unwrapped, restoring the physical continuity of the phase map. The following step was the definition of a stable point without displacement, in order to refer the phase to zero. For this purpose, the CR located on bedrock outside the rock glacier was used. In the fifth and sixth steps, the atmospheric phase was estimated

using the Atmospheric Phase Screen (APS) algorithm (Luzi et al., 2004; Noferini et al., 2006) and subtracted from each interferogram. Then the unwrapping step was computed again. The eighth step consisted in the conversion from phase to displacement, and in the geocoding procedure, in order to project the GB-SAR images in geographic coordinates.

DIn-SAR provides only the displacement component along the Line of Sight (LOS), in this study approximately parallel to the longitudinal rock glacier axis. Displacement higher than half of the SAR wavelength (i.e. displacement higher than half of 1.8 cm for the Ku band) are undetectable exploiting this technique (Klees and Massonnet, 1998). However, the hourly displacement of the investigated rock glacier did not exceed half of the SAR wavelength.

Table 3.1: list of the data and their acquisition times.

GB-SAR	**GPS**	**UAV**
From 26/07/2017 to 06/08/2017	06/09/2016	27/09/2016
From 09/08/2018 to 18/08/2018	20/06/2017	20/06/2017
From 13/09/2018 to 03/10/2018	23/08/2017	23/08/2017
	12/10/2017	12/10/2017
	27/06/2018	28/06/2018
	27/09/2018	21/09/2018

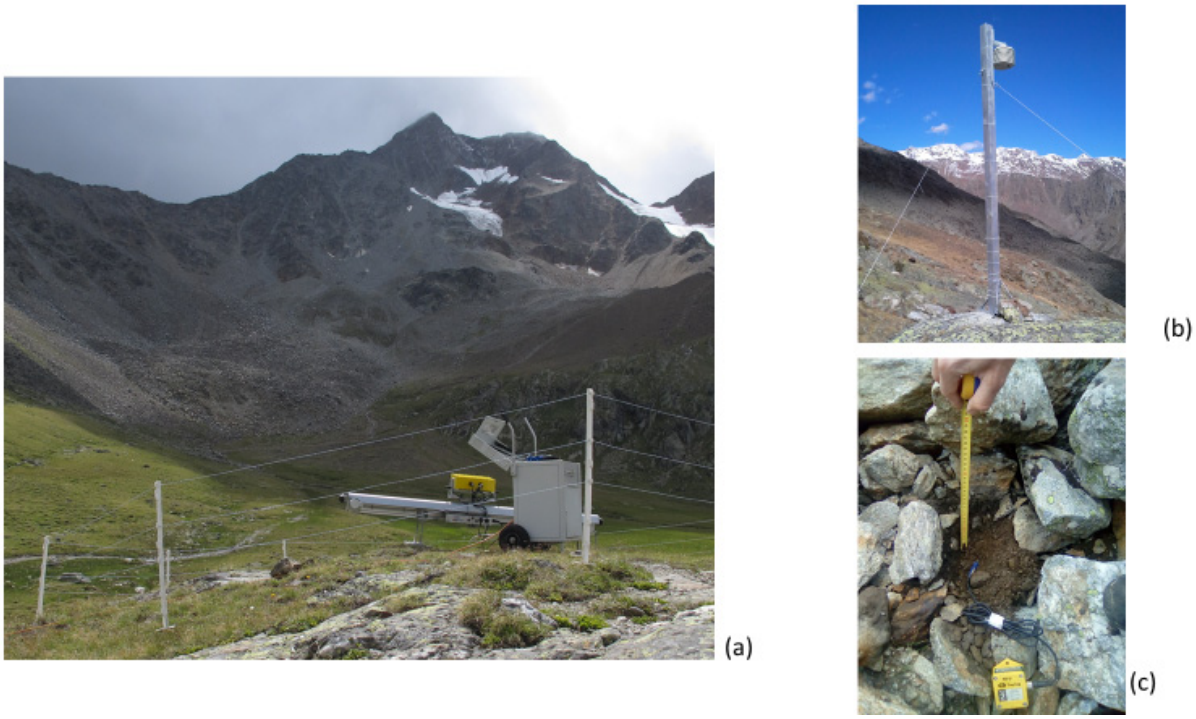

Figure 3.2: (a) the GB-SAR instrument used for monitoring the surface displacement of the Lazaun rock glacier (on the left background). (b) the air temperature datalogger, (c) one of the GST dataloggers.

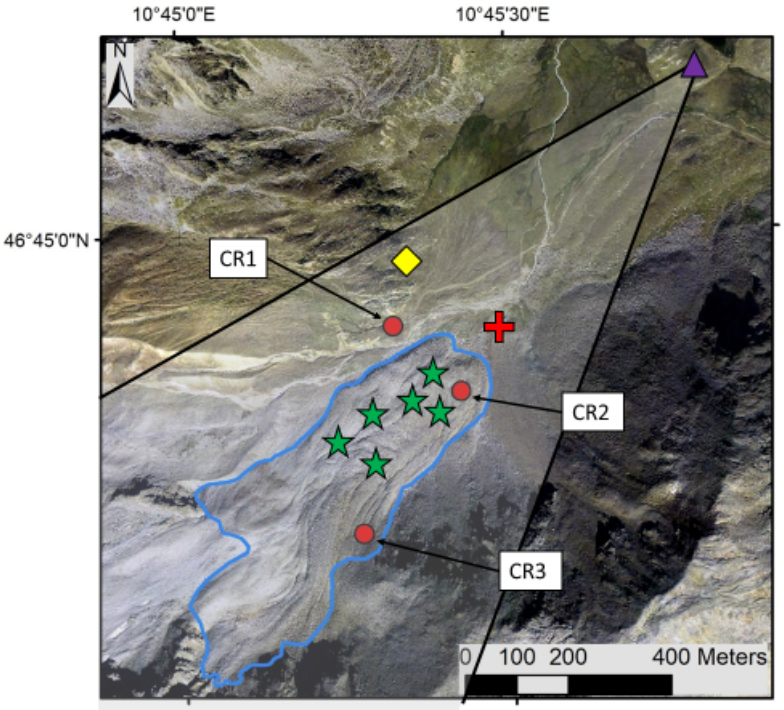

Figure 3.3: the area investigated by the GB-SAR. The blue line represents the rock glacier outline, the purple triangle is the location of the instrument, the red dots are the location of the CRs. The yellow diamond is the location of the air temperature datalogger, the red cross is the location of the spring water temperature datalogger, and the green stars are the location of the GST dataloggers.

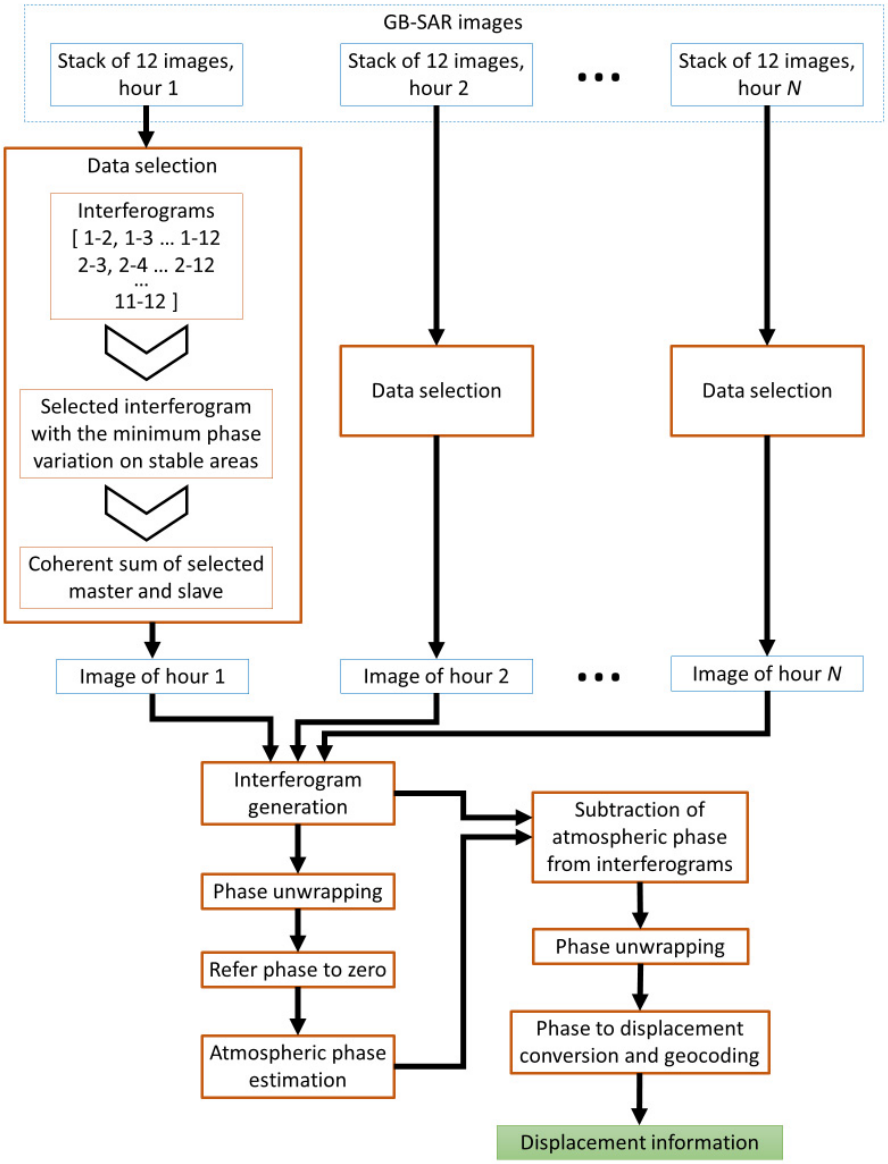

Figure 3.4: Scheme of the GB-SAR data processing workflow.

3.2.3 UAV

Six UAV campaigns were conducted between the summer 2016 and 2018 within the ALPSMOTION project (Tab. 3.1), in order to acquire the images used for the photogrammetric DTM generation, which was used for describing the surface displacement with high spatial resolution and wide spatial coverage. The campaigns were conducted using a hexacopter (Surveying Robot Mk.AD) equipped with a Sony A6000 camera (24-mm-focal length) which recorded an area of 0.16 km^2 within a flight time of 15 min at a flight altitude of 92 m above ground level. The photogrammetric processing was done using the Pix4D software. The georeferencing step in UTM32 projection was conducted using about 79 Ground Control Points (GCP) marked and measured by Global Navigation Satellite System (GNSS) during each flight campaign. Therefore, the planimetric and

vertical precisions are around 3 cm. From the photogrammetric processing, orthophotos with a GSD of 3 cm and 3D point clouds with a point sampling distance of 6 cm were obtained. DTMs with a GSD of 10 cm were obtained from the triangulation of the point clouds. Hillshaded maps with cell size of 10 cm were generated, using a sun light direction of 40° and an elevation of 45°.

To investigate the rock glacier displacement between the 2016 and 2018 the Image Cross Correlation (ICC) technique was used (Kaab, 2000; Strozzi et al., 2010, 2004) (Fig. 3.5). The displacements were computed between each pair of consecutive images. In particular, the analysis were conducted using the COSIcorr software (Ayoub et al., 2009; Leprince et al., 2007). Since the orthophotos were acquired in different months, different light conditions existed. Therefore, to avoid the problems related to shadows, the ICC technique was applied to the hillshaded maps derived from the photogrammetric DTMs acquired with UAVs (Table 3.1).

The software enabled us to calculate planimetric displacements, which were derived from the matching of the multitemporal hillshaded maps (Ayoub et al., 2009; Leprince et al., 2007). After several tests, we optimized a window correlation size of 64 pixel and a sliding step of 4 pixel. The minimum displacement detectable by COSIcorr is theoretically 1/20 of the pixel size, and the greater the displacement, the better the estimate (Leprince et al., 2007).

A large number of GCPs were used during the georeferencing process. The coregistration between the hillshaded maps was checked on stable areas outside the rock glacier.

In order to compare the planimetric displacement detected by ICC from UAV data with the displacement detected by the GB-SAR along the LOS, we reprojected the planimetric displacement detected by ICC along the LOS of GB-SAR. The reprojection was conducted using the following cross product:

$$s_{los} = \bar{d}_{icc} * \hat{l}$$

(3.1)

Where s_{los} is the reprojected displacement along the LOS, the displacement vector $\bar{d}_{icc} = (d_x, d_y)$ is the vector displacement measured by the ICC along the North-South direction (d_y) and the East-West direction (d_x), and $\hat{l}$ is the unit vector of the LOS. Vertical displacement was not taken into account.

The ICC technique is able to provide only the two components of the planimetric displacement. The vertical displacement was estimated computing the Difference of DTM (DoD). In detail, the 21/09/2018 DTM was subtracted to the 27/09/2016 DTM. The DoD was also used to compute elevation changes inside the rock glacier, which were used to calculate volume changes.

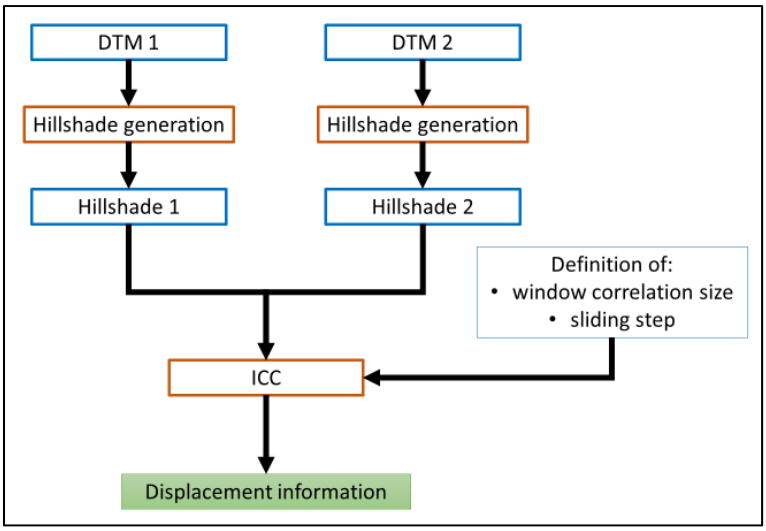

Figure 3.5: Scheme of the ICC processing with UAV data.

3.2.4 GPS

During the ALPSMOTION project six field campaigns were conducted with GPS in Real Time Kinematic (RTK) mode, with the signal correction from a base-station less than 2 km far. With this configuration, the planimetric precision was around 1–2 cm, the altimetric precision was around 2–3 cm. Table 4.1 shows the time of the surveys. A geodetic network of 57 survey markers and 7 fixed control points in front of the rock glacier was established in August 2006. During the years, 5 marker points were lost and therefore the network of effectively measured points during the six field campaigns conducted between 2016 and 2018 was composed of 52 marker points.

The positions measured by the GPS for each survey marker were used to compute the 3D displacement for each time interval investigated between 2016 and 2018 (Strozzi et al., 2010). Since the GPS is the only technique used in this work able to provide the rock glacier displacement on the three spatial dimensions (i.e. North-South, East-West and vertical), the GPS results were compared with the UAV and GB-SAR results. In detail, the planimetric displacement detected by ICC from UAV data was compared with the planimetric displacement detected by GPS, and the displacement detected by GB-SAR along the LOS was compared with the displacement detected by GPS and reprojected along the LOS. The reprojection was conducted using the following cross product:

$$s_{los} = \bar{d}_{gps} * \hat{l}$$

(3.2)

Where s_{los} is the reprojected displacement along the LOS, the displacement vector $\bar{d}_{gps} = (d_x, d_y, d_z)$ is the vector displacement measured by the GPS along the North-South direction (d_y), the East-West direction (d_x) and the vertical direction (d_z), and $\hat{l}$ is the unit vector of the LOS.

3.2.5 TerraSAR-X

Five TerraSAR X (TSX) images were acquired the 18/08/2016, 14/07/2017, 05/08/2017, 16/08/2017, 16/09/2018 and 27/09/2018, with a minimum repeat-pass time interval of 11 days (Fig. 3.6). The images were acquired in descending geometry, VV polarization, staring spotlight mode, and with a 5 km swath and a spatial resolution of 90 cm in range and 16 cm in azimuth.

TSX images were used to study with high spatial details the rock glacier surface kinematic, whereas the Sentinel-1 images are not adequate because they have a low spatial resolution (20 meters). The TSX images were processed using Differential Interferometry (DIn-SAR,(Barboux et al., 2014; Osmanoğlu et al., 2016; Strozzi et al., 2010, 2004), which allows detecting displacements along the LOS exploiting the difference between the phase component of two SAR images, acquired at different times.

The first step in the DIn-SAR processing workflow (Fig. 3.7a) was the computation of the phase difference between the master and slave images. The three investigated couples of images are between the periods 14/07/2017 and 05/08/2017, 05/08/2017 and 16/08/2017, 16/09/2018 and 27/09/2018 (Fig. 3.8a). Since displacements along the LOS larger than half of the SAR wavelength (e.g. displacement higher than half of 3,1 cm for the X band) are undetectable exploiting this technique, a maximum temporal baseline of 22 days was taken into account, in order to avoid large rock glacier displacements. For this reason, the DIn-SAR technique was useable only for sub-seasonal analyses of displacements. The interferograms were generated using a multilooking 4 in azimuth in order to increase the Signal to Noise Ratio (SNR).

The second step consisted of the phase unwrapping, allowing to solve the phase ambiguity. Then we defined a point without displacement in order to refer the phase to zero, selecting for this purpose a point located on stable bedrock outside the rock glacier. The last step was the conversion from phase to displacement, and the geocoding procedure, in order to project the SAR images in geographic coordinates.

In the investigated area the vegetation is absent, and the snow cover was avoided working on images acquired in the snow-free periods. The main errors sources are atmospheric phase distortions, signal noise, and inaccuracies in the orbit determination. However, these errors can be neglected in our case study because they only affect large areas.

The calculated displacement along the LOS was reprojected along the line of maximum slope, which is the direction of rock glacier displacement (Section 3.3.1.3). The reprojection was performed by means of the following cross product relationship:

$$s_{los} = \bar{d}_{sd} * \hat{l}$$

(3.3)

Where s_{los} is the displacement information obtained along the LOS, the displacement vector $\bar{d}_{sd} = (d_x, d_y, d_z)$ is the vector displacement along the line of maximum slope for the three components along the North-South direction (d_y), the East-West direction (d_x) and the vertical direction (d_z), and $\hat{l}$ is the unit vector of the SAR LOS. $\bar{d}_{sd}$ was computed from this equation. However, during the reprojection step the errors associated with each measurement are amplified. The greater the angle between the LOS direction and the maximum slope direction, the greater the amplification of the errors associated with each measurement. Therefore, to limit this issue, we reprojected only the measurements with an angle smaller than 60° between the LOS and the maximum slope.

Because of the above mentioned limitation of the TSX DIn-SAR technique in detecting displacements larger than half of 3.1 cm, it was replaced by the amplitude tracking technique for analyses of displacements across longer time periods (Michel et al., 1999; Sánchez-Gámez and Navarro, 2017). This approach exploits the amplitude information of two SAR images acquired at different times, and provides the displacement information applying the Image Cross-Correlation (ICC) algorithm (Hu et al., 2014; Michel et al., 1999; Rott et al., 1998; Wang and Jónsson, 2015). Since the amplitude tracking technique is more suitable for detecting large displacements, large time intervals (i.e. annual) have been taken into consideration. The three investigated periods analysed were from 18/08/2016 to 16/08/2017, from 16/08/2017 to 27/09/2018, and from 18/08/2016 to 27/09/2018 (Fig.3.8b).

The first step of the processing workflow (Fig. 3.7b) was the extraction of the amplitude of SAR images. Afterwards, the ICC algorithm was applied, using a cross-correlation window size defined by a kernel window of 32 pixels in range and 64 pixels in azimuth, as optimized after several tests. The following step was the definition of a stable point without displacement, in order to refer the displacement to zero. In the final step the displacement information obtained by ICC in unit pixel was converted in meters and the SAR image was geocoded, in order to project the SAR image in geographic coordinates.

Similar to the DIn-SAR approach, this technique is also affected by signal noise and inaccuracy in the orbit determination, however they are negligible in this case because they mainly regard areas larger than the investigated landform. The phase unwrapping step – essential in the interferometric techniques – is not necessary with the amplitude tracking technique. Compared to the interferometric techniques, the accuracy of amplitude tracking techniques is generally lower (Simons and Rosen, 2007).

Amplitude tracking provides the displacement components along two directions: one along the LOS (i.e. along the range direction of SAR image) and the other one along the azimuth (AZ) direction (nearly parallel

to the North-South direction). This technique is not able to detect the real 3D rock glacier displacement, because a third component would be needed in addition to the LOS and AZ components. Therefore, the displacement components along the LOS and AZ were combined to obtain the rock glacier displacement information, assuming that the rock glacier displacement takes place along a plane. We assumed a parallel plane to the topographic surface, then exploiting the combination of the two known components we defined the module and the direction of the displacement parallel on this plane. The equation was solved exploiting the following cross product relationships:

$$\begin{cases} \bar{d}_{sd} * \hat{r} = d_{los} \\ \bar{d}_{sd} * \hat{a} = d_{fly} \\ \bar{d}_{sd} * \hat{n} = 0 \end{cases}$$

(3.4)

Where the $\bar{d}_{sd} = (d_x, d_y, d_z)$ is the vector displacement along the plane for the three components along the North-South direction (d_y), the East-West direction (d_x) and the vertical direction (d_z), d_{los} is the obtained displacement along the LOS, d_{fly} is the obtained displacement along the AZ direction, $\hat{r}$ is the unit vector of the LOS, $\hat{a}$ is the unit vector of the AZ direction and $\hat{n}$ is the unit vector of the line normal to the plane and perpendicular to the surface topography. During this combination step the errors associated with LOS and AZ components are amplified. Here we introduce the alpha angle (α), defined as an angle generated by the intersection between the plane which includes the LOS and AZ vectors and the plane parallel to the topographic surface. The greater the α angle, the greater the amplification of the errors associated with LOS and AZ components. Therefore, to avoid a large amplification of errors, only the LOS and AZ measurements with an α angle less than 60° were combined. This assumption allowed improving the accuracy of the displacement direction exploiting only one SAR relative orbit.

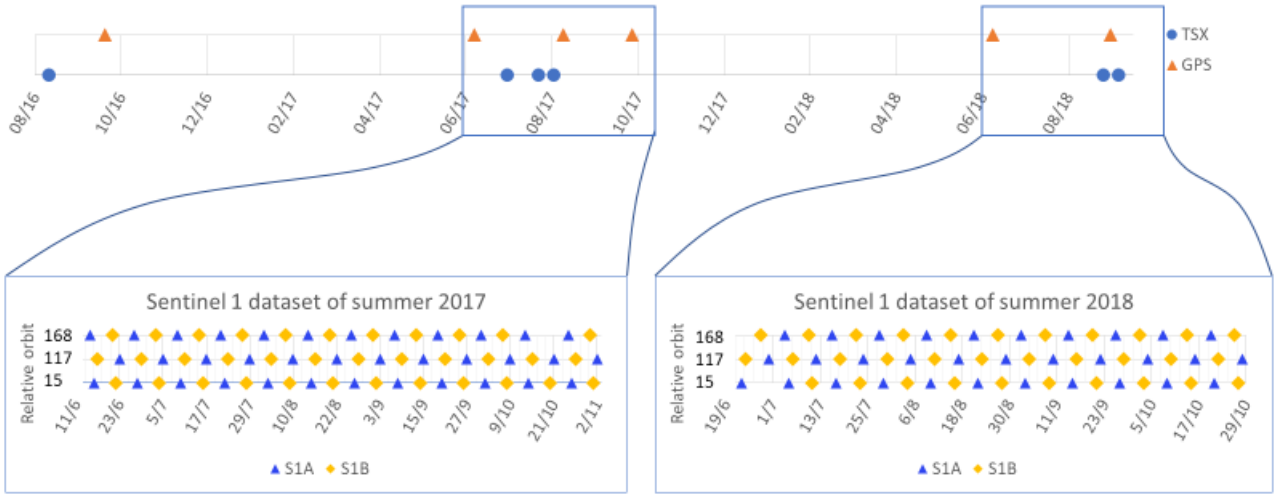

Figure 3.6: list of the different dataset used. In the upper part the blue dots show the acquisition time of the TSX images, and the orange triangles show the acquisition time of the GPS data. In the lower part the Sentinel-1 images acquired during the summer 2017 and 2018.

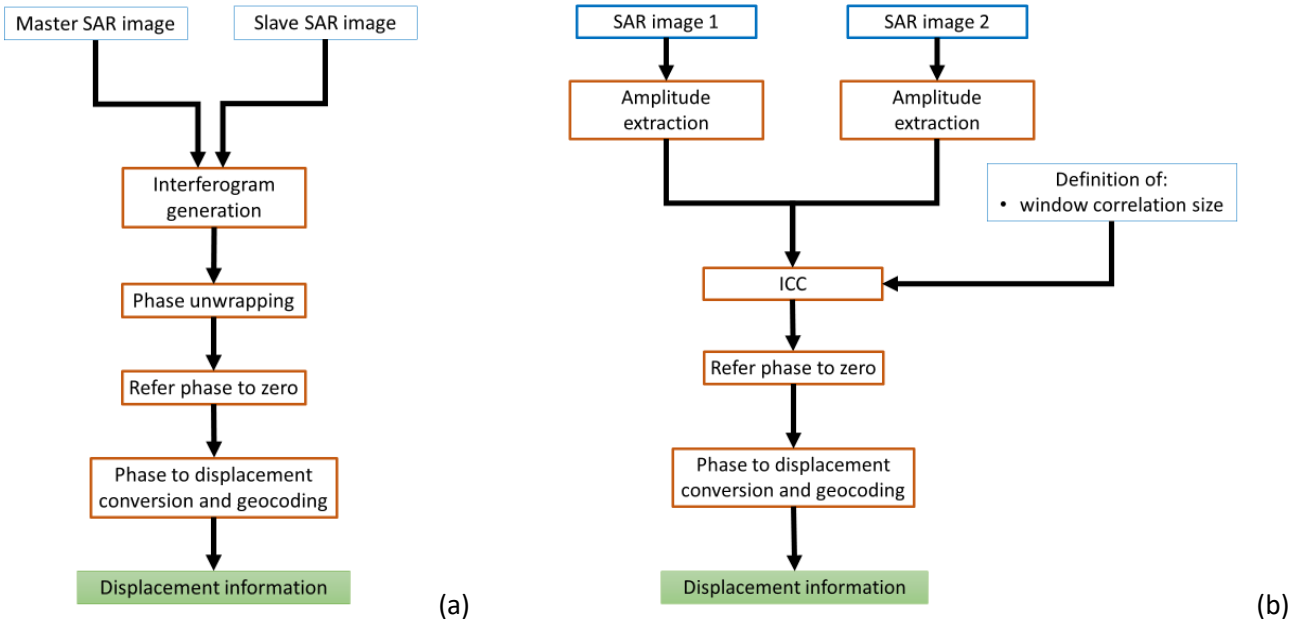

Figure 3.7: (a) scheme of DIn-SAR technique. (b) scheme of amplitude tracking technique.

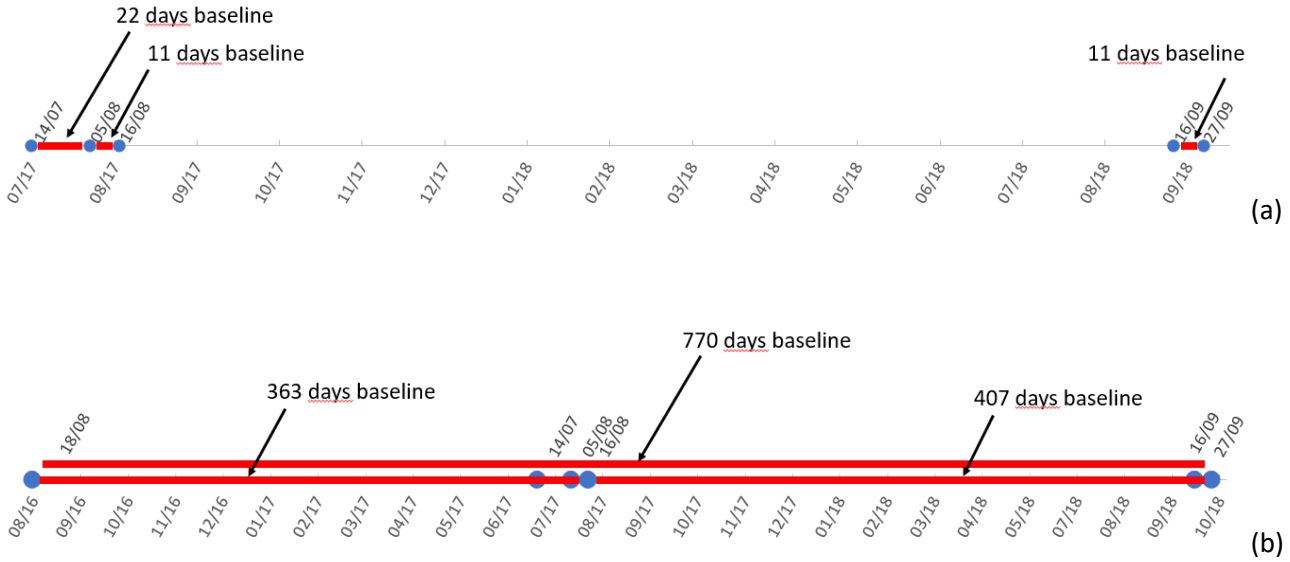

Figure 3.8: time lines of the TSX images (blue dots). (a) The red line shows the investigated time interval exploiting the DIn-SAR technique. (b) The red line shows the investigated time interval exploiting the amplitude tracking technique.

3.2.6 Sentinel-1

Three Sentinel-1 tracks, i.e. relative orbit 15, 117 (ascending) and 168 (descending), cover the Lazaun area. Sentinel-1 images are acquired in Interferometric Wide swath (IW) mode with a 250 km swath at 5 m by 20 m spatial resolution (single look). Single Look Complex (SLC) product type and VV polarization data were used in this work. We took into account all the images acquired by the Sentinel-1A and Sentinel-1B platforms during the snow-free period 2017 and 2018 (Fig. 3.6). The absence of snow was checked with optical images acquired from Sentinel 2. 2.7 2.2.3.1

The high acquisition time frequency of Sentinel-1 data (every 6 days for each relative orbit) enables to study the seasonal rock glacier displacements and to highlight the displacement variations during the entire snow free period. The images acquired during the summer 2017 and 2018 were processed using two different multitemporal interferometric techniques: Persistent Scatter (PS) (Ferretti et al., 2001) and Small BAseline Subset (SBAS) (Berardino et al., 2002). These techniques were already described in section 2.2.3.1 (Fig. 2.7). Both allow to obtain only the displacement along the LOS of the satellite (Hu et al., 2014). The main advantage of these multitemporal approaches are the strong reduction of phase errors such as atmospheric artefacts or topographic residuals, using a large number of SAR images (Osmanoğlu et al., 2016).

As done for the DIn-SAR with the TSX data, the displacements obtained along the LOS component were reprojected along the maximum slope direction (equation 3.3). The reprojections allow to compare the results obtained from different geometries (i.e. ascending and descending) and from different platforms (i.e. Sentinel-1 and TSX) used in this work.

3.2.7 Environmental variables

Six temperature dataloggers (Tinytag TGP 4020) equipped with an external probe were installed on the rock glacier in summer 2017 to monitor the Ground Surface Temperature (GST, Fig. 3.2c). The probes were placed under a few decimetres of fine-grained terrain, in order to shield them from the solar radiation (Fig. 3.2c and Tab. 3.2). The GST dataloggers were installed in areas with different displacement values (Fig. 3.3). The dataloggers have an accuracy of ±0.35°C between -40 and +125°C, and measured instantaneous temperature with hourly resolution. Their accuracy was checked using the zero curtain temperature in the snowmelt phase (Outcalt et al., 1990) and they did not required recalibration. Unfortunately, two of the installed GST sensors didn't record data due to battery failure. One further datalogger of the same type was installed in autumn 2017 to measure the air temperature close to the rock glacier using an external probe housed inside a Davis 7714 passive radiation shield (Fig. 3.2b). Finally, in summer 2018 one further temperature datalogger with external probe was installed in the spring emerging at the rock glacier front, in order to measure the spring water temperature. Rainfall data were taken from an automatic weather station of the Bolzano Province (Vernago weather station), located 4 km South-East of the rock glacier.

The GST data were used to extract some information related to the thermal regime of the ground (Kellerer-Pirklbauer and Kaufmann, 2012). In particular, we calculated the length of the zero curtain period, i.e. a phase at stable 0°C temperature of the ground corresponding to the melting period of the snow cover in spring (Outcalt et al., 1990). The length of the zero curtain may provide an indirect information on the thickness of the snow layer above the measuring point.

Table 3.2: description of the locations where the GST dataloggers were installed.

	Tessiture	**Slope [°]**	**Aspect [°]**	**Altitude [m]**
GST 1	soil, grain size < 1 mm	22	10	2580
GST 2	soil, grain size < 1 mm	12	359	2595
GST 3	soil, grain size < 1 mm	10	359	2638
GST 4	soil, grain size < 1 mm	16	57	2600
GST 5	soil, grain size < 1 mm	10	62	2599
GST 6	soil, grain size < 5 mm	17	30	2654

3.2.8 Error analysis and data comparison

Since each technique is affected by errors, for each measure we evaluated the accuracy and the precision. The accuracy was evaluated computing the mean displacement over stable areas, and the precision was evaluated computing the standard deviation of displacement over the same stable areas. The stable areas

were chosen close to the front and lateral slopes of the rock glacier, on rock outcrops or in flat areas where soil creep processes do not occur.

To evaluate the suitability of each technique, we cross-compared the daily velocities obtained by each approach used in this work. Qualitative evaluation was shown by the scatterplot, while as a quantitate evaluation we computed the Root Mean Square Difference (RMSD). RMSD is frequently used for comparing predicted and observed values. We also computed the Spearman's correlation coefficient (ρ) which is a nonparametric measure of rank correlation. It assesses how well the relationship between two variables can be described using a monotonic function (whether linear or not). It ranges between -1 (i.e. observations have a dissimilar rank between the two variables) and +1 (i.e. observations have a similar rank between the two variables).

3.3 Results

3.3.1 In-situ and proximal sensing approaches

3.3.1.1 Ground-Based SAR

From the GB-SAR data we obtained high resolution displacement maps of the entire rock glacier (Fig. 3.9). With the geocoding procedure a spatial resolution of 1m was obtained. The fastest areas with velocities higher than 2 mm/d are located above the frontal slope and in the central part of the rock glacier, while in the North-West area the velocity is lower (< 1 mm/d). The velocity was lower in July and August, and increased in September. As can be observed in figure. 3.9, the maximum velocities were around 2 mm/d in the first two periods and 3 mm/d in the last period, indicating an acceleration towards the end of the summer.

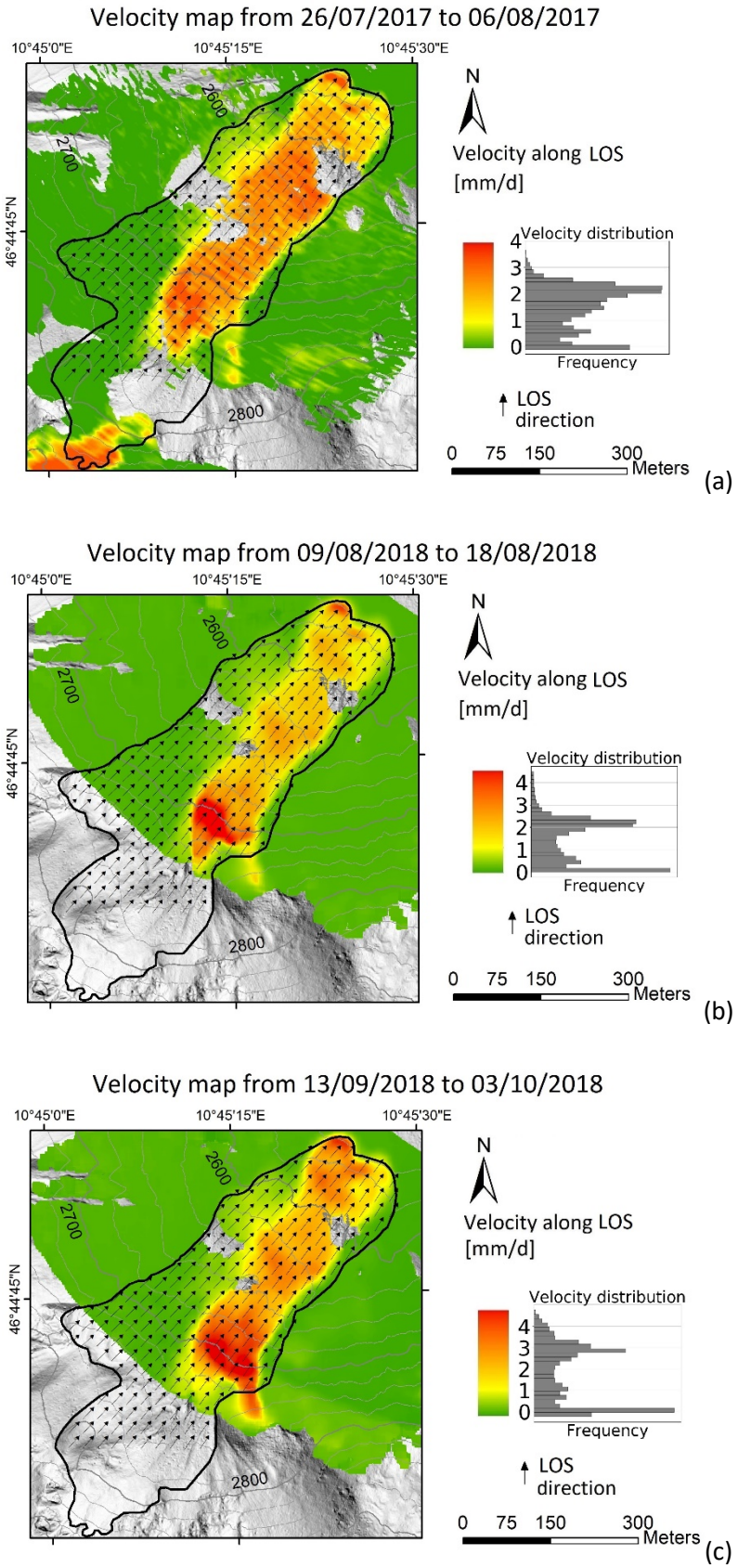

Figure 3.9: velocity maps obtained by the GB-SAR instrument in July 2017 (a), August 2018 (b) and September 2018 (c). The velocities are obtained along the LOS and are showed by colours. Black arrows represent the LOS direction.

The figure 3.10 shows the time series of the two measurement periods acquired in summer 2018. We computed the cumulative displacement of four points located on the rock glacier in areas with different mean velocities and of other four points located on stable areas outside the rock glacier (Fig. 3.10a). Along with the displacement data, figure 3.10 shows the environmental variables recorded in the same periods, i.e. the air temperature, precipitation, spring water temperature and the GST (average of four dataloggers).

The points located on the rock glacier have different cumulative displacement, with minimum values for the point located in the 'slow zone' shown in figure 3.10b and 3.10c (green line), and maximum values for the point located in the 'upper zone' (blue line). The displacement of the four points follows the same pattern and shows a "step-like" cumulative movement. The displacement mainly occurs during very short time intervals (about in 3 hours), alternated with longer phases of apparent stagnation (about 20 – 21 hours). For example, in August the displacement follows a very regular rhythm and occurs around midnight of each day, with movements around 2 – 4 mm in 3 hours (Fig. 3.10b). During the other intervals the variation of cumulative displacement is almost zero. In September and October (Fig. 3.10c) the displacement has the same pattern and occurs between midnight (more frequently in late September) and twelve o'clock (more frequently in mid-September) of each day, with movements around 4 – 6 mm in 3 hours.

The mean displacements over stable areas outside the rock glacier are -0.3 mm, 0.13 mm and -0.42mm, and standard deviations are 0.41 mm, 0.14 mm and 0.54 mm for the summer 2017, August 2018 and September/October 2018 field campaigns, respectively. Therefore, the sensitivity and the accuracy of displacements measured by GB-SAR are very high, and the results are not affected by strong noise or error generated during the data processing. The slight decrease visible in the cumulative displacement is related to residual noise. The cumulative displacement measured in the stable areas outside the rock glacier is very low, ranging between -0.5 mm and 0.5 mm. In August, no anomalies are visible in the cumulative displacement of the stable points, while for the September/October anomalous displacements between -1 mm and 2 mm are visible from 21st to 24th September and from 1st to 3rd October. These anomalies could be related to changes of the weather conditions, which may disturb the radar signal. During the first anomaly (21st September – 24th September) a decrease in air temperature and precipitation are observed at the end of this anomaly. This anomaly could be related to change of other physical parameters not measured, as for example the air humidity. During the second anomaly (1st October – 3rd October) a decrease in air temperature and precipitation are observed in the same time.

Rapid decrease of the spring water temperature (up to 0.14 °C) are related to rainfall events, but not all rainfall events generate a decrease in the spring water temperature. In August four rainfall events are visible, of which two generate a decrease of the spring water temperature when the amount of water is higher than 2 mm per day. In the period monitored during August 2018 the air temperature was quite stable. In September six main rainfall events are visible. Unfortunately, the spring water temperature time series is

incomplete, however two rapid decrease of the spring water temperature related to rainfall events are visible, associated also to decreasing air temperature. In September two minimum temperatures are measured, one in 25 September, one in 2 October. Around these time intervals, maximum cumulative displacement values around 2 mm are measured over the stable areas, while the movements inside the rock glacier decrease. Therefore, during these time intervals with minimum air temperature, the rock glacier movements decrease from 4 – 6 mm to 2 – 3 mm in 3 hours. The GST behaviour is very similar to that of air temperature. The GST is higher than air temperature, due to the increased heating of the soil.

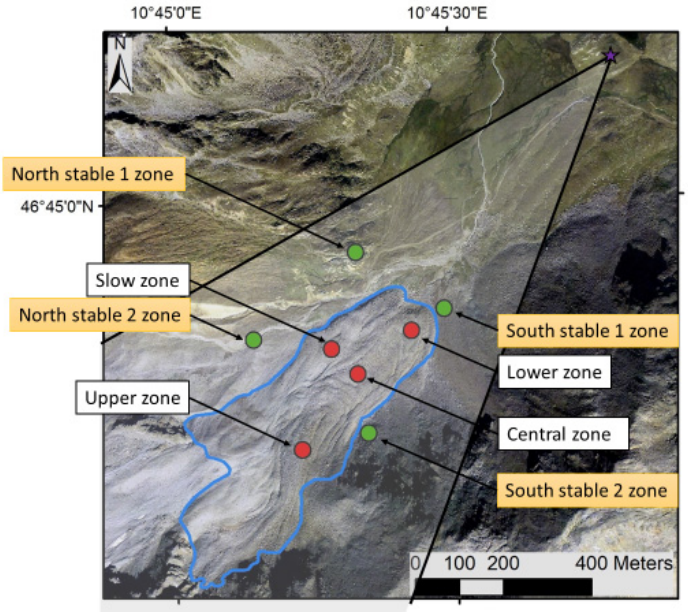

(a)

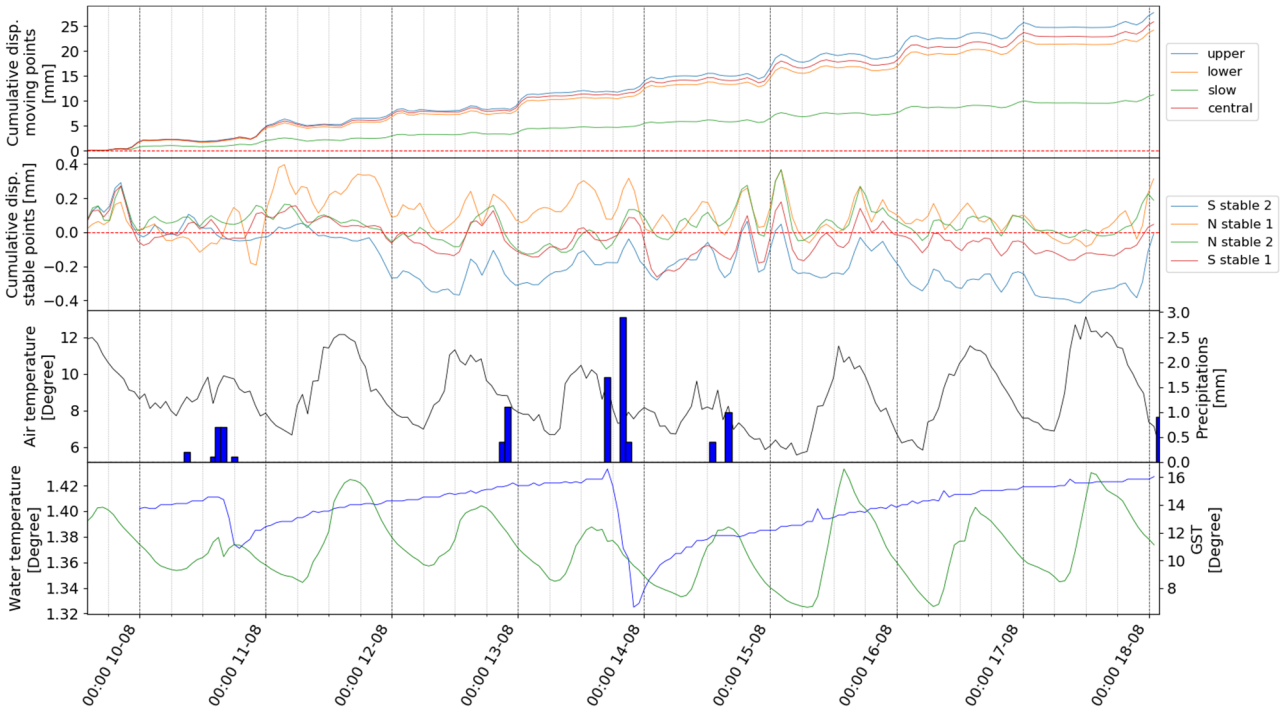

(b)

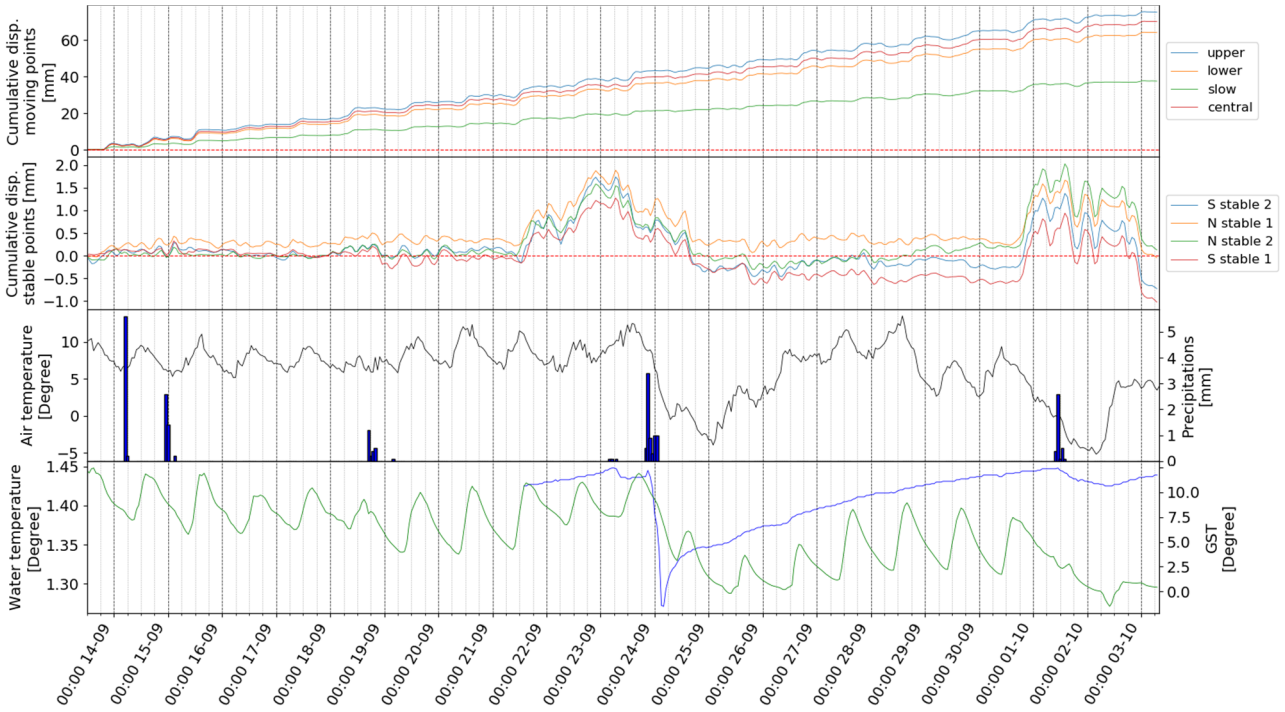

(c)

Figure 3.10: (a) position of points located inside the rock glacier (red) and outside (green) where the time series were computed, including the Lazaun rock glacier outline (blue line) and the investigated area by the GB-SAR. Time series obtained from the field measurements conducted with the GB-SAR instrument in August (b) and September (c) 2018. For each time series we plotted the cumulative displacement along the LOS of four points located in sectors with different mean velocities inside the rock glacier, the cumulative displacement of four points located in stable areas outside the rock glacier outline, in the first and second subplots, respectively. In the third subplot the air temperature measured close to the rock glacier in black, and the precipitations measured by a weather station located 4 Km far from the rock glacier in the blue bars. In the fourth subplot the water temperature measured in spring water close to the frontal part of the rock glacier in blue, and the average of the GSTs measured by four instruments. The instantaneous temperatures are measured with hourly resolution.

3.3.1.2 UAV results

The results obtained by the ICC using the UAV acquisitions provided the displacement maps with a high spatial resolution (0.4 meters) and the planimetric direction of the displacement (Fig. 3.11 and 3.12). The measurements conducted between 2016 and 2018 provided also a detailed sub-seasonal time series. The velocity map obtained with the largest time interval (27/09/2016 to 21/09/2018, 724 days) (Fig. 3.11) shows that the fastest areas are located above the frontal slope and in the middle part of the rock glacier, while in the North-West area the velocity is lower. The upper part of the rock glacier was not investigated by the UAV. For each investigated period (Fig. 3.12), the lower velocities were obtained in the summer times, while higher velocities were obtained in the periods between the autumn and spring. The displacements on stable areas outside the rock glacier are very low, with mean values between 18 mm and 53 mm, and standard deviation between 9 mm and 23 mm (Tab. 3.3).

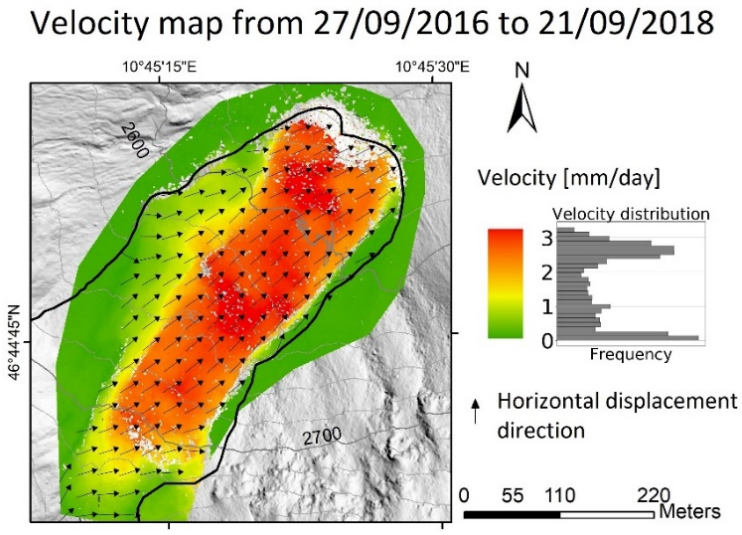

Figure 3.11: velocity map obtained by ICC between 27 September 2016 and 21 September 2018, i.e. the largest time interval. The colours represent the intensity of the velocity in mm per day; the black arrows represent the planimetric direction of the displacement.

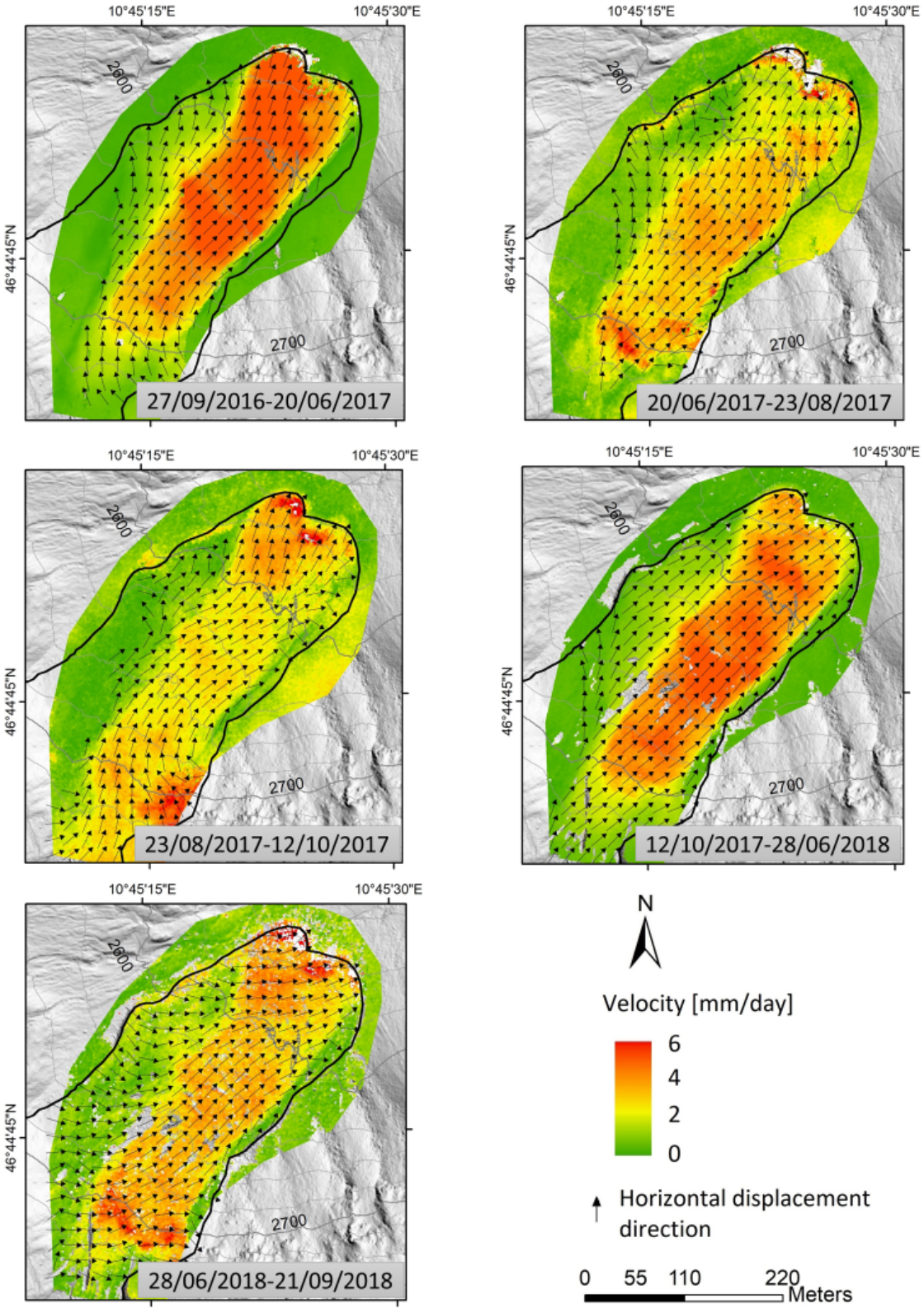
10°45'15"E
10°45'30"E
46°44'45"N
2800
2700
27/09/2016-20/06/2017
20/06/2017-23/08/2017
23/08/2017-12/10/2017
12/10/2017-28/06/2018
28/06/2018-21/09/2018
N
Velocity [mm/day]
6
4
2
0
Horizontal displacement direction
0 55 110 220
Meters

(a)

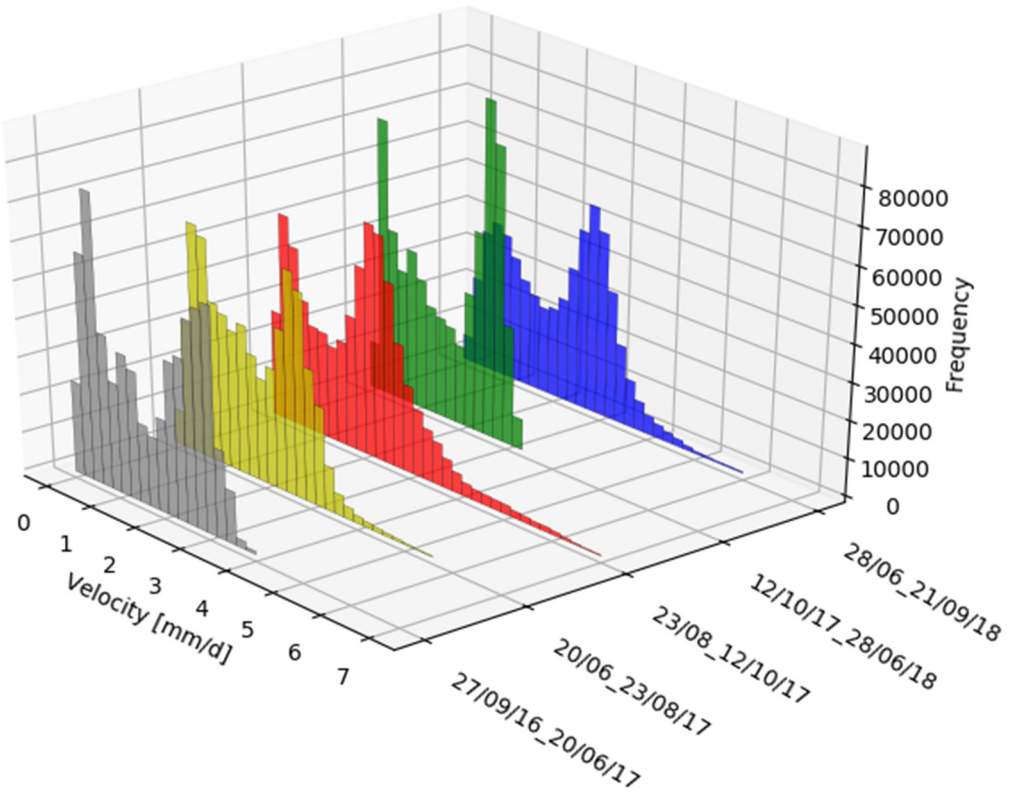

(b)

Figure 3.12: (a) velocity maps obtained for each investigated time interval with ICC. The colours represent the velocity in mm per day; the black arrows represent the planimetric direction of the displacement. (b) frequency distribution of the planimetric velocity obtained for each investigated time interval.

Table 3.3: mean cumulative displacement values and standard deviation over the stable areas for each investigated period using UAV ICC.

Date	Days	Mean [mm]	Standard deviation [mm]
27/09/2016 – 20/06/2017	266	39	18
20/06/2017 – 23/08/2017	64	28	14
23/08/2017 – 12/10/2017	50	18	9
12/10/2017 – 28/06/2018	259	40	21
28/06/2018 – 21/09/2018	85	53	23
27/09/2016 – 21/09/2018	724	33	15

The DoD was computed by subtracting the DTM of 21/09/2018 from the DTM of 27/09/2016 (Fig. 3.13). A large area in the upper part of the rock glacier is characterized by subsidence. Small areas with uplifts appear because of the planimetric displacement in correspondence of steep slopes, on the downstream side of

ridges and of the front. DoD ranges between -1 m and 1 m. The total volume change inside the rock glacier was computed as -5100 m^3 (volume lost) between the two DTMs.

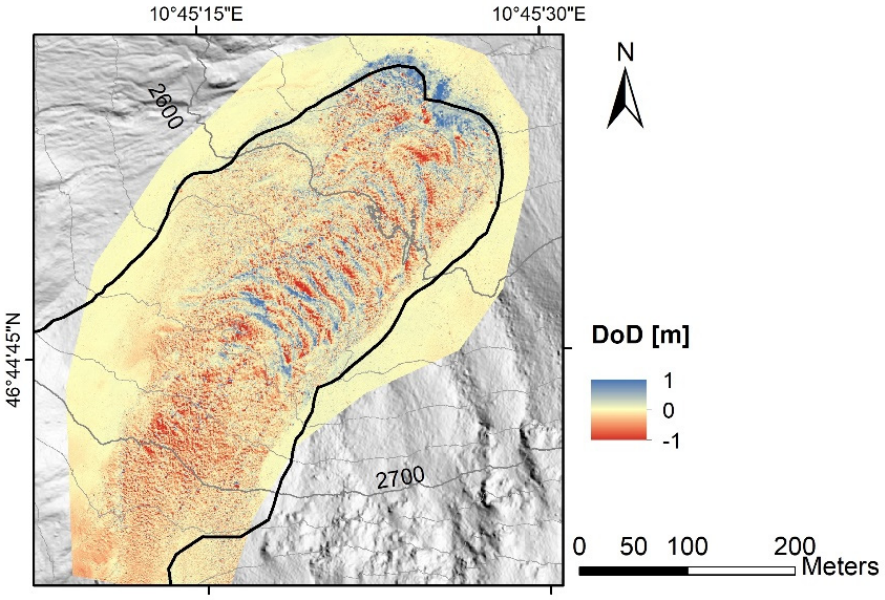

Figure 3.13: DoD computed between the 21/09/2018 and the 27/09/2016. Red colour represents subsidence, blue represent uplift.

3.3.1.3 GPS results

The GPS surveys provided the 3D displacement of the measured points from September 2016 to September 2018 (Fig. 3.14). High flow velocities were recorded in a 110 – 120 m wide zone along the rock glacier axis, while lower flow velocities were recorded near the boundary of the rock glacier. The zone with high flow velocities includes the survey markers located in the central zone, with velocities higher than 2.5 mm/day. The zone with low flow velocities is located in the North-West margin, with velocities lower than 1.5 mm/day. The displacement direction provided by the GPS is approximately parallel to the rock glacier axis, with the exclusion of the markers close to the lateral slope where the displacement direction is oriented with the maximum local slope. The marker points located outside the rock glacier area recorded a mean displacement value of 41 mm, with a standard deviation of 19 mm

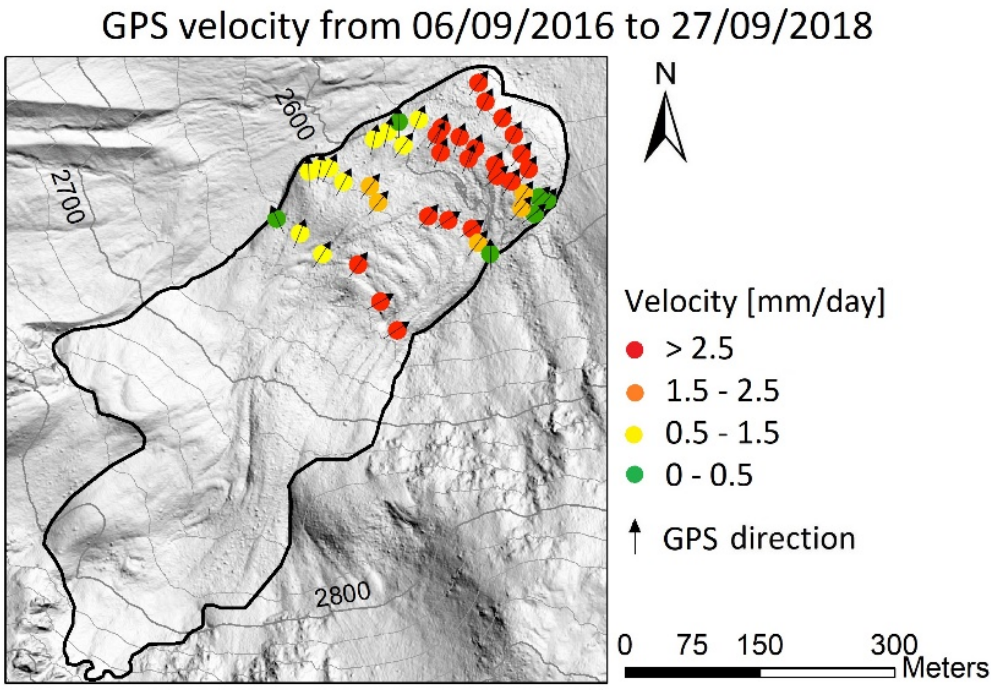

Figure 3.14: velocities obtained by the GPS survey from the 06/09/2016 to 27/09/2018. The arrows represent the direction obtained by the GPS, the colour dots represent the magnitude of the 3D displacement in millimetres per day.

As we wanted to analyse the relationship between the rock glacier displacement direction and the topography, we compared the real 3D displacement direction provided by the GPS with the maximum slope direction provided by the DTM. The terrain aspect and slope information were extracted from the grids of terrain slope and aspect extracted from the UAV DTM of 21/09/2018. A window size of 10 meters was used to compute these models, in order to avoid the effect of surface roughness due to presence of large blocks. For each GPS marker we computed (i) the difference angle between the azimuth of the GPS vector and the azimuth of the terrain aspect, and (ii) the difference angle between the vertical inclination of the GPS vector and the vertical inclination of the terrain slope. The results are showed in boxplots (Fig. 3.15). The difference angles are very low, with mean values around 7° and 3° for the azimuth and the vertical inclination, respectively. This means that the direction of the rock glacier displacement is approximately parallel to the maximum slope direction, as observed in figure 3.15.

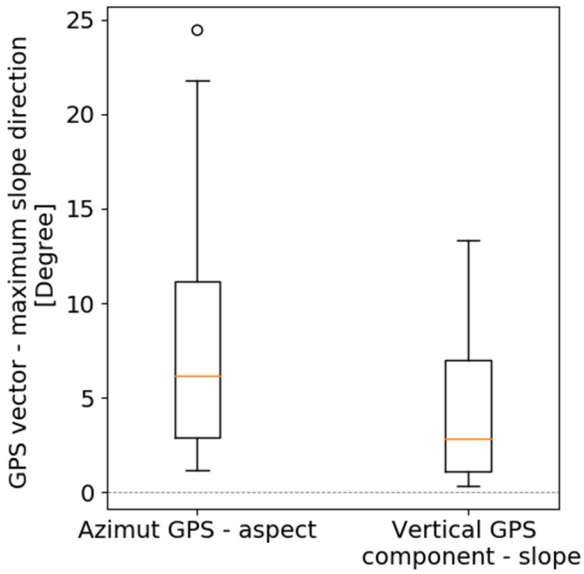

Figure 3.15: on the left, the boxplot of the difference angles computed between the azimuth of the GPS vector and the azimuth of the terrain aspect; on the right, the boxplot of the difference angles computed between the vertical inclination of the GPS vector and the vertical inclination of the terrain slope. Mean values are lower than 10°.

3.3.1.4 Time series analysis

In order to better understand the seasonal and sub-seasonal velocity variations, we plotted in a single graph the velocities obtained by the different techniques in correspondence of a selected number of the GPS survey markers, separating the fast (central part) from the slow (North-West part) rock glacier zones (Fig. 3.16a). In detail, we plotted the mean velocity of the selected GPS survey markers obtained by (i) GPS, (ii) GB-SAR, and (iii) ICC technique with UAV data (Fig. 3.16b). Daily air temperature, precipitations and GST are also plotted for comparison.

Focusing on the two summer periods, a velocity increase is observable between the end of June and the beginning of October on the fast zone (Fig. 3.16b). Since during the summer 2017 three UAV and GPS surveys were conducted, an increase of velocity from 2.3 – 2.5 mm/d to 3 – 3.1 mm/d was detected. In summer 2018, only two UAV and GPS campaigns were conducted, then velocity changes are not detectable using these techniques. However, the two GB-SAR campaigns detected an increase of velocity from 2.15 mm/d in August to 2.9 mm/d at the end of September 2018. Focusing on the slow zone (Fig. 3.16b), during 2017 the GPS measurements showed an increase of velocity from 0.5 to 0.9 mm/d, while UAV observed a decrease from 0.7 mm/d to 0.45 mm/d. These different trends are probably related to the technological limit of the ICC, due to the low displacement of this area that is close to the sensitivity of the ICC technique. During the summer 2018 the two GB-SAR field campaigns showed an increase of velocity from 0.6 mm/d in August to 1 mm/d at the end of September 2018.

Additional analysis was conducted to investigate the interannual periods (i.e. between early autumn and late spring) exploiting the UAV and the GPS techniques (Fig. 3.16b). The velocities measured by the ICC and GPS

between September 2016 and June 2017 are 3 mm/d and 3.4 mm/d, respectively, for the fast zone, while 0.85 mm/d and 1.2 mm/d, respectively, for the slow zone. Lower velocities are obtained between October 2017 and June 2018. In detail 2.7 mm/d and 2.75 mm/d are measured by the cross-correlation and GPS, respectively, for the fast zone, while 0.9 mm/d and 0.95 mm/d, respectively, for the slow zone.

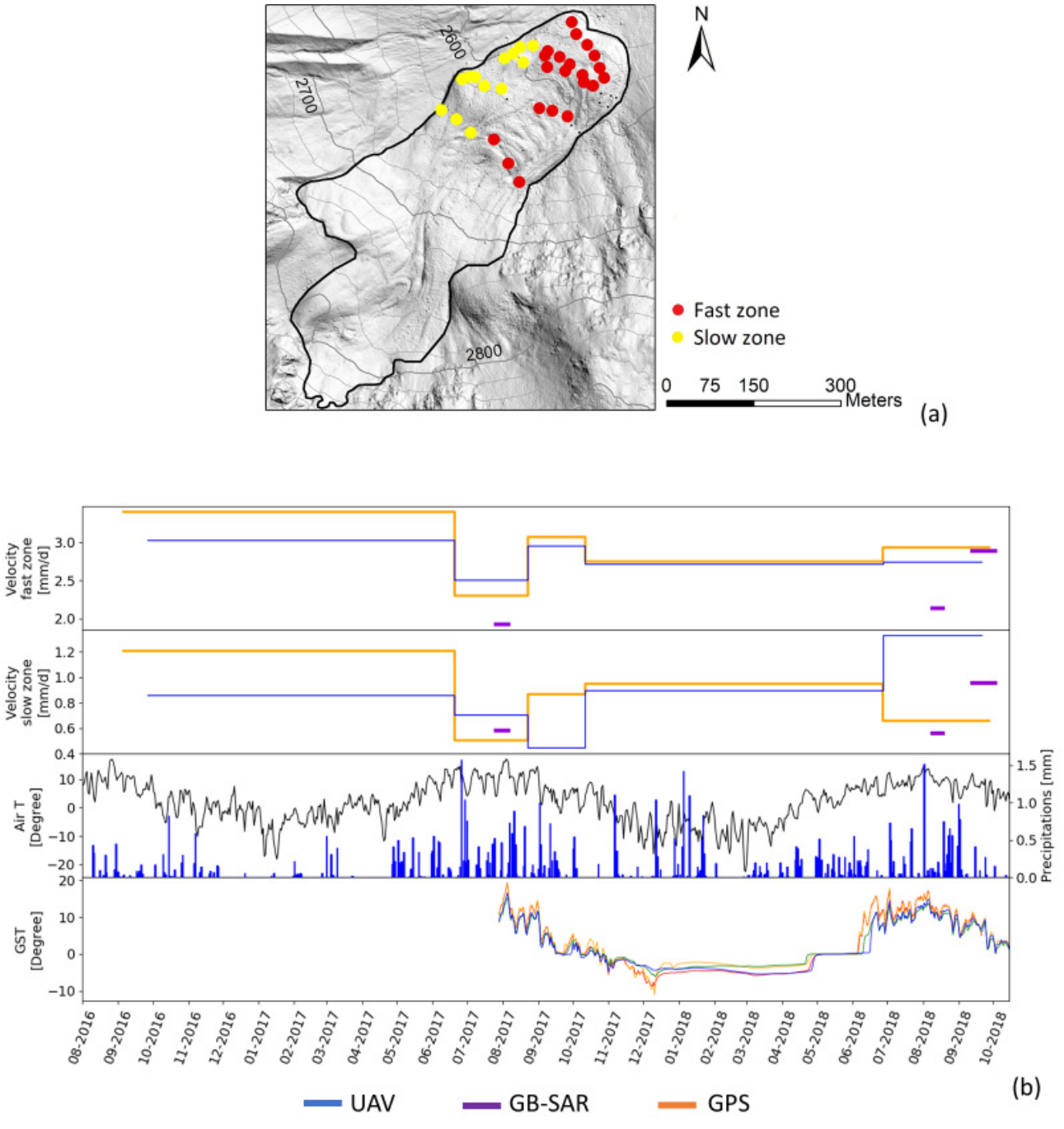

Figure 3.16: (a) location of the GPS survey marks used to analyse the velocities obtained by the different techniques in the fast rock glacier zone (red marks) and in the slow rock glacier zone (yellow marks). The average velocities obtained in the fast rock glacier zone (central part) and in the slow rock glacier zone (North-West part) are showed in the graph b. In violet the velocities obtained by GB-SAR along the LOS, in blue the planimetric velocities obtained by ICC, and in orange the 3D velocities obtained by GPS technique. Daily air temperature, daily precipitation and GST are also showed. The trend of air temperature before autumn 2017 was reconstructed by exploiting the air temperature measured by a meteorological station located 6 km from the rock glacier.

3.3.1.5 Data comparison

The UAV and GB-SAR techniques are not able to provide the displacement information along the three spatial components (i.e. North-South, East-West and vertical). Therefore, the planimetric displacement information obtained by UAV was compared with the planimetric displacement provided by the GPS, excluding the vertical component measured. The displacement information obtained by the GB-SAR along the LOS was compared to the GPS, projecting the GPS displacement vector along the LOS (Equation 3.2). The comparison GB-SAR – UAV was conducted comparing the GB-SAR displacement information obtained along the LOS with the UAV planimetric displacement reprojected along the LOS (Equation 3.1). However, since the acquisition times of GB-SAR data are quite different from UAV and GPS, good results are not expected.

The comparison UAV – GPS provides good results (Fig. 3.17a), with RMSD ranging between 0.11 mm/day and 0.74 mm/day, and ρ ranging between 0.67 and 0.98 (Tab. 3.4). In detail, lower RMSD values and higher ρ values are obtained when larger time intervals are evaluated, because ICC better enables disentangling displacements from errors.

With the comparison GB-SAR – GPS (Fig. 3.17b) the RMSD and ρ are 0.47 mm/day and 0.66 (2017 measurements), 0.25 mm/day and 0.97 (August 2018 measurements) and 0.70 mm/day and 0.91 (September 2018 measurements), respectively (Tab. 3.4). These different values are explained by the different acquisition time of the GB-SAR data and the GPS measurements, since each technique provides velocities information for different time intervals.

The comparison GB-SAR – UAV is similar to the GB-SAR – GPS comparison (Fig. 3.17c). RMSD and ρ values are 0.42 mm/day and 0.8 (2017 measurement), 0.47 mm/day and 0.88 (August 2018 measurement) and 0.68 mm/day and 0.77 (September 2018 measurement), respectively (Tab. 3.4).

The scatterplots obtained with the GB-SAR results of September 2018 showed an offset compared to the UAV and GPS results (Fig. 3.17b and 3.17c). These offsets are generated by the different recorded velocities, because the times of acquisition of GB-SAR and GPS/UAV measurements are different. In detail, the GB-SAR velocities are overestimated because the GB-SAR velocities recorded during the field campaign of September 2018 are higher than the velocities recorded by GPS and UAV during the entire 2018 summer season.

For the same reason another offset is visible from the scatterplot between UAV and GPS of September 2016 and June 2017 (Fig. 3.17a). In detail, the GPS velocities are overestimated because the GPS velocities recorded from 16/09/2016 to 20/06/2017 are higher than the velocities recorded by UAV from 27/09/16 to 20/06/17.

Table 3.4: Matrix of RMSDs and ρ coefficients resulting from the comparison of displacements measured with different techniques.

		UAV					**GB-SAR**		
		27/09/16 to 20/06/17	20/06/17 to 23/08/17	23/08/17 to 12/10/17	12/10/17 to 28/06/18	28/06/18 to 21/09/18	26/07/17 to 06/08/17	09/08/18 to 18/08/18	13/09/18 to 03/10/18
GPS	16/09/2016 to 20/06/2017	RMSD: 0.31 ρ: 0.98							
	20/06/2017 to 23/08/2017		RMSD: 0.64 ρ: 0.67				RMSD: 0.47 ρ: 0.66		
	23/08/2017 to 12/10/2017			RMSD: 0.48 ρ: 0.89					
	12/10/2017 to 27/06/2018				RMSD: 0.11 ρ: 0.96				
	27/06/2018 to 27/09/2018					RMSD: 0.74 ρ: 0.82		RMSD: 0.25 ρ: 0.97	RMSD: 0.70 ρ: 0.91
GB-SAR	26/07/2017 to 06/08/2017		RMSD: 0.42 ρ: 0.8						
	09/08/2018 to 18/08/2018					RMSD: 0.47 ρ: 0.88			
	13/09/2018 to 03/10/2018					RMSD: 0.68 ρ: 0.77			

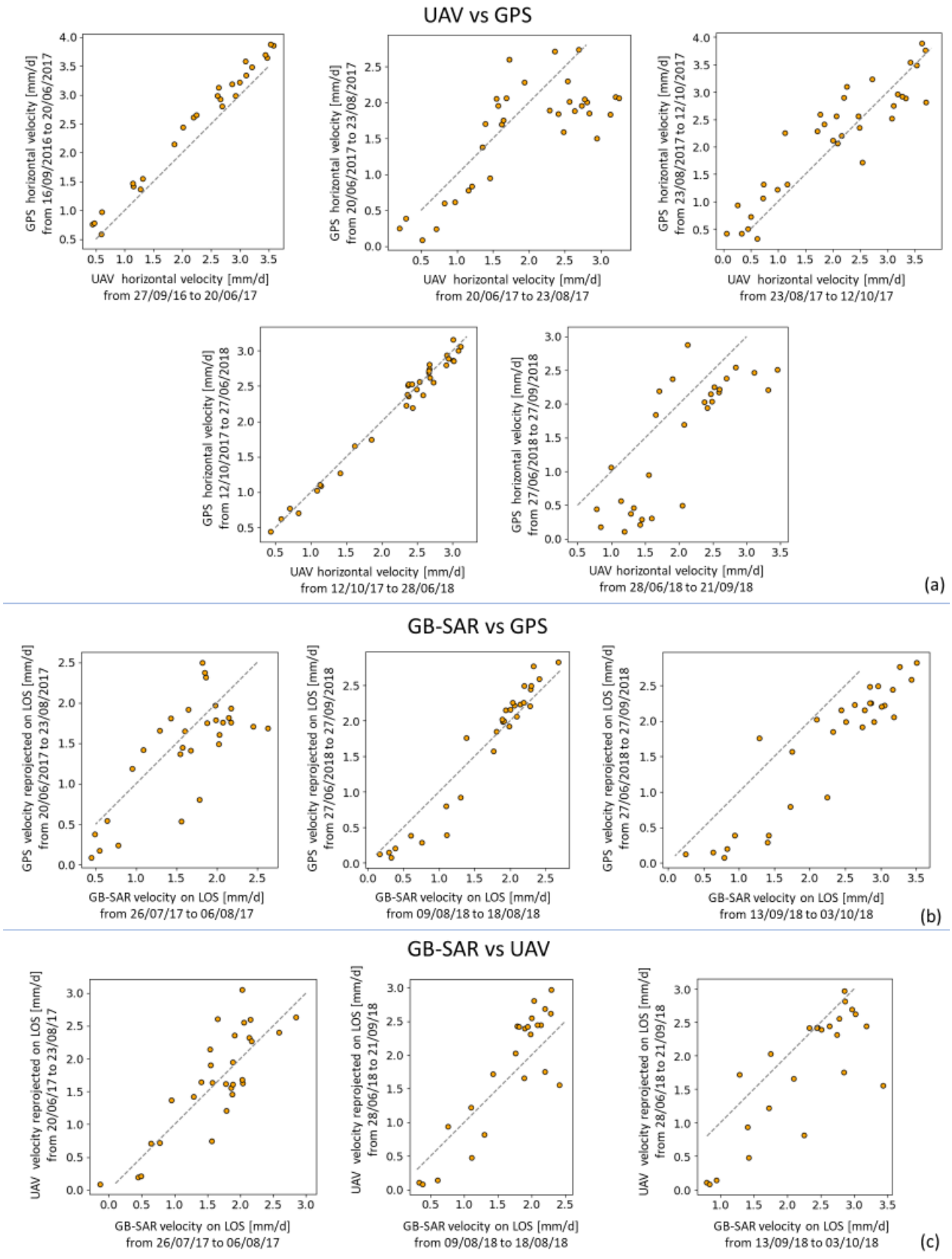

Figure 3.17: Scatterplots comparing surface displacement measured with different techniques.

The GPS is the only technique able to provide the 3D displacement direction, which can be separated in the North-South, East-West and vertical components. Therefore, we compared the North-South and East-West components detected by the ICC between 27/09/2016 and 21/09/2018 (724 days) with the same components detected by the GPS between 16/09/2016 and 27/09/2018 (741 days) (Fig. 3.18). Since between 27/09/2016 and 21/09/2018 the vertical displacement was calculated from the DoD, we were able to compare this component to the vertical component measured by the GPS. The North-South and East-West components estimated by the ICC are very similar to those obtained by the GPS, with RMSD of 0.09 mm/day for both and ρ values of 0.96 (East-West component) and 0.98 (North-South component). The vertical component detected by the DoD show a larger scatter, however the results are satisfactory (RMSD = 0.59 mm/day and ρ = 0.48).

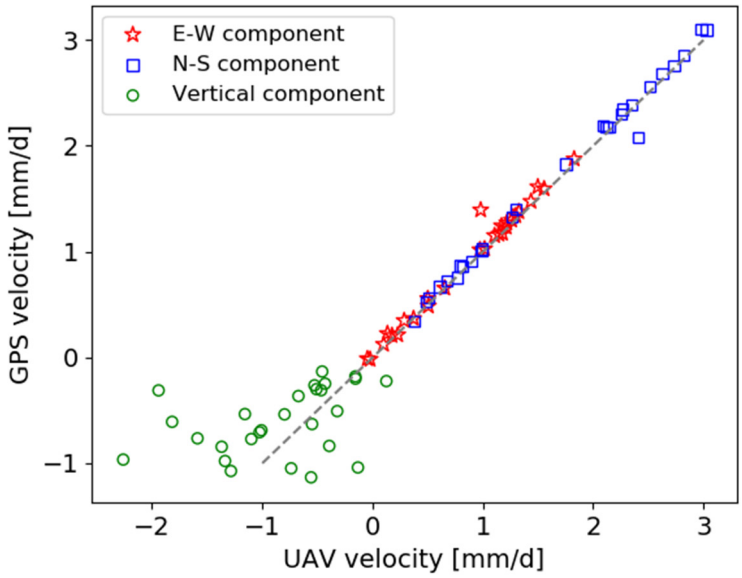

Figure 3.18: comparison between UAV and GPS results obtained during the time interval 27/09/2016 – 21/09/2018. In red and blue the comparison between ICC and GPS for the East-West and North-South components, respectively. In green the comparison between the DoD and the vertical component measured by the GPS.

3.3.1.6 Velocity transects

In order to highlight the spatial variability of surface displacements, we plotted the planimetric velocity estimated by the ICC and the vertical velocity derived from the DoD in the time interval between 27/09/2016 and 21/09/2018, along a longitudinal profile and a transversal profile (Fig. 3.19). The longitudinal profile (Fig. 3.19b) shows constant planimetric velocities inside the rock glacier area, with values around 2 - 3 mm/day, with a decrease in the rooting zone (South-West). The vertical velocity in the rooting zone (South-West) suggests subsidence, while in the central and frontal parts (North-East) the vertical velocity shows subsidence alternated with uplift, due to the planimetric displacement in correspondence of steep slopes, for example

of large rock blocks or transversal ridges. The transversal profile (Fig. 3.19c) shows asymmetries of the planimetric velocities inside the rock glacier area, with lower velocities in the North-West part, and higher velocities in the South-East part. This planimetric velocity distribution is well visible also in the previous velocity maps. In the North-West part the planimetric velocity increases slowly, while it decreases rapidly towards the south-eastern margin of the rock glacier, after a 'plateau' zone with velocity exceeding 2.5 - 3 mm/day. The vertical velocity oscillates around zero along the entire transversal profile.

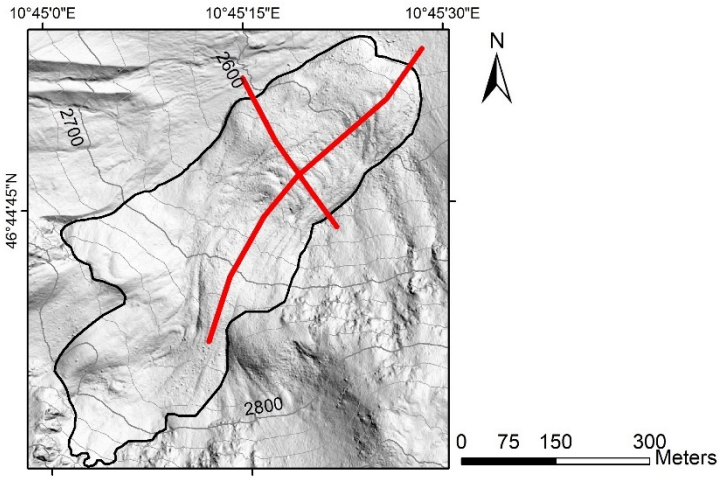

(a)

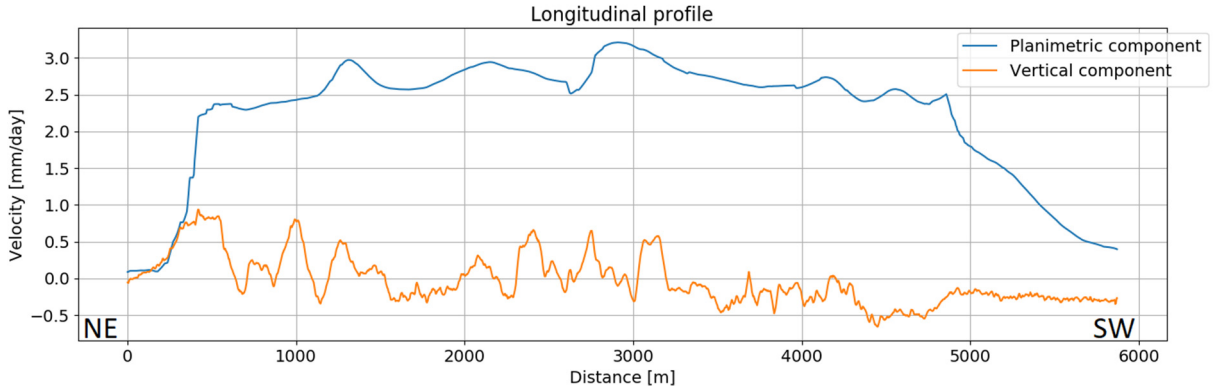

(b)

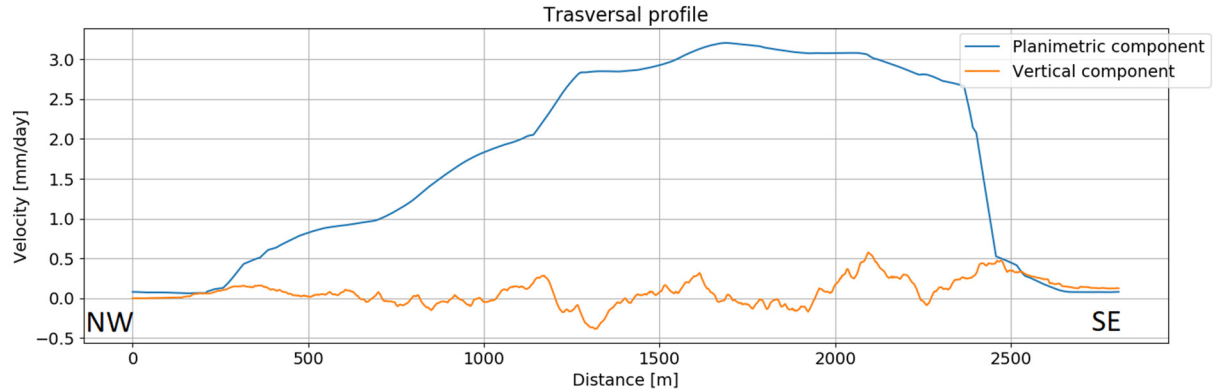

(c)

Figure 3.19: (a) traces of the longitudinal and transversal profiles. (b) Longitudinal profile. (c) Transversal profile. In blue the planimetric velocity, in orange the vertical velocity.

3.3.2 Satellite SAR-based approaches

In this section we present the results obtained from satellite SAR-based approaches, in order to test the feasibility in case of field data cannot be acquired.

3.3.2.1 TerraSAR-X results

The high-resolution velocity maps (spatial resolution of 1 meter after the geocoding procedure of TSX data) in figure 3.20 show the rock glacier velocity for the investigated periods, obtained using the DIn-SAR technique, with the LOS displacement reprojected along the slope direction. The fastest areas are located above the frontal slope and in the middle part of the rock glacier, while in the North-West area the velocity is lower. Lowest velocities are obtained in July, while higher velocities are obtained in September, indicating an acceleration towards the end of the summer. The displacements on the stable areas are very low, with mean values of 2.2 mm, 0.1 mm and 1.4 mm, and standard deviation of 0.5 mm, 0.6 mm and 0.8 mm for the first, second and third investigated period, respectively.

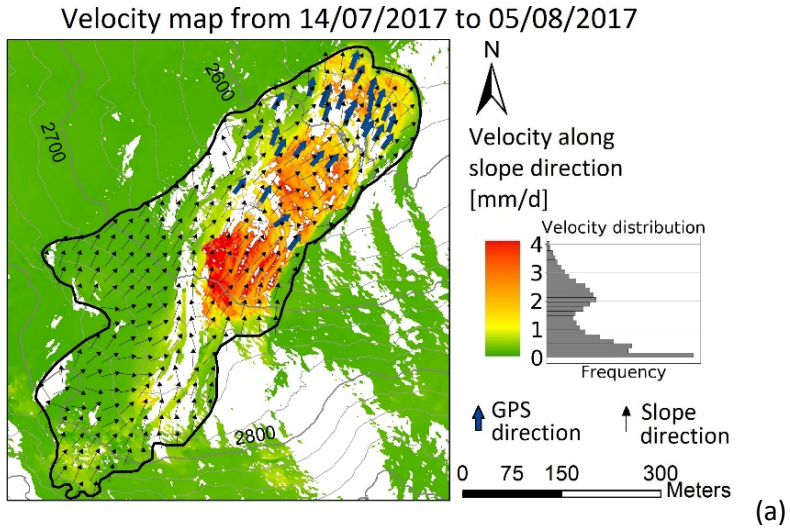

(a)

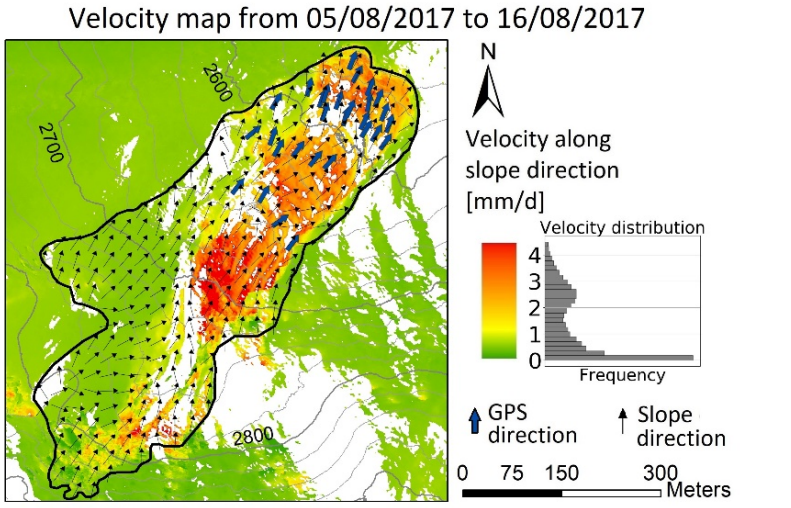

(b)

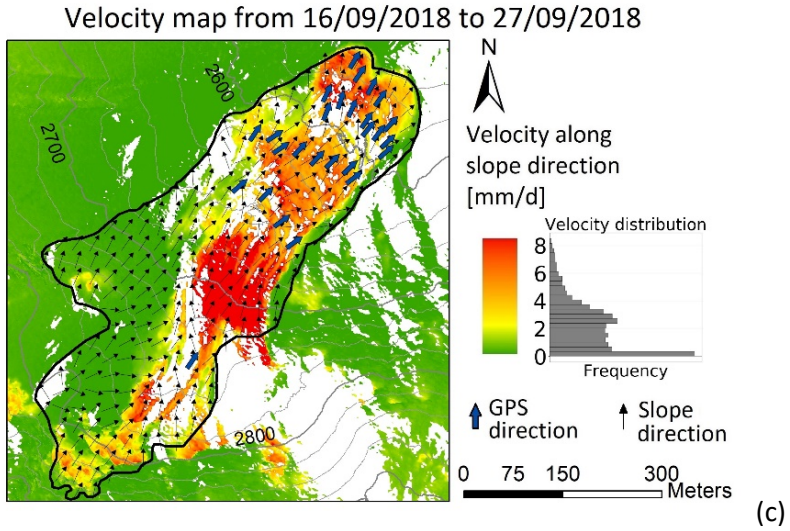

(c)

Figure 3.20: velocity maps obtained using the DIn-SAR technique in July2017 (a), August 2017 (b) and September 2018 (c). The velocities obtained along the LOS are reprojected along the maximum slope. Black arrows represent the slope direction, blue arrows represent the GPS direction.

The rock glacier velocities obtained using the amplitude tracking technique over longer time periods are shown in the high-resolution velocity maps (Fig. 3.21), obtained from the combination of LOS and AZ components. Similarly to the DIn-SAR results, the fastest areas are located above the frontal slope and in the middle part of the rock glacier, while in the North-West area the velocity is lower. The vector directions are parallel to the longitudinal axis of the rock glacier. The displacement directions and the velocity are similar for the three investigated periods. The mean values of displacements on the stable areas range between 3.9 mm and 7.1 mm, and standard deviation range between 1.8 mm and 2.1 mm.

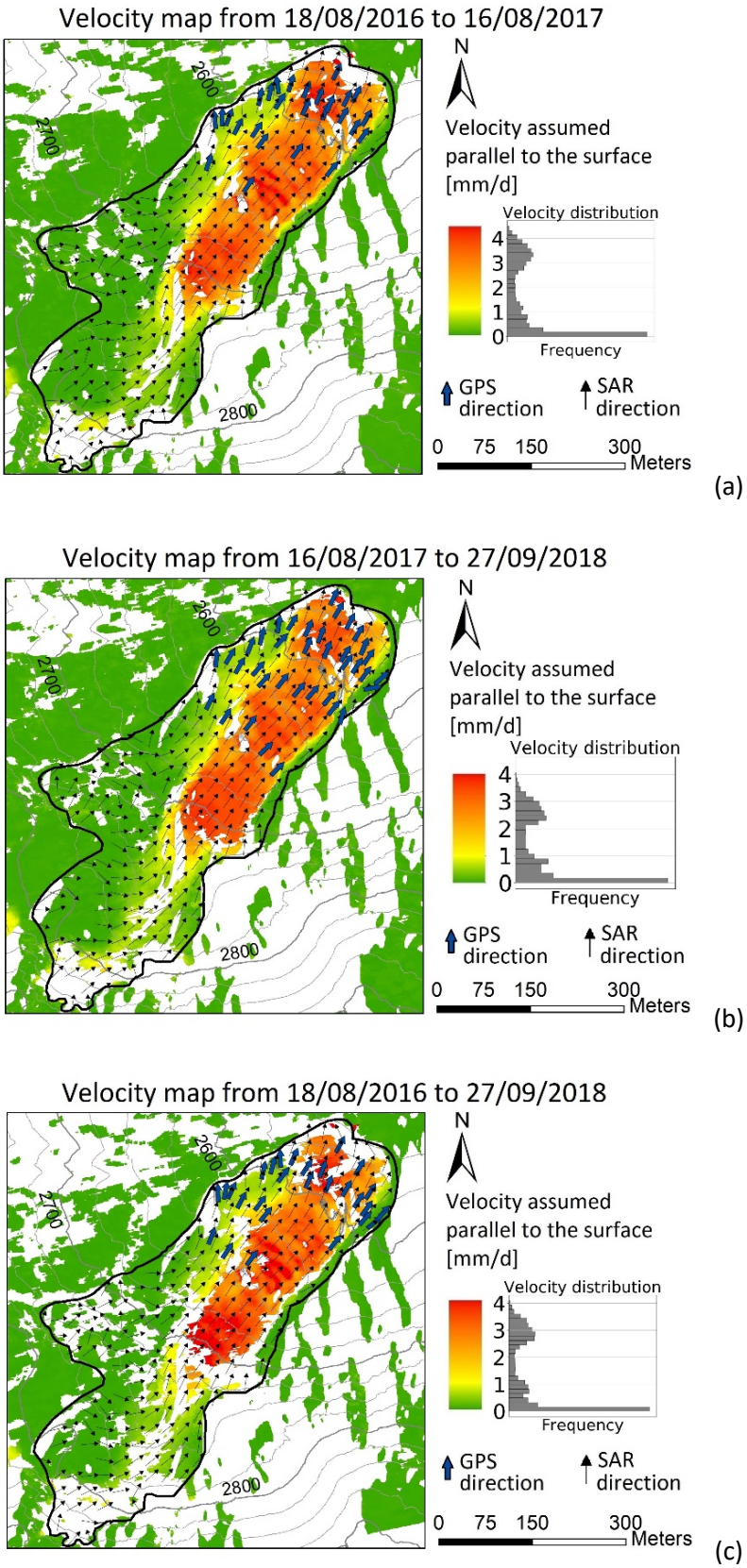

Figure 3.21: velocity maps obtained using the amplitude tracking technique between August 2016 and August 2017 (a), between August 2017 and September 2018 (b), and between August 2016 and September 2018 (c). The velocity vectors are obtained by the combination of LOS and AZ component. Black arrows represent the rock glacier displacement direction, blue arrows represent the GPS direction.

3.3.2.2 Sentinel-1 results

The velocity maps in figure 3.22 show the results obtained by the PS processing of Sentinel-1 data. The results from the relative orbits 117 and 168 of the summer 2017 show lower velocities inside the rock glacier compared to TSX results, whereas the pattern looks similar in the rest of the rock glacier. The fastest areas are located above the frontal slope and in the middle part of the rock glacier, while in the North-West area the velocity is lower. However, these results are unreliable because of widespread persistent scatters with negative values (i.e. up slope displacements) inside the rock glacier area. This is probably due to the very high displacement of the rock glacier combined with the complex surface roughness that can generate particular backscatter effects such as localized layover and shadow conditions. Lower velocities are obtained with the relative orbit 168 compared to the results obtained from the relative orbit 117. This is probably related to the unfavourable orientation of the LOS compared to the rock glacier orientation.

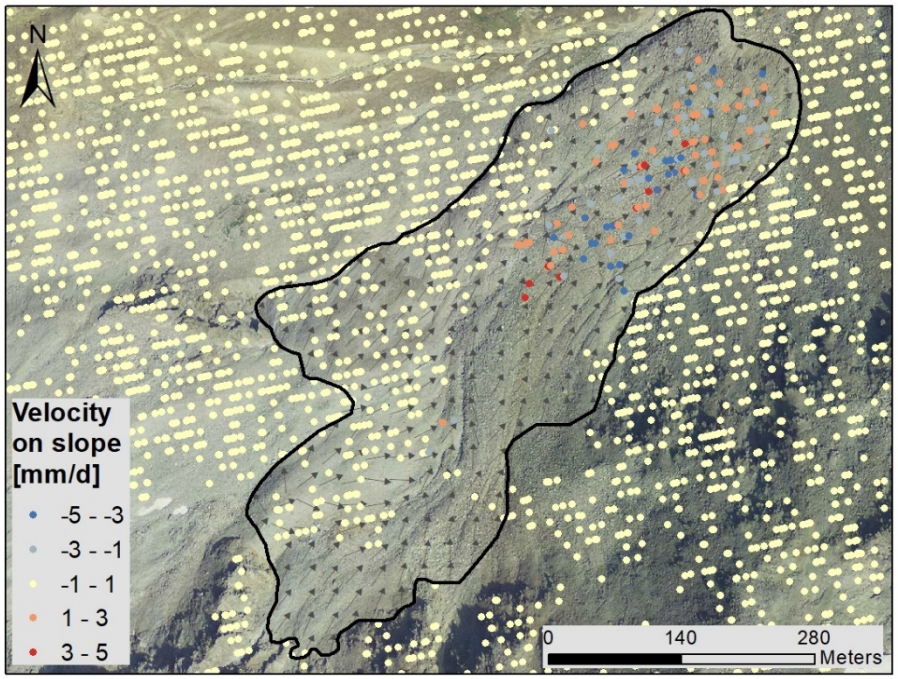

(a)

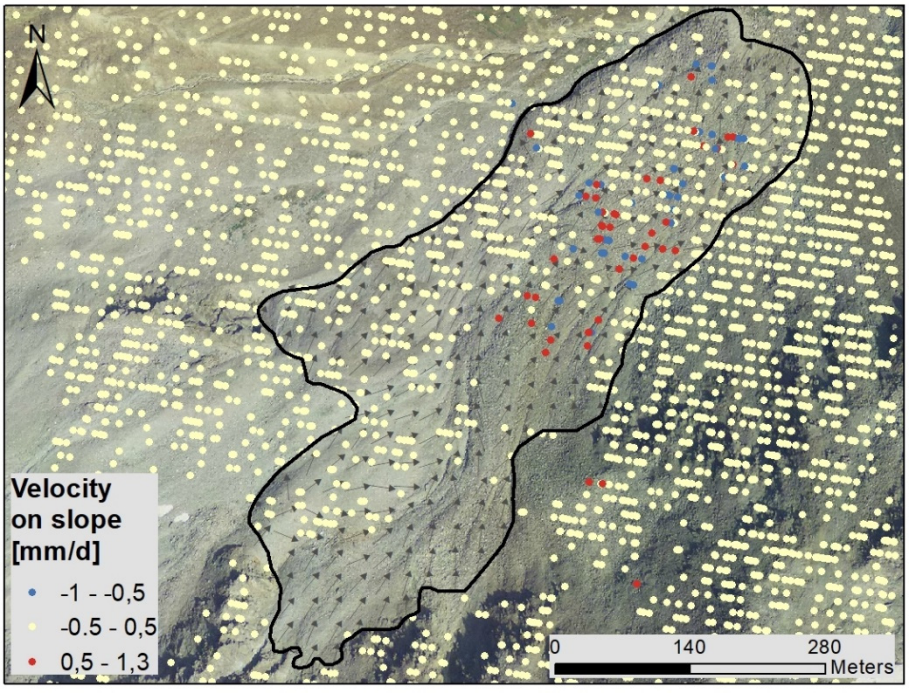

(b)

Figure 3.22: velocity maps obtained using the PS technique with Sentinel-1 data from the relative orbit 117(a) and 168 (b) during the summer 2017. The velocities obtained for each persistent scatter along the LOS are reprojected along the maximum slope. Grey arrows represent the slope direction.

The velocity maps in figure 3.23 show the results obtained by the SBAS processing of Sentinel-1 data. The results from the relative orbits 15 and 117 show lower velocities above the frontal slope compared to TSX results, whereas the pattern looks similar in the rest of the rock glacier. Completely different results were obtained from the relative orbit 168, where positive values are recorded above the frontal slope, while negative values (i.e. up slope displacements) are recorded in the middle-upper part of the rock glacier. This

velocity distribution is probably related to the unfavourable orientation of the LOS compared to the rock glacier orientation. The velocities obtained from the relative orbit 117 during the summer 2017 are similar to those obtained during the summer 2018. The mean values of displacements over stable areas outside the rock glacier range between 2.5 mm and 3.5 mm, and standard deviation range between 0.35 mm and 1.28 mm.

Velocity map from 17/06/2017 to 02/11/2017
with Sentinel 1 data, track 117

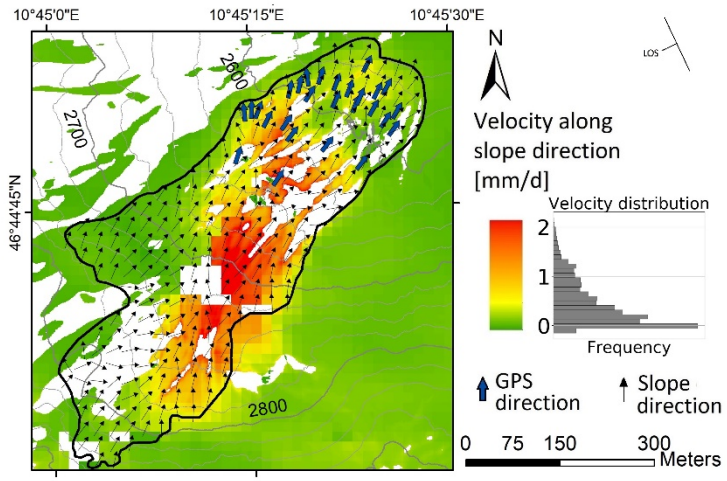

(a)

Velocity map from 15/06/2017 to 31/10/2017
with Sentinel 1 data, track 168

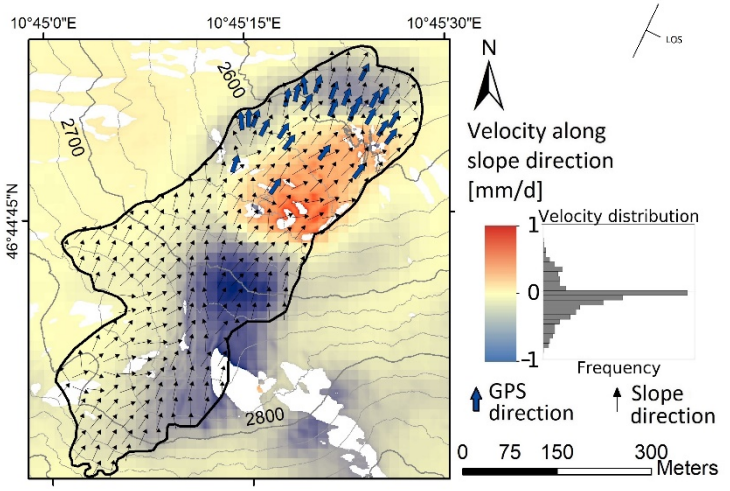

(b)

Velocity map from 23/06/2018 to 21/10/2018
with Sentinel 1 data, track 15

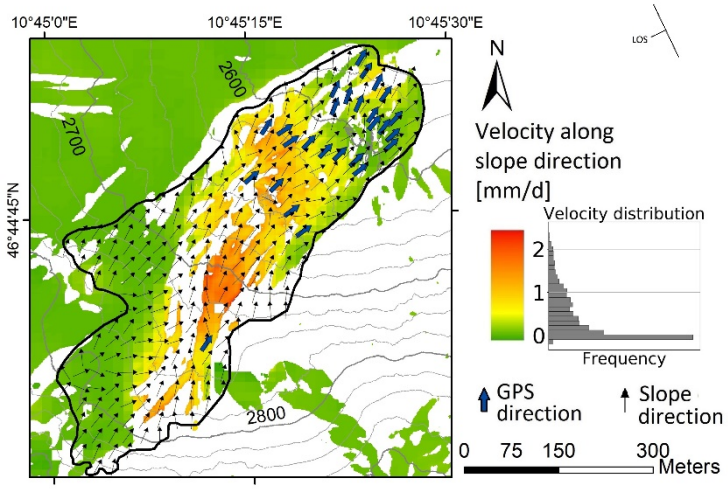

(c)

Velocity map from 24/06/2018 to 22/10/2018
with Sentinel 1 data, track 117

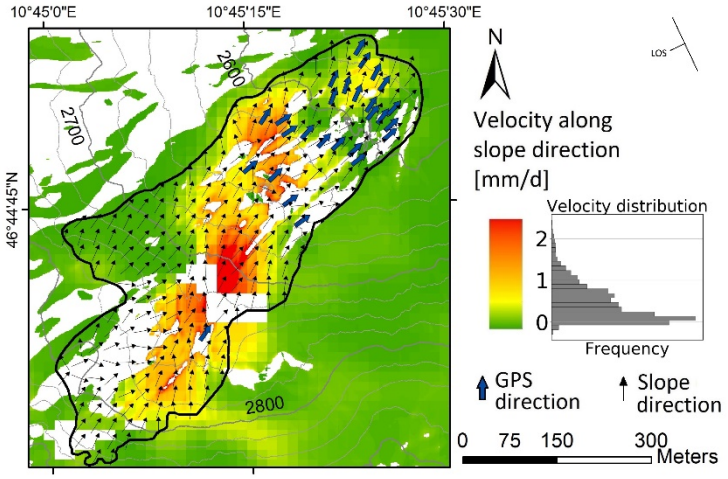

(d)

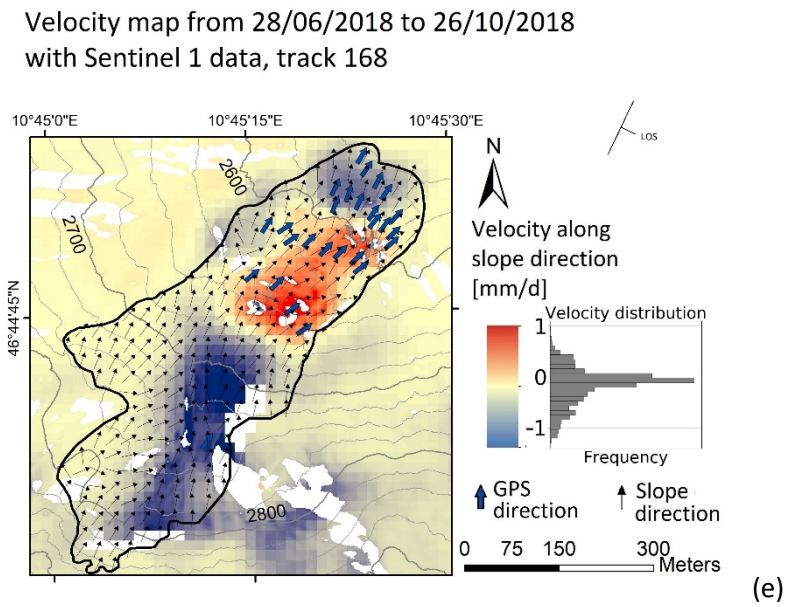

Figure 3.23: velocity maps obtained using the SBAS technique with Sentinel-1 data from the relative orbit 117(a) and 168 (b) during the summer 2017, and from the relative orbit 15 (c), 117 (d) and 168 (e) during the summer 2018. The velocities obtained along the LOS are reprojected along the maximum slope. Black arrows represent the slope direction, blue arrows represent the GPS direction.

3.3.2.3 Time series analysis

Figure 3.24 compares the velocities obtained by different techniques in correspondence of a selected number of GPS survey markers, separating the fast (central part) from the slow (North-West part) rock glacier zone. In detail, we plotted the mean velocity of the selected GPS survey markers obtained by (i) GPS, (ii) TSX data, and (iii) Sentinel-1 data (Fig. 3.24a). Reprojected displacement for the SAR techniques were used. PS results were not plotted because unreliable. Daily air temperature precipitations and GST are also showed.

During the summer 2017 (Fig. 3.24) the DIn-SAR technique provides an increase of velocity from 2.07 mm/d in July to 2.55 mm/d in August for the fast zone, while for the slow zone an increase of velocity from 0.4 mm/d in July to 0.82 mm/d in August. This velocity increase during the summer 2017 is confirmed by the GPS measurements, and also from UAV and GB-SAR. Velocities obtained with Sentinel-1 data are widely underestimated, compared to the other results. The ascending relative orbits 15 and 117 indicate a slight velocity increase during the summer 2018 for the fast zone, while for the slow zone only the ascending relative orbit 15 indicates a slight velocity increase in the same period. Other velocity variations are not detected with Sentinel-1.

On an annual timescale, the velocities measured by the amplitude tracking match rather well with GPS measurements, and also with the UAV. Between September 2016 and June 2017 velocities in the fast zone were 3.36 mm/d and 3.44 mm/d for amplitude tracking and GPS, respectively, while for the fast zone they were1.16 mm/d and 1.2 mm/d, respectively. Lower velocities were obtained between October 2017 and

June 2018. In detail, 2.55 mm/d and 2.75 mm/d were measured by the amplitude tracking and GPS, respectively, for the fast zone, while 0.7 mm/d and 0.95 mm/d were measured for the slow zone. Overall, the decrease in velocity between 2017 and 2018 is well captured by amplitude tracking, in particular over the fast zone (i.e. where the change in velocity was larger).

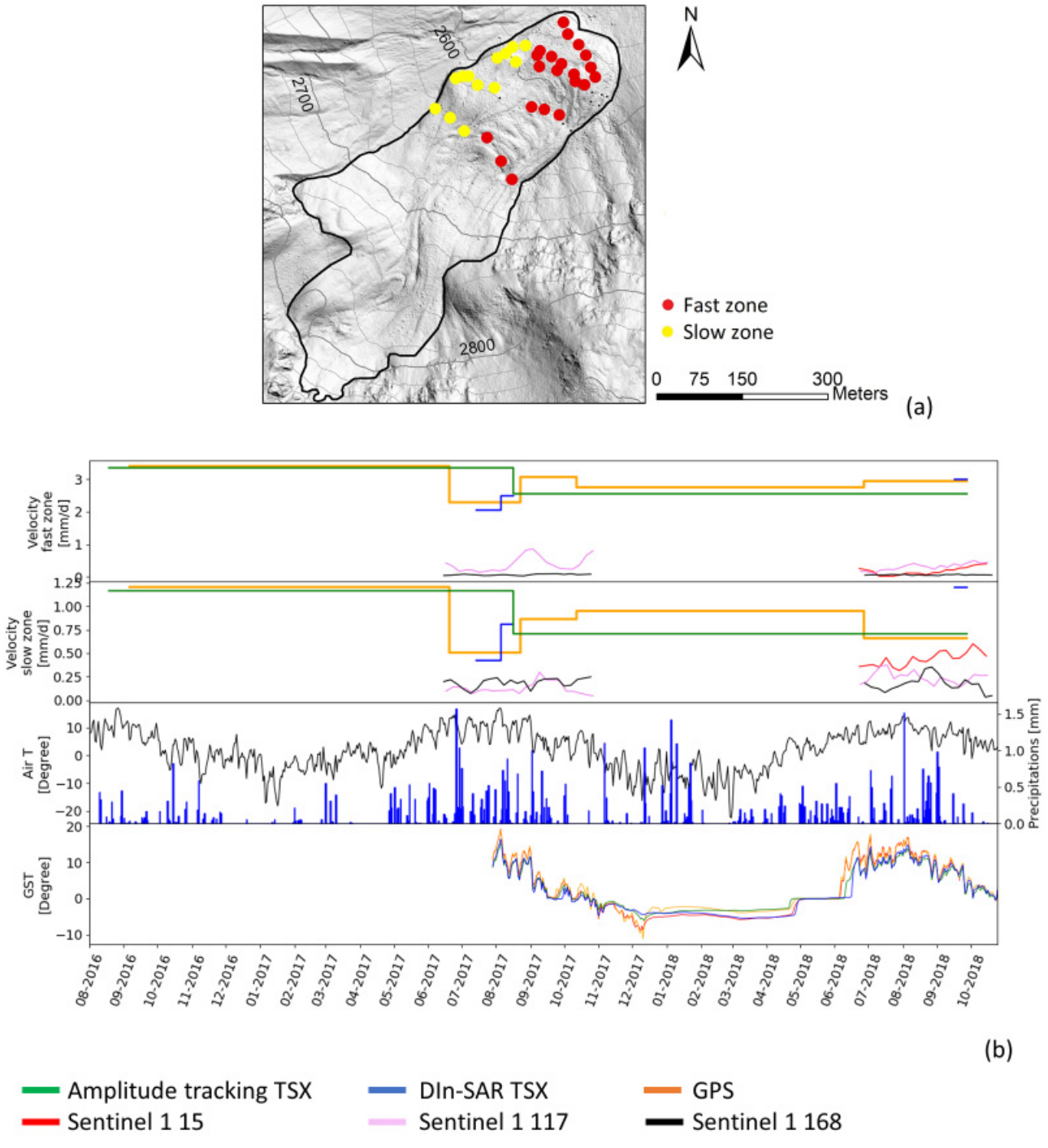

Figure 3.24: (a) position of the GPS survey marks used to investigate the velocities obtained by the different techniques employed. The velocities obtained in the fast rock glacier zone (central part) and in the slow rock glacier zone (North-West part) are showed in the graph (b). The velocities were computed using the total 3D displacement for the GPS technique, and the reprojected displacement for the SAR techniques. Climatic variables are also showed.

3.3.2.4 Data comparison

The reliability of the SAR products was assessed by comparison with GPS measurements. Since the SAR techniques provide the displacement information along the LOS and AZ components, we reprojected the GPS measurements along the LOS for the SBAS and DIn-SAR techniques, and along the LOS and AZ for the amplitude tracking technique. The reprojection was conducted following the same approach explained in the equations 3.3 and 3.4.

The comparison between the TSX DIn-SAR and the GPS was conducted although the different acquisition time of the TSX DIn-SAR data and the GPS measurements. RMSD and ρ are 0.43 mm/day and 0.8 (July 2017), 0.68 mm/day and 0.77 (August 2017) and 0.28 mm/day and 0.87 (September 2018), respectively (Tab. 3.5). These different values can be justified because each technique provides velocities information for different time intervals. In fact, the scatterplots obtained with the TSX DIn-SAR results of summer 2017 showed an offset compared to the GPS results (Fig. 3.25). In detail, the TSX velocities are overestimated because the TSX velocities recorded during the investigated times are higher than the velocities recorded by GPS between June and August 2017.

Good results were obtained with the amplitude tracking technique (Fig. 3.26), with RMSD and ρ between 0.39 and 0.16 mm/day and between 0.78 and 0.89, respectively, along the LOS direction. Better RMSD and ρ were obtained along the AZ direction, between 0.19 and 0.14 mm/day (RMSD) and between 0.91 and 0.96 (ρ) (Tab. 3.5) because of the higher spatial resolution in azimuth (16cm) compared to the spatial resolution in range (90cm).

Sentinel-1 results showed much lower agreement with GPS results them (Fig. 3.27). RMSD values between 1.07 and 0.27 mm/day are measured (Tab. 3.5). These RMSD values are similar to the RMSD values obtained between TSX and GPS because the absolute errors of Sentinel-1 are similar to those of TSX; however, the velocities measured by Sentinel-1 are lower than those measured by TSX, then Sentinel-1 is more affected by errors compared to TSX results. In fact, Sentinel-1 ρ values range between 0.56 and 0.37, lower than those obtained with TSX (Tab. 3.5).

The scatterplots with the Sentinel-1 results obtained from the ascending relative orbits (i.e. 15 and 117) showed a cluster of points with high absolute velocities recorded by GPS and low absolute velocities recorded by Sentinel-1 (Fig. 3.27). These points are located close to the frontal slope. In this area the velocities recorded by Sentinel-1 are lower, compared to the TSX results in which the measured velocities are higher. Sentinel-1 measurements are then largely underestimated, especially close to the frontal slope.

Table 3.5: table of RMSE computed between the SAR approaches and the GPS measurements.

Platform	Date	RMSD [mm/day]	ρ
DIn-SAR TSX	14/07/2017 - 05/08/2017	0.43	0.8
	05/08/2017 - 16/08/2017	0.68	0.77
	16/09/2018 - 27/09/2018	0.28	0.87
Amplitude tracking TSX	18/08/2016 - 16/08/2017	0.39 (LOS) 0.19 (AZ)	0.84 (LOS) 0.94 (AZ)
	16/08/2017 - 27/09/2018	0.22 (LOS) 0.18 (AZ)	0.78 (LOS) 0.91 (AZ)
	18/08/2016 - 27/09/2018	0.16 (LOS) 0.14 (AZ)	0.89 (LOS) 0.96 (AZ)
Sentinel-1	Track 117 17/06/2017 - 02/11/2017	0.76	0.47
	Track 168 15/06/2017 - 31/10/2017	0.27	0.37
	Track 15 23/06/2018 - 21/10/2018	1.07	0.56
	Track 117 24/06/2018 - 22/10/2018	1.07	0.37
	Track 168 28/06/2018 - 26/10/2018	0.28	0.44

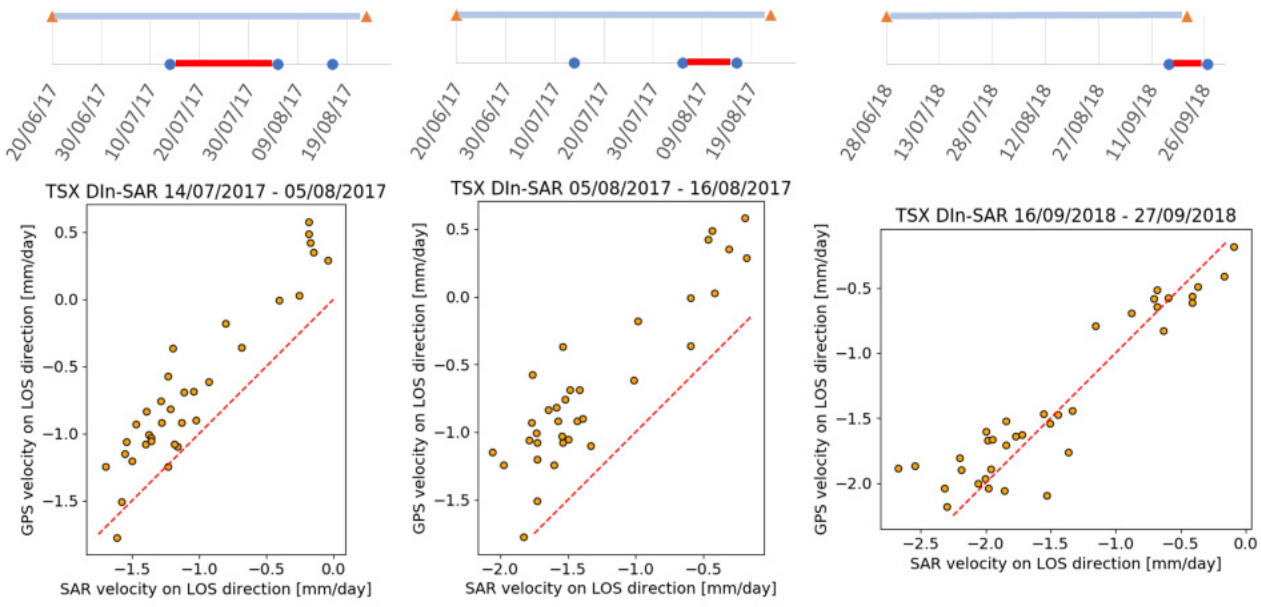

Figure 3.25: scatterplots of the periods investigated with the DIn-SAR using TSX images. On the x axis the velocity measured along the LOS, on the y axis the velocity measured by GPS and reprojected along the LOS. The red dashed line is the one to one line. On the top the time intervals investigated by DIn-SAR (red line) and the respectively GPS time intervals (orange triangle) used to validate the SAR approach.

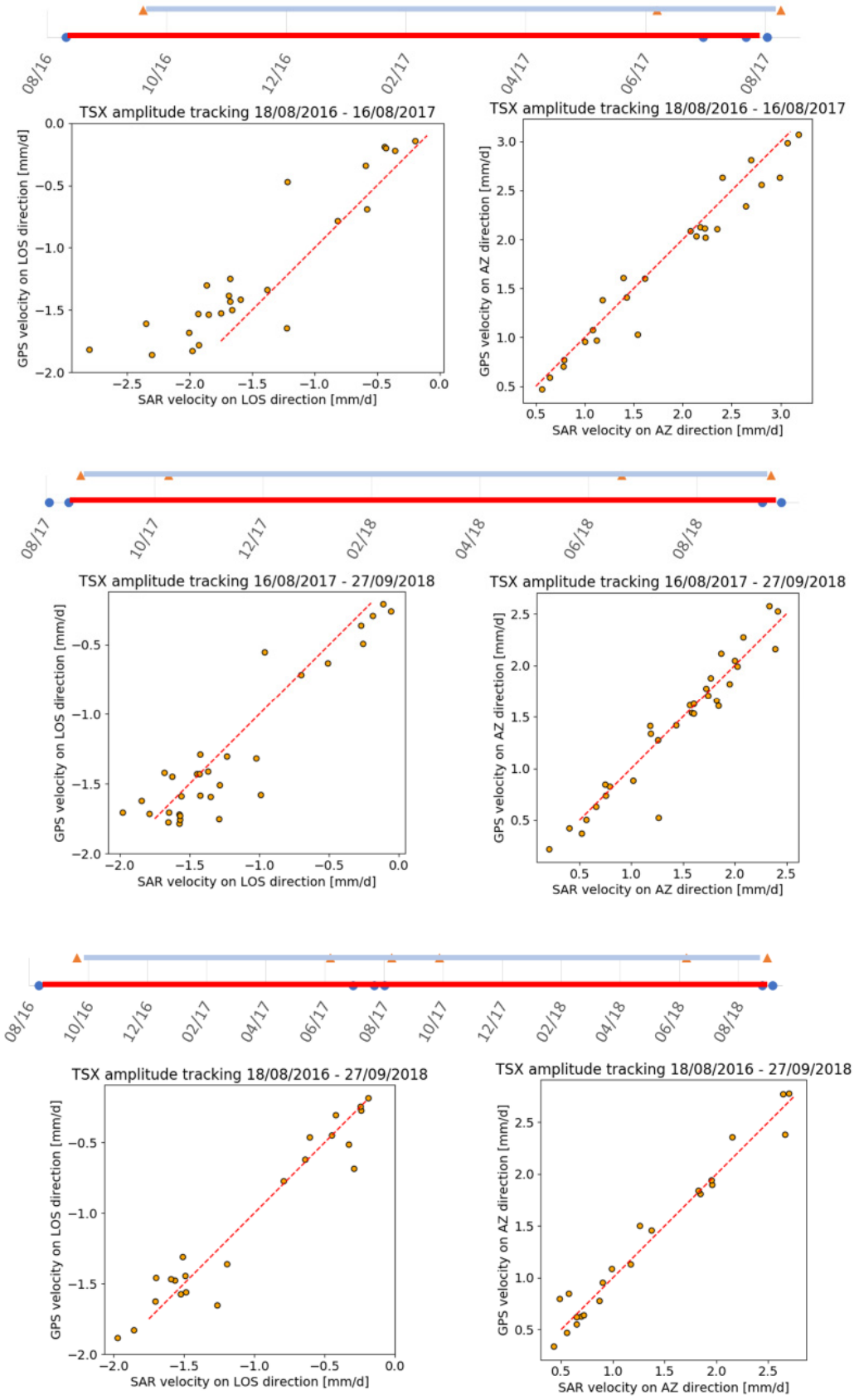

Figure 3.26: scatterplots of the periods investigated with the amplitude tracking using TSX images. On the x axis the velocity measured along the LOS (on the left) and along the AZ (on the right), on the y axis the velocity measured by GPS and reprojected along the LOS and along the AZ. The red dashed line is the one to one line. On the top the time intervals investigated amplitude tracking (red line) and the respectively GPS time intervals (orange triangle) used to validate the SAR approach.

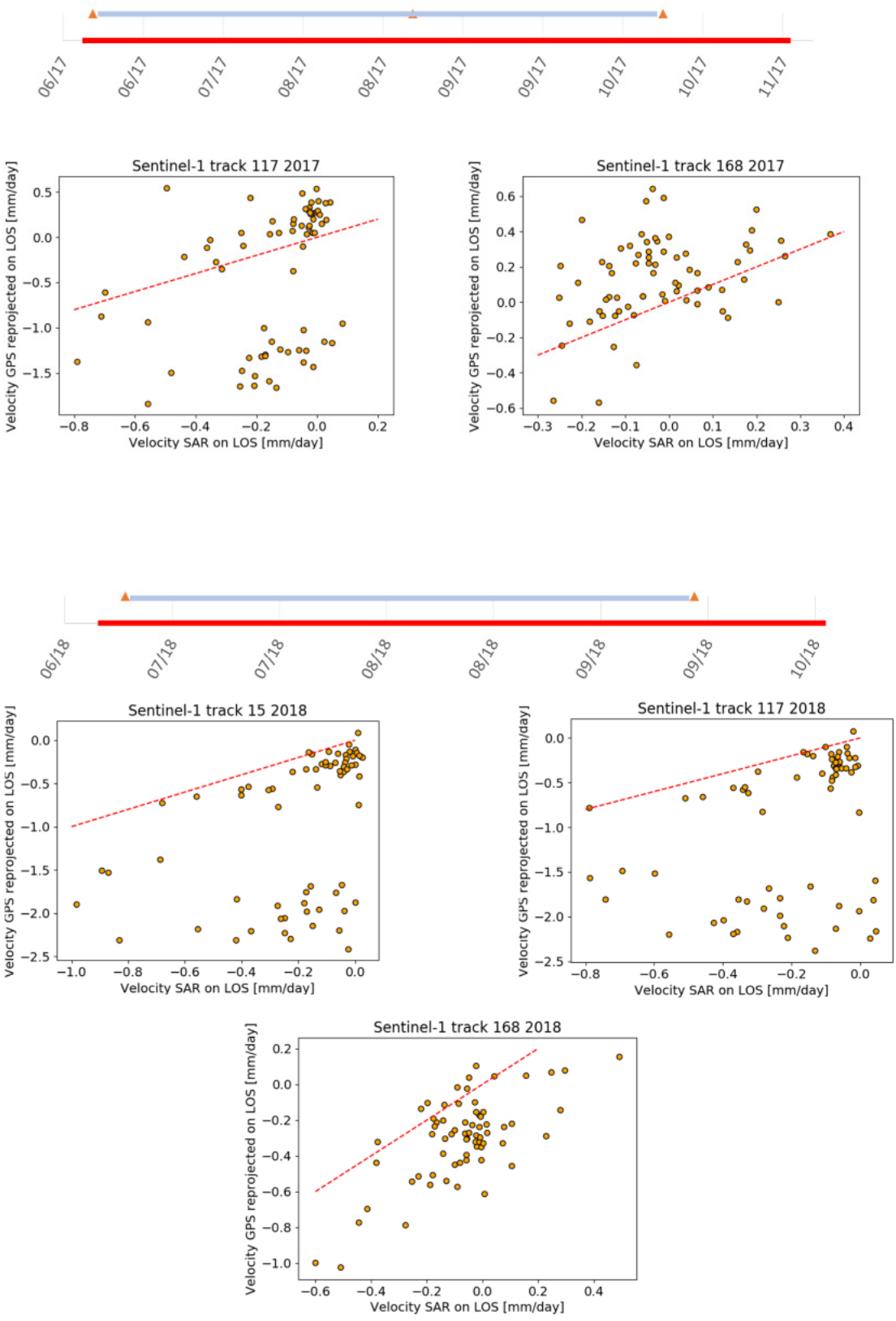

Figure 3.27: scatterplots of the periods investigated with Sentinel-1. On the x axis the velocity measured along the LOS, on the y axis the velocity measured by GPS and reprojected along the LOS. The red dashed line is the one to one line. On the top the time intervals investigated by Sentinel-1 (red line) and the respectively GPS time intervals (orange triangle) used to validate the SAR approach.

3.4 Discussion

3.4.1 Kinematic behaviour of Lazaun rock glacier exploiting in-situ and proximal sensing techniques

According to the geomorphological evidences (i.e. the well-developed surface structures due to the deformation such as ridges and furrows), the Lazaun rock glacier is characterized by a faster area located along the longitudinal axis, where maximum velocities around 4 mm/day are recorded by UAV and GB-SAR, in particular in the central part and close to the frontal slope. In contrast, velocities lower than 1 mm/day were recorded in the North-West area, which can be regarded as the slowest area of the landform. The DoD showed a prevailing lowering of the landform, with uplifts limited to small areas due to the planimetric displacement in correspondence of steep slopes, for example above the frontal slope. The landform lost 5100 m^3 during the observation period. In literature, the surface lowering was associated to ice melt or extending flow (Bosson and Lambiel, 2016; Lambiel and Delaloye, 2004). On the Lazaun rock glacier, the surface topography characterized by prominent transverse ridges and furrows and the surface velocity pattern suggest a prevailing compressive stress; therefore, the observed prevalence of surface lowering can be mainly related to ice melt rather than extending flow, with the exclusion of the rooting zone. This is supported by the study of Krainer et al. (2015), in which an ice melt volume of around 10000 m^3 per year was detected.

Two main processes of rock glaciers deformation are known from the literature, i.e. shearing within a distinct layer and internal plastic deformation due to the viscosity of the permafrost ice (Arenson et al., 2002; Buchli et al., 2013; Delaloye et al., 2012, 2010; Hausmann et al., 2007; Ikeda et al., 2008; Roer et al., 2008). The internal structure of Lazaun rock glacier is well known thanks to two boreholes drilled in the lower part (Lazaun 1) and near the front (Lazaun 2) and described in Krainer et al. (2015). According to this study, the frozen core is composed of a mixture of debris and ice, with a variable percent ice content along the vertical profile (undersaturated–oversaturated), and a low amount of fine-grained sediments. One of the cores (Lazaun 1) shows that the rock glacier is composed by two approximately 10-m-thick frozen bodies, separated by an unfrozen layer around 2.1 m thick (Fig. 3.1d). Near the front (core Lazaun 2), the ice content is significantly lower compared to the upper part. The inclinometer measurements conducted in the two boreholes (Krainer et al., 2015) demonstrated the presence of a shear horizon at a depth between 20 and 24 m, where banded ice containing high amounts of fine-grained sediment occurs. A second shear horizon was detected at a depth of about 14 m, near the base of the upper frozen part of the rock glacier. According to the authors, most of the deformation rate occurs at these shear horizons and the internal deformation is of minor importance. This may explain the high surface flow velocities recorded by GPS, which are similar to the deformation rates measured at the shear horizons. Finally, the authors state that the rates of deformation are probably favoured by the temperature of the ice which is close to the melting point. Our study showed an asymmetric transversal velocity profile (Fig. 3.19c), with lower velocities in the North-West part and higher velocities in the South-East part. This transversal profile has a “plateau” shape, with rather

constant planimetric velocities inside the rock glacier. Bosson and Lambiel (2016) attributed a similar shape of the velocity profile to a process of shear deformation within a distinct layer. Therefore, our findings are in agreement with the presence of shear layers inside the rock glacier where the displacement is concentrated, as detected by Krainer et al. (2015).

GPS measurements and ICC from UAV data allow to study the interannual velocity of Lazaun rock glacier between summer 2016 and summer 2018. In detail, a velocity decrease from about 3 mm/d to about 2.7 mm/d was detected between the period 2016-2017 and 2017-2018, therefore suggesting a slight deceleration. Similar trends were observed also on other rock glacier, with a slowing down in velocity after 2016 because of the absence of snow in early winter ("PERMOS reports," n.d.). This would be in contrast with other studies conducted in the European Alps, which suggest a general trend of increasing velocities (Buchli et al., 2018, 2013; Delaloye et al., 2010; Ikeda et al., 2008; Kenner et al., 2019, 2017; Roer et al., 2005; Seppi et al., 2019). However, it is not possible to make any considerations, given the very short period covered by our observations and the strong interannual variability of rock glacier velocity (Kellerer-Pirklbauer et al., 2018).

Seasonal velocity variations were detected during summer 2017 and 2018 (Fig. 3.16). In the fast rock glacier zone, during summer 2017 a velocity increase from 2.3 – 2.5 mm/d to 3 – 3.1 mm/d was detected by GPS and ICC from UAV between the first investigated period (from 20/06/17 to 23/08/17) and the second one (from 23/08/17 to 12/10/17). In the slow zone, GPS measured an increase of velocity, while UAV measured a decrease. These different behaviours are probably related to the small displacements during a short time period, close to the sensitivity of the ICC technique. Indeed, during these relatively short investigated periods (approximately two months) the detected ρ values (i.e. the measure of correlation) are lower than those obtained during long investigated periods (i.e. interannual) between the autumn and the following spring. A similar acceleration from 2.15 mm/d to 2.9 mm/d was detected between the GB-SAR campaign carried out from 09/08/18 to 18/08/18, and the second one from 13/09/18 to 03/10/18. Because of logistical issues and the presence of snow cover, GPS, UAV and GB-SAR data can be acquired only during summer and autumn, thus preventing to measure velocity variations over the entire year. It is therefore impossible to detect when the rock glacier reached the minimum and maximum velocities. However, from the experimental data, it is possible to state that the maximum velocity is reached between late summer and autumn (Fig. 3.16).

Investigations of seasonal velocity variations by means of intensive field campaigns or continuous GPS monitoring systems (Buchli et al., 2018, 2013; Delaloye et al., 2010; Ikeda et al., 2008; Kenner et al., 2019, 2017; Wirz et al., 2016) suggested a velocity increase during summer and a deceleration during winter. Kenner et al. (2017 and 2019) and Delaloye et al. (2010) recorded the minimum rock glacier velocities in spring, before the beginning of snow melt, while the maximum velocities were recorded in autumn before the onset of the snow. On the Lazaun rock glacier, the velocity increase towards late summer/early autumn

is well visible (Fig. 3.16) and this seems to support the observations made on other rock glaciers (Kenner et al., 2019, 2017; Wirz et al., 2016). Lower mean velocities were obtained in the first part of summer while higher mean velocities were observed between autumn and spring (Fig. 3.16)

The GB-SAR instrument provided displacement measurements of Lazaun rock glacier with a very high temporal resolution (i.e. hours) and distributed over the whole landform. A "step-like" cumulative displacement was observed, in which the displacement is concentrated in short periods of a few hours, separated by periods with much smaller displacement (Fig. 3.10). As far as we know, this particular kinematic behaviour was observed for the first time on a rock glacier, thanks to the use of the GB-SAR instrument, which allows to obtain displacement measurements every hour, with sensitivity of a fraction of millimetre. As reported by Wirz et al. (2016), several studies were conducted to analyse velocity variations during short time intervals (e.g. daily), but the technologies used in these studies do not allow having a temporal resolution able to see velocity variations in very short time intervals (e.g. hourly). GB-SAR and real aperture radar instruments were already used to measure glaciers and rock glaciers displacement (Buchli et al., 2018; Dematteis et al., 2018, 2017; LIU et al., 2019; LÓPEZ-MORENO et al., 2019), however, a kinematic behaviour similar to the Lazaun rock glacier was observed only on a glacier in China (LIU et al., 2019).

3.4.2 Factors influencing the rock glacier kinematic

Ikeda et al. (2008) suggested that the downslope strain rate of rock glacier is related to the shear stress and to the characteristics of the shear layer (ice/debris content, water availability). To explain the particular "step-like" displacement that occurs on Lazaun rock glacier, our hypothesis is that the shear stress would accumulate along the shear layer(s), and strain rate would occur in particular time intervals when the accumulated shear stress exceeds a maximum threshold, producing a surface displacement that is detected by our instrument. The shear stress is then accumulated and released every day when the maximum shear resistance is exceeded. However, this hypothesis is supported only by the observed surface displacements and, to confirm it, a detailed rheological analysis at the shear zones of the rock glaciers would be required. As additional explanations suggested by recent works, the rock glacier kinematics on short, seasonal and interannual timescales is controlled by the water content along the shear layer(s) (Bosson and Lambiel, 2016; Buchli et al., 2018, 2013; Cicoira et al., 2019; Harbor et al., 1997; Ikeda et al., 2008; Kääb et al., 2007; Kenner et al., 2019, 2017; Wirz et al., 2016). Water infiltration through drainage systems within the rock glacier may lead to an increase in pore water pressure and hence a reduction in shear resistance (Harbor et al., 1997; Terzaghi, 1943), thus triggering increased velocities. In addition, the water infiltration generates a rapid warming of the ground at depth through thermal advection and release of latent heat (Rist and Phillips, 2005), leading to a higher unfrozen water content (Anderson et al., 1973; Arenson et al., 2002) and increasing the strain rates of the ice in the frozen matrix (Yamamoto, 2015).

Two sources influence the water supply: snowmelt and heavy precipitation. Snowmelt mainly influences the seasonal velocity variations. The seasonal increase in velocity from spring/early summer is associated with the beginning of snowmelt and the percolation of snowmelt water along the shear layer(s) which reduce the shear resistance (Buchli et al., 2013; Ikeda et al., 2008). The seasonal decrease in velocity from the end of summer/autumn is associated with the beginning of snow cover which strongly reduces the water infiltration and insulates the ground. Ground temperature is only influenced by permafrost, without any influence of the atmosphere. Therefore, permafrost generates a cooling of the ground, re-freezes the pore water and increases the shear resistance (Buchli et al., 2013; Ikeda et al., 2008). Therefore, the velocity increase detected on Lazaun rock glacier in late spring/summer (Fig. 3.16) could be related to the infiltration of snowmelt water in the catchment area and on the rock glacier. Long periods of snowmelt and therefore of meltwater availability are suggested by the considerable length of the zero curtain (about 1.5 months) showed by GST measurements in spring 2018 (Fig. 3.16) The infiltration of meltwater as hypothesis for explaining the seasonal velocity increase on the Lazaun rock glacier was already proposed by Krainer et al. (2015).

Another water supply that may influence the velocity variations of rock glaciers is precipitation. Wirz et al. (2016) suggested that strong precipitation events triggered short term velocity peaks of their investigated rock glacier. The short time lag (i.e. couple of days) observed between the precipitation and the onset of the velocity peak indicates that the percolated water reached the shear layer(s) in a short time (Wirz et al., 2016). A similar behaviour was not observed on the Lazaun rock glacier during the two 2018 GB-SAR campaigns (Fig. 3.10b and 3.10c), and velocity peaks were not detected at hourly scale during or after precipitation events. Velocity peaks related to precipitation events were not observed also in other rock glaciers, and a possible explanation could be the existence of complex drainage systems within the rock glacier, which can generate a variable kinematic response depending on the precipitation events (Kenner et al., 2017; Wirz et al., 2016). However, it must be taken into account that rainfall is recorded at 4 km from the Lazaun, so not all events occurring near the meteorological station also occur in the area of the rock glacier (and viceversa). The spring water temperature recorded during the two 2018 GB-SAR campaigns showed values comprised between 1.3 °C and 1.4 °C, with no diurnal variations (Fig. 3.10b and 3.10c). A sudden decrease of the water temperature (about a tenth of a degree) was observed during the main rainfall events, followed by a slower increase of the same magnitude. The air temperature during the rainfall events has always been some degrees above zero (between 5°C and 10°C). Therefore, although the rainfall input was comparatively “warm”, the spring returned comparatively “cold” water. This seems to confirm the existence of a well-structured drainage system in the Lazaun rock glacier, in which complex processes of heat exchange between rainwater and ice may occur.

An additional correlation was observed in September, when two minimum air temperatures and GST (one in 25 September, one in 2 October, Fig. 3.10b) were associated with a velocity decrease from 4 – 6 mm to 2 – 3 mm in 3 hours. This seems to support the hypothesis that a decrease in GST generates an increase in the shear resistance, reducing the surface deformation (Buchli et al., 2013; Ikeda et al., 2008).

3.4.3 Satellite SAR-based techniques

The spatial distribution of surface velocities determined using TSX on the Lazaun rock glacier is in good agreement with GPS results, which is the reference validation dataset used in this case study.

The amplitude tracking technique applied to TSX data allowed to study the interannual variations in velocity of Lazaun rock glacier between summer 2016 and summer 2018. In detail, a velocity decrease from about 3.3 mm/d to about 2.8 mm/d was detected between the first and the second hydrological years, therefore suggesting a slight deceleration. This short-term trend, which is in contrast with the general trend of increasing velocities observed in the European Alps (Buchli et al., 2018, 2013; Delaloye et al., 2010; Ikeda et al., 2008; Kenner et al., 2019, 2017; Roer et al., 2005; Seppi et al., 2019) confirms the findings from the in-situ and proximal sensing techniques (i.e. GPS and UAV).

In a similar way, intra-seasonal variations of surface velocities were detected using DIn-SAR with TSX data during both summer 2017 and 2018 (Fig. 3.24). The velocity increase towards late summer/early autumn was also detected exploiting in-situ and proximal sensing techniques (i.e. GB-SAR, GPS and UAV). This seems to support the observations made on other rock glaciers, where a velocity increase during summer and a deceleration during winter were observed (Buchli et al., 2018, 2013; Delaloye et al., 2010; Ikeda et al., 2008; Kenner et al., 2019, 2017; Wirz et al., 2016).

Results obtained with Sentinel-1 PS technique are unreliable, probably because this technique is not able to investigate the very high displacement of the rock glacier, especially in areas with complex surface roughness that can generate particular backscatter effects such as localized layover and shadow conditions. Velocities detected from SBAS Sentinel-1 are largely underestimated compared to the GPS results (Fig. 3.27). In fact the lowest ρ values are obtained exploiting this satellite. A slight increase in velocity was detected by the ascending geometries 15 and 117 in the fast zone, while in the slow zone increase in velocities were not detected. Seasonal velocity variations were not detected during summer 2017 and 2018 by the descending geometry (i.e. 168). The descending geometry is less reliable because of the non-favourable orientation of the LOS compared to the rock glacier orientation. This is also well visible on the velocity maps (Fig. 3.23b and 3.23e), where positive values are recorded above the frontal slope, and negative values (i.e. up slope displacements) are recorded in the middle-upper part of the rock glacier. This confirm the issues related to the SBAS technique already perceived in the chapter 2.

4.6 Conclusions

In this work, in-situ and proximal sensing techniques such as GB-SAR, UAV and GPS were used to study the kinematics of Lazaun rock glacier. The displacement was investigated with temporal resolutions from interannual to hourly. UAV and GPS allowed to analyse the interannual and seasonal velocity variations, while GB-SAR allowed to investigate, for the first time on a rock glacier, the displacement with hourly resolution. On an interannual basis, a slight velocity decrease (from about 3 mm/d to about 2.7 mm/d) was observed between 2016-2017 and 2017-2018. An increase in velocity was observed on a seasonal basis i.e. from early summer to late summer/early autumn 2017 and 2018. This was observed also in other rock glaciers of the Alps and support the possible role of water infiltration from snowmelt and/or rainfall as one of the main drivers of the velocity variations. The GB-SAR measurements showed for the first time on a rock glacier the flow velocity with an hourly temporal resolution. A “step-like” pattern of the cumulative movement was observed, which occurs only during particular short time periods of 1 – 3 hours. This pattern seems to be independent from the main environmental variables (air and ground temperature, snowfall and rainfall), suggesting a complex interplay between the external drivers and the dynamic response of the rock glacier, which is modulated by the observed existence of distinct shear layers in the debris body. However, a slight correlation between temperature and intensity of displacement was observed.

From qualitative analysis only slight correlations were observed between environmental variables and kinematic, probably because during the periods investigated there was not enough climatic variability. Further investigations are needed, with particular emphasis on mid- and long-term monitoring, to better clarify the kinematic behaviour of the rock glacier at different spatial and time scales in relation to the outer and inner controlling factors.

Satellite SAR approaches demonstrate their potentiality to monitor the kinematics of rock glaciers with different time scales. Results are in agreement with those obtained with in-situ and proximal sensing approaches. Satellite platforms are therefore useful to study areas where the access to acquired field data is not possible or complicated. TSX data are more suitable compared to the Sentinel 1, probably because of the very high spatial resolution. However, Sentinel-1 data are open data, then they are widely used. Refining SAR methods is an important task in prospective of improvement, especially with Sentinel-1 data.

Chapter 4

Conclusions

The ice contained in active rock glaciers could be a key freshwater resource for mountainous areas in the perspective of future climate change. The amount of ice contained in active rock glaciers should be estimated at site-specific scale, while the regional approach enables to extend this information over large areas. Therefore, this research suggests that studying the activity of rock glaciers at different levels (i.e. from regional to site-specific scale) and with the proper tools and methods is a key task to help quantifying this resource.

This thesis provides a contribution to the knowledge on rock glacier activity at different spatial and temporal scales, testing and comparing different remote sensing and in-situ observation techniques. From the research conducted in the study areas, it emerges that the rapidly changing activity of rock glaciers is a key theme that, in the framework of climate change, should be approached at diverse spatial scales and combining different techniques. The objectives of the thesis, which were in agreement with those of the ALPSMOTION project, have been satisfactorily achieved. In particular, effective methods for classifying rock glacier activity at the regional scale were developed, and the kinematics of a specific active rock glacier (Lazaun) were successfully investigated at different temporal scales and combining different techniques.

At regional scale, satellite remote sensing proved as an effective technique for investigating the activity of rock glaciers. Sentinel-1 SAR data were used to develop two unsupervised and replicable methods for defining the activity of rock glaciers, distinguishing moving and no-moving landforms. The first method is based on the SAR coherence, which has the main advantage to provide an objective detection of the rock glacier activity status, avoiding the subjectivity and the potential misinterpretations that characterize, for example, the visual interpretation of DIn-SAR products. The second method derives information on rock glacier activity from the displacement maps obtained by multitemporal interferometric techniques (i.e. PS and SBAS). The main limitation of this approach is the difficult processing of SAR data, especially in mountainous areas with complex topography and with short snow-free periods, that reduce the number of usable images. Over large areas, PS technique works better than the SBAS technique. This last one is unreliable probably because of some errors due to atmospheric phase components related with the topography and not removed during the processing. Furthermore, the unwrapping step of SBAS technique is a difficult task to carry out on large areas with complex topography and widespread vegetation.

These two powerful tools have been applied to the entire study area, enabling for the first time the detection of the rock glaciers activity on an objective basis, a key feature that is still lacking in existing inventories. The main advantage of these methods is the unsupervised way to classify the rock glacier activity over large areas, thus avoiding long and time-consuming analyses. Thanks to the wide availability of Sentinel-1 imagery, these techniques have a wide potential applicability, and can be employed for assessing ex-novo the rock glacier activity status, as well as for confirming/correcting existing activity status classifications based, for example, on geomorphological considerations.

At site-specific scale, the kinematics of the Lazaun rock glacier (Val Senales, South Tyrol) were successfully studied exploiting in-situ, proximal and remote sensing techniques. GPS, ICC with UAV data, SAR interferometry and amplitude tracking are well-established techniques used from the scientific community, whereas GB-SAR, which was previously used to study landslides, glaciers and anthropic infrastructures, was applied for the first time to investigate the kinematics of a rock glacier. The displacement of Lazaun rock glacier was investigated with temporal resolutions from interannual to hourly exploiting the combination of these techniques. On an interannual basis, a slight velocity decrease was observed between 2016-2017 and 2017-2018. Similar trends were observed also on other rock glacier, with a slowing down in velocity after 2016, while general trend of increasing velocities was observed in other studies conducted in the European Alps. An increase in velocity was observed on a seasonal basis i.e. from early summer to late summer/early autumn 2017 and 2018, as already observed in other study cases. For the first time, the hourly displacement trend of a rock glacier was investigated thanks to the very high temporal resolution of GB-SAR instrument. An hourly “step-like” pattern of the cumulative movement was observed, which occurs only during particular and short (few hours) time intervals. These unexpected and novel results could open up new perspectives in understanding the kinematic mechanisms of rock glaciers and deserve further investigations.

Results obtained with the satellite SAR approaches are in agreement with those obtained with in-situ and proximal sensing approaches. This demonstrate the potentiality of satellite SAR platforms to monitor the kinematics of rock glaciers with different time scales. Satellite platforms are therefore useful to study areas where field data cannot be acquired (e.g. remote areas). High spatial resolution data are more suitable to study relatively-small landforms as rock glaciers, but often these data are too expensive. A valid alternative are the open data Sentinel-1. On local scale SBAS technique works well compared to the PS technique. This last one is unreliable probably because this is not able to investigate the very high displacement of the rock glacier, especially in area with complex surface roughness that can generate particular backscatter effects such as localized layover and shadow conditions.

Depending on the extension of the investigated area, PS or SBAS technique is more suitable. In this work both were used to deepen the knowledge of each. In a prospective of future works, these techniques should be improved in order to overcome the weakness of each technique, for example the removal of atmospheric

components for the SBAS or the accuracy of displacement maps for the PS. Further works could be the application of other multitemporal interferometric techniques that exploit both the theoretical principles of SBAS and PS.

The work carried out showed that the combination of different techniques is essential to investigate the displacement with different temporal resolutions. Each technique has advantages but also limitations, then the combination of several techniques allows to reduce their limits. For example, ICC with UAV data allow to obtain a large spatial coverage, compared to the punctual displacement information of GPS. However, GPS allow to obtain the displacement along the three different dimensions (i.e. North-South, East-West and vertical). GB-SAR is able to provide the displacement information with a very high temporal resolution, but the transportation and installation is very difficult to carry out in mountain regions, because of the considerable weight and size of the instrument. Satellite SAR data allow to obtain displacement information along the particular satellite view (e.g. along LOS and AZ), without carrying out field activities. Interannual and sub-seasonal investigation can be carried out exploiting satellite approaches, and results are similar to those obtained with in-situ and proximal sensing approaches. However, the high redundancy of different techniques increases the robustness of results.

Weak or no interactions were observed between the kinematic behaviour of the Lazaun rock glacier and the main environmental variables (air and ground temperature, snowfall, rainfall, spring water temperature), at all the time scales. More investigations would be needed on this topic, and long-term monitoring observational data would be essential to better understand the potential role of the external drivers on the rock glacier flow patterns, in particular when investigating sub-daily and shorter term (i.e. hourly) variations.

Further works should involve the use of the GB-SAR instrument on other study cases and the acquisition of additional data regarding the internal structure and the rheology, in order to find out the hourly, step-like movement on other landforms and better understand the factors driving this particular displacement behaviour.

Acknowledgments

This work was conducted within the project ALPSMOTION (ALPine Slow slope Movement moniTorIng and detectiON with remote and proximal sensing), coordinated by Eurac Research-Institute for Earth Observation and funded by the Autonomous province of Bolzano “Ripartizione Diritto allo Studio, Università e Ricerca Scientifica”. The PhD of Aldo Bertone in Earth and Environmental Sciences at the University of Pavia was funded by the ALPSMOTION project. SAR data were processed with SARscape software (SARMAP). GPS data were provided by University of Innsbruck. TSX Data were provided by the European Space Agency, Project Proposal id 34722, © DLR, distribution Airbus DS Geo GmbH, all rights reserved.

I would like to express my special appreciation and thanks to my supervisors Roberto Seppi, Mattia Callegari and Francesco Zucca. I would like to thank you for the infinite patience and support, for the essential support during the field activities and for the helpful suggestions, corrections and amendments to the thesis and the published paper. Special thanks are also given to Luca Carturan and Christophe Lambiel, for their advices during the reviewing phase of the thesis.

I thank Eurac Research-Institute for Earth Observation for the support of my PhD and the contributions to the paper. I thank ALPSMOTION project for the financing of my PhD. I thank SARMAP S.A. and CTTC -- Centre Tecnològic de Telecomunicacions de Catalunya for the support and the internship.

I thank my parents, grandparents, friends and girlfriend for supporting me in everything I do.

References

Alcántara, I., Goudie, A., 2010. Geomorphological hazards and disaster prevention. Cambridge University Press.

Anderson, D.M., Tice, A.R., McKim, H.L., 1973. The unfrozen water and the apparent specific heat capacity of frozen soils, in: Second International Conference on Permafrost, Yakutsk, USSR. North American Contribution. pp. 289–295.

Antonello, G., Casagli, N., Farina, P., Leva, D., Nico, G., Sieber, A.J., Tarchi, D., 2004. Ground-based SAR interferometry for monitoring mass movements. Landslides 1, 21–28. https://doi.org/10.1007/s10346-003-0009-6

Arenson, L., Hoelzle, M., Springman, S., 2002. Borehole deformation measurements and internal structure of some rock glaciers in Switzerland. Permafr. Periglac. Process. 13, 117–135. https://doi.org/10.1002/ppp.414

Ayoub, F., Leprince, S., Keene, L., 2009. User's Guide to COSI-CORR Co-registration of Optically Sensed Images and Correlation. Book 1–38.

Balzter, H., 2001. Forest mapping and monitoring with interferometric synthetic aperture radar (InSAR). Prog. Phys. Geogr. Earth Environ. 25, 159–177. https://doi.org/10.1177/030913330102500201

Bamler, R., Hartl, P., 1998. Synthetic aperture radar interferometry. Inverse Probl. 14, R1–R54. https://doi.org/10.1088/0266-5611/14/4/001

Barboux, C., Delaloye, R., Lambiel, C., 2014. Inventorying slope movements in an Alpine environment using DInSAR. Earth Surf. Process. Landforms 39, 2087–2099. https://doi.org/10.1002/esp.3603

Barboux, C., Strozzi, T., Delaloye, R., Wegmüller, U., Collet, C., 2015. Mapping slope movements in Alpine environments using TerraSAR-X interferometric methods. ISPRS J. Photogramm. Remote Sens. 109, 178–192. https://doi.org/10.1016/j.isprsjprs.2015.09.010

Bardi, F., Raspini, F., Ciampalini, A., Kristensen, L., Rouyet, L., Lauknes, T.R., Frauenfelder, R., Casagli, N., 2016. Space-borne and ground-based InSAR data integration: The Åknes test site. Remote Sens. 8. https://doi.org/10.3390/rs8030237

Barsch, D., 1996. Rockglaciers, Indicators for the Permafrost and Former Geoecology in High Mountain Environment, Series in the Physical Environment, 16.

Barsch, D., 1992. Permafrost creep and rockglaciers. Permafr. Periglac. Process. 3, 175–188. https://doi.org/10.1002/PPP.3430030303

Bartsch, A., Grosse, G., Kääb, A., Westermann, S., Strozzi, T., Wiesmann, A., Duguay, C., Seifert, F.M., Obu, J., Goler, R., 2016. GLOBPERMAFROST-HOW SPACE-BASED EARTH OBSERVATION SUPPORTS UNDERSTANDING OF PERMAFROST. Eur. Sp. Agency 9–13.

Bauer, a, Paar, G., Kaufmann, V., 2003. Terrestrial laser scanning for rock glacier monitoring. Proc. 8th Int. Conf. Permafrost, Zurich 1, 55–60.

Berardino, P., Fornaro, G., Lanari, R., Sansosti, E., 2002. A new algorithm for surface deformation monitoring based on small baseline differential SAR interferograms. IEEE Trans. Geosci. Remote Sens. 40, 2375–2383. https://doi.org/10.1109/TGRS.2002.803792

Bergstedt, H., Zwieback, S., Bartsch, A., Leibman, M., 2018. Dependence of C-Band Backscatter on Ground Temperature, Air Temperature and Snow Depth in Arctic Permafrost Regions. Remote Sens. 10, 142. https://doi.org/10.3390/rs10010142

Berthling, I., 2011. Beyond confusion: Rock glaciers as cryo-conditioned landforms. Geomorphology 131, 98–106. https://doi.org/10.1016/J.GEOMORPH.2011.05.002

Blöthe, J.H., Rosenwinkel, S., Höser, T., Korup, O., 2019. Rock-glacier dams in High Asia. Earth Surf. Process. Landforms 44, 808–824. https://doi.org/10.1002/esp.4532

Bodin, X., Krysiecki, J.-M., Schoeneich, P., Le Roux, O., Lorier, L., Echelard, T., Peyron, M., Walpersdorf, A., 2017. The 2006 Collapse of the Bérard Rock Glacier (Southern French Alps). Permafr. Periglac. Process. 28, 209–223. https://doi.org/10.1002/ppp.1887

Bosson, J.-B., Lambiel, C., 2016. Internal Structure and Current Evolution of Very Small Debris-Covered Glacier Systems Located in Alpine Permafrost Environments. Front. Earth Sci. 4. https://doi.org/10.3389/feart.2016.00039

Brardinoni, F., Scotti, R., Sailer, R., Tonidandel, D., 2018. Sources of uncertainty and variability in rock glacier inventories, in: 5th European Conference on Permafrost - EUCOP5. p. 388.

Brighenti, S., Tolotti, M., Bruno, M.C., Engel, M., Wharton, G., Cerasino, L., Mair, V., Bertoldi, W., 2019. After the peak water: the increasing influence of rock glaciers on alpine river systems. Hydrol. Process. 33, 2804–2823. https://doi.org/10.1002/hyp.13533

Buchli, T., Kos, A., Limpach, P., Merz, K., Zhou, X., Springman, S.M., 2018. Kinematic investigations on the Furggwanghorn Rock Glacier, Switzerland. Permafr. Periglac. Process. 29, 3–20. https://doi.org/10.1002/PPP.1968

Buchli, T., Merz, K., Zhou, X., Kinzelbach, W., Springman, S.M., 2013. Characterization and Monitoring of the Furggwanghorn Rock Glacier, Turtmann Valley, Switzerland: Results from 2010 to 2012. Vadose Zo. J.

12, 0. https://doi.org/10.2136/vzj2012.0067

Burn, C.R., 1998. The active layer: two contrasting definitions. Permafr. Periglac. Process. 9, 411–416. https://doi.org/10.1002/(SICI)1099-1530(199810/12)9:4<411::AID-PPP292>3.0.CO;2-6

Cicoira, A., Beutel, J., Faillettaz, J., Vieli, A., 2019. Water controls the seasonal rhythm of rock glacier flow. Earth Planet. Sci. Lett. 528, 115844. https://doi.org/10.1016/J.EPSL.2019.115844

Colucci, R.R., Boccali, C., Žebre, M., Guglielmin, M., 2016. Rock glaciers, protalus ramparts and pronival ramparts in the south-eastern Alps. Geomorphology 269, 112–121. https://doi.org/10.1016/j.geomorph.2016.06.039

Corbane, C., Lemoine, G., Pesaresi, M., Kemper, T., Sabo, F., Ferri, S., Syrris, V., 2018. Enhanced automatic detection of human settlements using Sentinel-1 interferometric coherence. Int. J. Remote Sens. 39, 842–853. https://doi.org/10.1080/01431161.2017.1392642

Corsini, A., Farina, P., Antonello, G., Barbieri, M., Casagli, N., Coren, F., Guerri, L., Ronchetti, F., Sterzai, P., Tarchi, D., 2006. Space-borne and ground-based SAR interferometry as tools for landslide hazard management in civil protection. Int. J. Remote Sens. 27, 2351–2369. https://doi.org/10.1080/01431160600554405

Cremonese, E., Gruber, S., Phillips, M., Pogliotti, P., Boeckli, L., Noetzli, J., Suter, C., Bodin, X., Crepaz, A., Kellerer-Pirklbauer, A., Lang, K., Letey, S., Mair, V., Morra Di Cella, U., Ravanel, L., Scapozza, C., Seppi, R., Zischg, A., 2011. Brief communication: "An inventory of permafrost evidence for the European Alps." Cryosphere 5, 651–657. https://doi.org/10.5194/tc-5-651-2011

Crosetto, M., Monserrat, O., Cuevas-González, M., Devanthéry, N., Crippa, B., 2016. Persistent Scatterer Interferometry: A review. ISPRS J. Photogramm. Remote Sens. https://doi.org/10.1016/j.isprsjprs.2015.10.011

Delaloye, R., Lambiel, C., Gärtner-Roer, I., 2010. Overview of rock glacier kinematics research in the Swiss Alps. Geogr. Helv. 65, 135–145. https://doi.org/10.5194/gh-65-135-2010

Delaloye, R., Morard, S., Barboux, C., Abbet, D., Gruber, V., Riedo, M., Gachet, S., 2012. Rapidly moving rock glaciers in Mattertal. Jahrestagung der Schweizerischen Geomorphol. Gesellschaft 21–31.

Dematteis, N., Giordan, D., Zucca, F., Luzi, G., Allasia, P., 2018. 4D surface kinematics monitoring through terrestrial radar interferometry and image cross-correlation coupling. ISPRS J. Photogramm. Remote Sens. 142, 38–50. https://doi.org/10.1016/J.ISPRSJPRS.2018.05.017

Dematteis, N., Luzi, G., Giordan, D., Zucca, F., Allasia, P., 2017. Monitoring Alpine glacier surface deformations with GB-SAR. Remote Sens. Lett. 8, 947–956.

https://doi.org/10.1080/2150704X.2017.1335905

Falaschi, D., Tadono, T., Masiokas, M., 2015. Rock glaciers in the patagonian andes: an inventory for the monte san lorenzo (cerro cochrane) massif, 47° s. Geogr. Ann. Ser. A, Phys. Geogr. 97, 769–777. https://doi.org/10.1111/geoa.12113

Ferretti, A., Prati, C., Rocca, F., 2001. Permanent scatterers in SAR interferometry. IEEE Trans. Geosci. Remote Sens. 39, 8–20. https://doi.org/10.1109/36.898661

Ferretti, A., Prati, C., Rocca, F., 2000. Nonlinear subsidence rate estimation using permanent scatterers in differential SAR interferometry. IEEE Trans. Geosci. Remote Sens. 38, 2202–2212. https://doi.org/10.1109/36.868878

Frauenfelder, R., Kääb, A., 2000. Towards a palaeoclimatic model of rock-glacier formation in the Swiss Alps. Ann. Glaciol. 31, 281–286. https://doi.org/10.3189/172756400781820264

Groh, T., Blöthe, J.H., 2019. Rock Glacier Kinematics in the Kaunertal, Ötztal Alps, Austria. Geosciences 9, 373. https://doi.org/10.3390/geosciences9090373

Gupta, M R, Chen, Y, Gupta, Maya R, Chen, Yihua, 2011. Theory and Use of the EM Algorithm. Found. Trends R Signal Process. 4, 223–296. https://doi.org/10.1561/2000000034

Haeberli, W., 1985. Creep of mountain permafrost: internal structure and flow of alpine rock glaciers. Mitteilungen der Versuchsanstalt fur Wasserbau, Hydrol. und Glaziologie an der ETH Zurich 77.

Haeberli, W., Hallet, B., Arenson, L., Elconin, R., Humlum, O., Kääb, A., Kaufmann, V., Ladanyi, B., Matsuoka, N., Springman, S., Mühll, D.V., 2006. Permafrost creep and rock glacier dynamics. Permafr. Periglac. Process. 17, 189–214. https://doi.org/10.1002/ppp.561

Harbor, J., Sharp, M., Copland, L., Hubbard, B., Nienow, P., Mair, D., 1997. Influence of subglacial drainage conditions on the velocity distribution within a glacier cross section. Geology 25, 739. https://doi.org/10.1130/0091-7613(1997)025<0739:IOSDCO>2.3.CO;2

Hausmann, H., Krainer, K., Brückl, E., Mostler, W., 2007. Internal structure and ice content of Reichenkar rock glacier (Stubai Alps, Austria) assessed by geophysical investigations. Permafr. Periglac. Process. 18, 351–367. https://doi.org/10.1002/ppp.601

Hooper, A., Zebker, H., Segall, P., Kampes, B., 2004. A new method for measuring deformation on volcanoes and other natural terrains using InSAR persistent scatterers. Geophys. Res. Lett. 31. https://doi.org/10.1029/2004GL021737

Hu, J., Li, Z.W., Ding, X.L., Zhu, J.J., Zhang, L., Sun, Q., 2014. Resolving three-dimensional surface

displacements from InSAR measurements: A review. Earth Sci. Rev. 133, 1–17. https://doi.org/10.1016/j.earscirev.2014.02.005

Ikeda, A., Matsuoka, N., 2002. Degradation of talus-derived rock glaciers in the Upper Engadin, Swiss Alps. Permafr. Periglac. Process. 13, 145–161. https://doi.org/10.1002/ppp.413

Ikeda, A., Matsuoka, N., Kääb, A., 2008. Fast deformation of perennially frozen debris in a warm rock glacier in the Swiss Alps: An effect of liquid water. J. Geophys. Res. 113, F01021. https://doi.org/10.1029/2007JF000859

Jones, D.B., Harrison, S., Anderson, K., Betts, R.A., 2018a. Mountain rock glaciers contain globally significant water stores. Sci. Rep. 8, 2834. https://doi.org/10.1038/s41598-018-21244-w

Jones, D.B., Harrison, S., Anderson, K., Selley, H.L., Wood, J.L., Betts, R.A., 2018b. The distribution and hydrological significance of rock glaciers in the Nepalese Himalaya. Glob. Planet. Change 160, 123–142. https://doi.org/10.1016/j.gloplacha.2017.11.005

Jones, D.B., Harrison, S., Anderson, K., Whalley, W.B., 2019. Rock glaciers and mountain hydrology: A review. Earth-Science Rev. https://doi.org/10.1016/J.EARSCIREV.2019.04.001

Kaab, A., 2000. Photogrammetry for early recognition of high mountain hazards: New techniques and applications. Phys. Chem. Earth, Part B Hydrol. Ocean. Atmos. 25, 765–770. https://doi.org/10.1016/S1464-1909(00)00099-X

Kääb, A., Frauenfelder, R., Roer, I., 2007. On the response of rockglacier creep to surface temperature increase. Glob. Planet. Change 56, 172–187. https://doi.org/10.1016/J.GLOPLACHA.2006.07.005

Kääb, A., Huggel, C., Fischer, L., Guex, S., Paul, F., Roer, I., Salzmann, N., Schlaefli, S., Schmutz, K., Schneider, D., 2005. Remote sensing of glacier-and permafrost-related hazards in high mountains: an overview. Geosci. Union 5, 527–554.

Kääb, A., Kaufmann, V., Ladstädter, R., Eiken, T., 2003. Rock glacier dynamics : implications from high-resolution measurements of surface velocity fields. Permafrost 501–506.

Kääb, A., Vollmer, M., 2000. Surface geometry, thickness changes and flow fields on creeping mountain permafrost: Automatic extraction by digital image analysis. Permafr. Periglac. Process. 11, 315–326. https://doi.org/10.1002/1099-1530(200012)11:4<315::AID-PPP365>3.0.CO;2-J

Kääb, A., Weber, M., 2004. Development of transverse ridges on rock glaciers: field measurements and laboratory experiments. Permafr. Periglac. Process. 15, 379–391. https://doi.org/10.1002/ppp.506

Kellerer-Pirklbauer, A., Delaloye, R., Lambiel, C., Gärtner-Roer, I., Kaufmann, V., Scapozza, C., Krainer, K.,

Staub, B., Thibert, E., Bodin, X., 2018. Interannual variability of rock glacier flow velocities in the European Alps, in: 5th European Conference on Permafrost, June 2018, Chamonix, France. pp. 396–397.

Kellerer-Pirklbauer, A., Kaufmann, V., 2012. About the relationship between rock glacier velocity and climate parameters in central Austria. Austrian J. Earth Sci. 105, 94–112.

Kenner, R., Magnusson, J., 2017. Estimating the Effect of Different Influencing Factors on Rock Glacier Development in Two Regions in the Swiss Alps. Permafr. Periglac. Process. 28, 195–208. https://doi.org/10.1002/ppp.1910

Kenner, R., Phillips, M., Beutel, J., Hiller, M., Limpach, P., Pointner, E., Volken, M., 2017. Factors Controlling Velocity Variations at Short-Term, Seasonal and Multiyear Time Scales, Ritigraben Rock Glacier, Western Swiss Alps. Permafr. Periglac. Process. 684, 675–684. https://doi.org/10.1002/ppp.1953

Kenner, R., Pruessner, L., Beutel, J., Limpach, P., Phillips, M., 2019. How rock glacier hydrology, deformation velocities and ground temperatures interact: Examples from the Swiss Alps. Permafr. Periglac. Process. ppp.2023. https://doi.org/10.1002/ppp.2023

Kenyi, L.W., Kaufmann, V., 2003. Estimation of rock glacier surface deformation using sar interferometry data. IEEE Trans. Geosci. Remote Sens. 41, 1512–1515. https://doi.org/10.1109/TGRS.2003.811996

Klees, R., Massonnet, D., 1998. Deformation measurements using SAR interferometry: potential and limitations. Geol. en Mijnb. 77, 161–176. https://doi.org/10.1023/A:1003594502801

Krainer, K., Bressan, D., Dietre, B., Haas, J.N., Hajdas, I., Lang, K., Mair, V., Nickus, U., Reidl, D., Thies, H., Tonidandel, D., 2015. A 10,300-year-old permafrost core from the active rock glacier Lazaun, southern Ötztal Alps (South Tyrol, northern Italy). Quat. Res. (United States) 83, 324–335. https://doi.org/10.1016/j.yqres.2014.12.005

Krainer, K., Ribis, M., 2012. A Rock Glacier Inventory of the Tyrolean Alps (Austria). Austrian J. Earth Sci. 105/2, 32–47.

Lambiel, C., Delaloye, R., 2004. Contribution of real-time kinematic GPS in the study of creeping mountain permafrost: examples from the Western Swiss Alps. Permafr. Periglac. Process. 15, 229–241. https://doi.org/10.1002/ppp.496

Lambiel, C., Delaloye, R., Strozzi, T., Lugon, R., Raetzo, H., 2008. ERS InSAR for Assessing Rock Glacier Activity, in: 9th Int. Conf. Permafrost. pp. 1019–1025.

Land Use Information System South Tyrol [WWW Document], n.d. URL http://geoportale.retecivica.bz.it/geodati.asp

Lee, S.-K., Kugler, F., Papathanassiou, K.P., Hajnsek, I., 2013. Quantification of Temporal Decorrelation Effects at L-Band for Polarimetric SAR Interferometry Applications. IEEE J. Sel. Top. Appl. Earth Obs. Remote Sens. 6, 1351–1367. https://doi.org/10.1109/JSTARS.2013.2253448

Leprince, S., Barbot, S., Ayoub, F., Avouac, J.-P., 2007. Automatic and Precise Orthorectification, Coregistration, and Subpixel Correlation of Satellite Images, Application to Ground Deformation Measurements. IEEE Trans. Geosci. Remote Sens. 45, 1529–1558. https://doi.org/10.1109/TGRS.2006.888937

LIU, L., JIANG, L., SUN, YONGLING, WANG, H., SUN, YAFEI, XU, H., 2019. Diurnal fluctuations of glacier surface velocity observed with terrestrial radar interferometry at Laohugou No. 12 Glacier, western Qilian mountains, China. J. Glaciol. 1–10. https://doi.org/10.1017/jog.2019.1

Liu, L., Millar, C.I., Westfall, R.D., Zebker, H.A., 2013. Surface motion of active rock glaciers in the Sierra Nevada, California, USA: inventory and a case study using InSAR. Cryosph. 7, 1109–1119. https://doi.org/10.5194/tc-7-1109-2013

LÓPEZ-MORENO, J.I., ALONSO-GONZÁLEZ, E., MONSERRAT, O., DEL RÍO, L.M., OTERO, J., LAPAZARAN, J., LUZI, G., DEMATTEIS, N., SERRETA, A., RICO, I., SERRANO-CAÑADAS, E., BARTOLOMÉ, M., MORENO, A., BUISAN, S., REVUELTO, J., 2019. Ground-based remote-sensing techniques for diagnosis of the current state and recent evolution of the Monte Perdido Glacier, Spanish Pyrenees. J. Glaciol. 65, 85–100. https://doi.org/10.1017/jog.2018.96

Lugon, R., Stoffel, M., 2010. Rock-glacier dynamics and magnitude–frequency relations of debris flows in a high-elevation watershed: Ritigraben, Swiss Alps. Glob. Planet. Change 73, 202–210. https://doi.org/10.1016/J.GLOPLACHA.2010.06.004

Luzi, G., Pieraccini, M., Mecatti, D., Noferini, L., Guidi, G., Moia, F., Atzeni, C., 2004. Ground-based radar interferometry for landslides monitoring: atmospheric and instrumental decorrelation sources on experimental data. IEEE Trans. Geosci. Remote Sens. 42, 2454–2466. https://doi.org/10.1109/TGRS.2004.836792

Luzi, G., Pieraccini, M., Mecatti, D., Noferini, L., Macaluso, G., Galgaro, A., Atzeni, C., 2006. Advances in ground-based microwave interferometry for landslide survey: a case study. Int. J. Remote Sens. 27, 2331–2350. https://doi.org/10.1080/01431160600554975

Mair V., Zischg A., Krainer K., Stötter J., Zilger J., Belitz K., & L.K., 2008. PROALP Rilevamento e monitoraggio dei fenomeni permafrost. Esperienze della Provincia di Bolzano. Neve e Valanghe 64, 50–59.

Marcer, M., Serrano, C., Brenning, A., Bodin, X., Goetz, J., Schoeneich, P., 2019. Evaluating the

destabilization susceptibility of active rock glaciers in the French Alps. Cryosph. 13, 141–155. https://doi.org/10.5194/tc-13-141-2019

Massonnet, D., Feigl, K.L., 1998. Radar interferometry and its application to changes in the Earth's surface. Rev. Geophys. 36, 441–500. https://doi.org/10.1029/97RG03139

Massonnet, D., Souyris, J.-C., 2008. Imaging with Synthetic Aperture Radar.

Michel, R., Avouac, J.-P., Taboury, J., 1999. Measuring ground displacements from SAR amplitude images: Application to the Landers Earthquake. Geophys. Res. Lett. 26, 875–878. https://doi.org/10.1029/1999GL900138

Monnier, S., Kinnard, C., 2017. Pluri-decadal (1955-2014) evolution of glacier-rock glacier transitional landforms in the central Andes of Chile (30-33 • S). Earth Surf. Dynam 5, 493–509. https://doi.org/10.5194/esurf-5-493-2017

Monserrat, O., Crosetto, M., Luzi, G., 2014. A review of ground-based SAR interferometry for deformation measurement. ISPRS J. Photogramm. Remote Sens. 93, 40–48. https://doi.org/10.1016/J.ISPRSJPRS.2014.04.001

Moon, T.K., 1996. The expectation-maximization algorithm. IEEE Signal Process. Mag. 13, 47–60. https://doi.org/10.1109/79.543975

Moreira, A., Prats-Iraola, P., Younis, M., Krieger, G., Hajnsek, I., Papathanassiou, K.P., 2013. A tutorial on synthetic aperture radar. IEEE Geosci. Remote Sens. Mag. 1, 6–43. https://doi.org/10.1109/MGRS.2013.2248301

Nagler, T., Rott, H., 2000. Retrieval of wet snow by means of multitemporal SAR data. IEEE Trans. Geosci. Remote Sens. 38, 754–765. https://doi.org/10.1109/36.842004

Necsoiu, M., Onaca, A., Wigginton, S., Urdea, P., 2016. Rock glacier dynamics in Southern Carpathian Mountains from high-resolution optical and multi-temporal SAR satellite imagery. Remote Sens. Environ. 177, 21–36. https://doi.org/10.1016/J.RSE.2016.02.025

Noferini, L., Pieraccini, M., Mecatti, D., Macaluso, G., Luzi, G., Atzeni, C., 2006. Long term landslide monitoring by ground-based synthetic aperture radar interferometer. Int. J. Remote Sens. 27, 1893–1905. https://doi.org/10.1080/01431160500353908

Noferini, L., Takayama, T., Pieraccini, M., Mecatti, D., Macaluso, G., Luzi, G., Atzeni, C., 2008. Analysis of Ground-Based SAR Data With Diverse Temporal Baselines. IEEE Trans. Geosci. Remote Sens. 46, 1614–1623. https://doi.org/10.1109/TGRS.2008.916216

Nolan, M., Fatland, D.R., 2003. Penetration depth as a DInSAR observable and proxy for soil moisture. IEEE Trans. Geosci. Remote Sens. 41, 532–537. https://doi.org/10.1109/TGRS.2003.809931

Onaca, A., Ardelean, F., Urdea, P., Magori, B., 2017. Southern Carpathian rock glaciers: Inventory, distribution and environmental controlling factors. Geomorphology 293, 391–404. https://doi.org/10.1016/j.geomorph.2016.03.032

Osmanoğlu, B., Sunar, F., Wdowinski, S., Cabral-Cano, E., 2016. Time series analysis of InSAR data: Methods and trends. ISPRS J. Photogramm. Remote Sens. https://doi.org/10.1016/j.isprsjprs.2015.10.003

Outcalt, S.I., Nelson, F.E., Hinkel, K.M., 1990. The zero-curtain effect: Heat and mass transfer across an isothermal region in freezing soil. Water Resour. Res. 26, 1509–1516. https://doi.org/10.1029/WR026i007p01509

PERMOS reports [WWW Document], n.d. URL http://www.permos.ch/publications.html

Pieraccini, M., Miccinesi, L., 2019. Ground-Based Radar Interferometry: A Bibliographic Review. Remote Sens. 11, 1029. https://doi.org/10.3390/rs11091029

Pontius, R.G., Millones, M., 2011. Death to Kappa: birth of quantity disagreement and allocation disagreement for accuracy assessment. Int. J. Remote Sens. 32, 4407–4429. https://doi.org/10.1080/01431161.2011.552923

Rangecroft, S., Harrison, S., Anderson, K., Magrath, J., Castel, A.P., Pacheco, P., 2014. A First Rock Glacier Inventory for the Bolivian Andes. Permafr. Periglac. Process. 25, 333–343. https://doi.org/10.1002/ppp.1816

Riesen, P., Strozzi, T., Bauder, A., Wiesmann, A., Funk, M., 2011. Short-term surface ice motion variations measured with a ground-based portable real aperture radar Interferometer. J. Glaciol. 57, 53–60. https://doi.org/10.3189/002214311795306718

Rist, A., Phillips, M., 2005. First results of investigations on hydrothermal processes within the active layer above alpine permafrost in steep terrain. Nor. Geogr. Tidsskr. - Nor. J. Geogr. 59, 177–183. https://doi.org/10.1080/00291950510020574

Roer, I., Haeberli, W., Avian, M., Kaufmann, V., Delaloye, R., Lambiel, C., Kääb, A., 2008. Observations and considerations on destabilizing active rock glaciers in the European Alps. Ninth Int. Conf. Permafr. 1505–1510. https://doi.org/10.5167/uzh-6082

Roer, I., Kääb, A., Dikau, R., 2005. Rockglacier acceleration in the Turtmann valley (Swiss Alps): Probable controls. Nor. Geogr. Tidsskr. - Nor. J. Geogr. 59, 157–163. https://doi.org/10.1080/00291950510020655

Roer, I., Nyenhuis, M., 2007. Rockglacier activity studies on a regional scale: comparison of geomorphological mapping and photogrammetric monitoring. Earth Surf. Process. Landforms 32, 1747–1758. https://doi.org/10.1002/esp.1496

Rott, H., Scheuchl, B., Siegel, A., Grasemann, B., 1999. Monitoring very slow slope movements by means of SAR interferometry: A case study from a mass waste above a reservoir in the Otztal Alps, Austria. Geophys. Res. Lett. 26, 1629–1632. https://doi.org/10.1029/1999GL900262

Rott, H., Stuefer, M., Siegel, A., Skvarca, P., Eckstaller, A., 1998. Mass fluxes and dynamics of Moreno Glacier, Southern Patagonia Icefield. Geophys. Res. Lett. 25, 1407–1410. https://doi.org/10.1029/98GL00833

Rouyet, L., Kristensen, L., Derron, M.H., Michoud, C., Blikra, L.H., Jaboyedoff, M., Lauknes, T.R., 2017. Evidence of rock slope breathing using ground-based InSAR. Geomorphology 289, 152–169. https://doi.org/10.1016/j.geomorph.2016.07.005

Rouyet, L., Lauknes, T.R., Christiansen, H.H., Strand, S.M., Larsen, Y., 2019. Seasonal dynamics of a permafrost landscape, Adventdalen, Svalbard, investigated by InSAR. Remote Sens. Environ. 231, 111236. https://doi.org/10.1016/J.RSE.2019.111236

Rudolf, H., Leva, D., Tarchi, D., Sieber, A.J., 1999. A mobile and versatile SAR system, in: IEEE 1999 International Geoscience and Remote Sensing Symposium. IGARSS'99 (Cat. No.99CH36293). IEEE, pp. 592–594. https://doi.org/10.1109/IGARSS.1999.773575

Sánchez-Gámez, P., Navarro, F.J., 2017. Glacier surface velocity retrieval using D-InSAR and offset tracking techniques applied to ascending and descending passes of sentinel-1 data for southern ellesmere ice caps, Canadian Arctic. Remote Sens. https://doi.org/10.3390/rs9050442

Scotti, R., Brardinoni, F., Alberti, S., Frattini, P., Crosta, G.B., 2013. A regional inventory of rock glaciers and protalus ramparts in the central Italian Alps. Geomorphology 186, 136–149. https://doi.org/10.1016/j.geomorph.2012.12.028

Scotti, R., Crosta, G.B., Villa, A., 2017. Destabilisation of Creeping Permafrost: The Plator Rock Glacier Case Study (Central Italian Alps). Permafr. Periglac. Process. 28, 224–236. https://doi.org/10.1002/ppp.1917

Seppi, R., 2019. Personal communication.

Seppi, R., Carton, A., Zumiani, M., Dall'Amico, M., Zampedri, G., Rigon, R., 2012. Inventory, distribution and topographic features of rock glaciers in the southern region of the Eastern Italian Alps (Trentino). Geogr. Fis. e Din. Quat. 35, 185–197. https://doi.org/10.4461/GFDQ.2012.35.17

Seppi, R., Carturan, L., Carton, A., Zanoner, T., Zumiani, M., Cazorzi, F., Bertone, A., Baroni, C., Salvatore, M.C., 2019. Decoupled kinematics of two neighbouring permafrost creeping landforms in the Eastern Italian Alps. Earth Surf. Process. Landforms esp.4698. https://doi.org/10.1002/esp.4698

Simons, M., Rosen, P. a, 2007. Interferometric Synthetic Aperture Radar Geodesy, Treatise on Geophysics. https://doi.org/10.1016/B978-0-12-386874-9.00010-5

Smith, L.C., 2002. Emerging Applications of Interferometric Synthetic Aperture Radar (InSAR) in Geomorphology and Hydrology. Ann. Assoc. Am. Geogr. 92, 385–398. https://doi.org/10.1111/1467-8306.00295

South Tyrol Digital Terrain Model (DTM) [WWW Document], n.d. URL http://geoportale.retecivica.bz.it/geodati.asp

Strozzi, T., Delaloye, R., Kääb, A., Ambrosi, C., Perruchoud, E., Wegmüller, U., 2010. Combined observations of rock mass movements using satellite SAR interferometry, differential GPS, airborne digital photogrammetry, and airborne photography interpretation. J. Geophys. Res. Earth Surf. 115, 1–11. https://doi.org/10.1029/2009JF001311

Strozzi, T., Kääb, A., Frauenfelder, R., 2004. Detecting and quantifying mountain permafrost creep from *in situ* inventory, space-borne radar interferometry and airborne digital photogrammetry. Int. J. Remote Sens. 25, 2919–2931. https://doi.org/10.1080/0143116042000192330

Strozzi, T., Wegmuller, U., Matzler, C., 1999. Mapping wet snowcovers with SAR interferometry. Int. J. Remote Sens. 20, 2395–2403. https://doi.org/10.1080/014311699212083

Summary for Policymakers — Special Report on the Ocean and Cryosphere in a Changing Climate [WWW Document], 2019. URL https://www.ipcc.ch/srocc/chapter/summary-for-policymakers/ (accessed 10.14.19).

Tarayre, H., Massonnet, D., 1996. Atmospheric Propagation heterogeneities revealed by ERS-1 interferometry. Geophys. Res. Lett. 23, 989–992. https://doi.org/10.1029/96GL00622

Tarchi, D., Casagli, N., Fanti, R., Leva, D.D., Luzi, G., Pasuto, A., Pieraccini, M., Silvano, S., 2003. Landslide monitoring by using ground-based SAR interferometry: an example of application to the Tessina landslide in Italy. Eng. Geol. 68, 15–30. https://doi.org/10.1016/S0013-7952(02)00196-5

Terzaghi, K., 1943. Theoretical soil mechanics. Wiley 510.

Touzi, R., Lopes, A., Bruniquel, J., Vachon, P.W., 1999. Coherence estimation for SAR imagery. IEEE Trans. Geosci. Remote Sens. 37, 135–149. https://doi.org/10.1109/36.739146

Van Everdingen, R.O., 1998. Multi-Language Glossary of Permafrost and Related Ground-Ice Terms. International Permafrost Association.

Villarroel, C., Tamburini Beliveau, G., Forte, A., Monserrat, O., Morvillo, M., Villarroel, C.D., Tamburini Beliveau, G., Forte, A.P., Monserrat, O., Morvillo, M., 2018. DInSAR for a Regional Inventory of Active Rock Glaciers in the Dry Andes Mountains of Argentina and Chile with Sentinel-1 Data. Remote Sens. 10, 1588. https://doi.org/10.3390/rs10101588

Vivero, S., Lambiel, C., 2019. Monitoring the crisis of a rock glacier with repeated UAV surveys. Geogr. Helv 74, 59–69. https://doi.org/10.5194/gh-74-59-2019

Wang, T., Jónsson, S., 2015. Improved SAR amplitude image offset measurements for deriving three-dimensional coseismic displacements. IEEE J. Sel. Top. Appl. Earth Obs. Remote Sens. 8, 3271–3278. https://doi.org/10.1109/JSTARS.2014.2387865

Wang, X., Liu, L., Zhao, L., Wu, T., Li, Z., Liu, G., 2017. Mapping and inventorying active rock glaciers in the northern Tien Shan of China using satellite SAR interferometry. Cryosphere 11, 997–1014. https://doi.org/10.5194/tc-11-997-2017

Westermann, S., Peter, M., Langer, M., Schwamborn, G., Schirrmeister, L., Etzelmüller, B., Boike, J., 2017. Transient modeling of the ground thermal conditions using satellite data in the Lena River delta, Siberia. Cryosph. 11, 1441–1463. https://doi.org/10.5194/tc-11-1441-2017

Westoby, M.J., Brasington, J., Glasser, N.F., Hambrey, M.J., Reynolds, J.M., 2012. 'Structure-from-Motion' photogrammetry: A low-cost, effective tool for geoscience applications. Geomorphology 179, 300–314. https://doi.org/10.1016/J.GEOMORPH.2012.08.021

Wirz, V., Gruber, S., Purves, R.S., Beutel, J., Gärtner-Roer, I., Gubler, S., Vieli, A., 2016. Short-term velocity variations at three rock glaciers and their relationship with meteorological conditions. Earth Surf. Dyn. 4, 103–123. https://doi.org/10.5194/esurf-4-103-2016

Yague-Martinez, N., Prats-Iraola, P., Rodriguez Gonzalez, F., Brcic, R., Shau, R., Geudtner, D., Eineder, M., Bamler, R., 2016. Interferometric Processing of Sentinel-1 TOPS Data. IEEE Trans. Geosci. Remote Sens. 54, 2220–2234. https://doi.org/10.1109/TGRS.2015.2497902

Yamamoto, Y., 2015. Instabilities in alpine permafrost. Vdf Hochschulverlag AG an der ETH Zürich.

Yu, C., Li, Z., Penna, N.T., 2018. Interferometric synthetic aperture radar atmospheric correction using a GPS-based iterative tropospheric decomposition model. Remote Sens. Environ. 204, 109–121. https://doi.org/10.1016/J.RSE.2017.10.038

Yu, C., Penna, N.T., Li, Z., 2017. Generation of real-time mode high-resolution water vapor fields from GPS

observations. J. Geophys. Res. Atmos. 122, 2008–2025. https://doi.org/10.1002/2016JD025753

Zebker, H.A., Rosen, P.A., Hensley, S., 1997. Atmospheric effects in interferometric synthetic aperture radar surface deformation and topographic maps. J. Geophys. Res. Solid Earth 102, 7547–7563. https://doi.org/10.1029/96JB03804

Zebker, H.A., Villasenor, J., 1992. Decorrelation in interferometric radar echoes. IEEE Trans. Geosci. Remote Sens. 30, 950–959. https://doi.org/10.1109/36.175330

Zischg, A., Mair, V., Lang, K., 2012. PROALP-KARTIERUNG UND MONITORING VON PERMAFROST IN DER AUTONOMEN PROVINZ BOZEN SÜDTIROL, ITALIEN, in: 12th Congress INTERPRAEVENT 2012. pp. 421–432.

Appendix A

This appendix shows some parts of the Python (2.7) code developed to classify the rock glaciers activity as described in chapter 2.2.2. The input files are the interferograms, the amplitude images, the layover and shadow maps, the rock glacier shapefiles in SAR geometry, and the table containing the land use information of each rock glacier. The output is a table containing the rock glacier classification.

```
import rasterio
import rasterio.mask
import fiona
import os
import pandas as pd
import numpy as np
from scipy import stats
import matplotlib.mlab as mlab
from sklearn.metrics import confusion_matrix
from sklearn.metrics import accuracy_score
import math
import cmath
from __future__ import division
from datetime import date
import matplotlib.pyplot as plt
from matplotlib.colors import LogNorm
from sklearn import mixture
from sklearn.mixture import GMM
import sklearn.metrics
import matplotlib.dates as mdates
pd.set_option('display.expand_frame_repr', False)
## Inputs:
Dphase_folder = #folder containing the interferograms
pwr_folder = #folder containing the amplitude images
mask_folder= #folder containing the layover and shadow mask, and the rock glacier shapefiles
land_use= #table containing the land use information of each rock glacier
##parameters
th_lay= #percentage of maximum layover and shadow inside each rock glacier
th_area= #minimum number of pixel inside each rock glacier

Dphase_list = [f for f in os.listdir(Dphase_folder) if '.enp' not in f]
rg_117= fiona.open(os.path.join(mask_folder,'117_RG_1_slant.shp'), 'r')
rg_168= fiona.open(os.path.join(mask_folder,'168_RG_1_slant.shp'), 'r')
track_list, date_list, id_list, percentualeLayover_list, CC_in,dif_pwr_m,dif_pwr_s, Npixel_list,baseline_list = ([],[],[],[],[],[],[],[],[],[])
shp_px_diversi_list, date2_list,track2_list= ([],[],[])
Nrange=range(0,(len(Dphase_list)))
for i in Nrange:
    D_phase= Dphase_list[i]
    track = int(D_phase.split('_')[0])
    master_data = D_phase.split('_')[1]
    slave_data = D_phase.split('_')[4]
    pwr_M=[f for f in os.listdir(pwr_folder) if '.' not in f and master_data in f and str(track) in f and 'meta' not in f]
    pwr_S=[f for f in os.listdir(pwr_folder) if '.' not in f and slave_data in f and str(track) in f and 'meta' not in f]
    if len(pwr_M)!=1:
        print 'error: more master pwr open', pwr_M
        break
    if len(pwr_S) !=1:
        print 'error: more slave pwr open', pwr_S
        break
    if track==117:
        rg=rg_117
        layover='sentinel1_117_20170705_170645898_IW_SIW1_A_VV_cut_slc_pwr_rsp_geo_ls_mask_rsp'
        superPWR='sentinel1_117_20170822_170648723_IW_SIW1_A_VV_cut_slc_pwr_rsp'
    elif track==168:
```

```
    rg=rg_168
    layover='sentinel1_168_20170727_052600013_IW_SIW1_D_VV_cut_slc_pwr_rsp_geo_ls_mask_rsp'
    superPWR='sentinel1_168_20170814_052634696_IW_SIW1_D_VV_msc_cut_slc_pwr_rsp'
  deltaSAR = date(int(slave_data[:4]), int(slave_data[4:6]), int(slave_data[6:])) - date(int(master_data[:4]), int(master_data[4:6]),
int(master_data[6:]))
  src = rasterio.open(os.path.join(Dphase_folder,D_phase))
  master = rasterio.open(os.path.join(pwr_folder,pwr_M[0]))
  slave = rasterio.open(os.path.join(pwr_folder,pwr_S[0]))
  lay= rasterio.open(os.path.join(mask_folder,layover))
  supermaster = rasterio.open(os.path.join(pwr_folder,superPWR))
  for feat in rg:
    out_image, out_transform = rasterio.mask.mask(src, [feat['geometry']], nodata=-999, crop=True)
    masked_img = out_image.data[0,:,:]
    out_master, out_transform = rasterio.mask.mask(master, [feat['geometry']], nodata=-999, crop=True)
    masked_master = out_master.data[0,:,:]
    out_slave, out_transform = rasterio.mask.mask(slave, [feat['geometry']], nodata=-999, crop=True)
    masked_slave = out_slave.data[0,:,:]
    out_lay, out_transform = rasterio.mask.mask(lay, [feat['geometry']], nodata=-999, crop=True)
    masked_lay = out_lay.data[0,:,:]
    out_Smaster, out_transform = rasterio.mask.mask(supermaster, [feat['geometry']], nodata=-999, crop=True)
    masked_Smaster = out_Smaster.data[0,:,:]
    P = masked_img[masked_img!=out_image.fill_value]
    lay_all = masked_lay[masked_lay!=out_lay.fill_value]
    M=masked_master[masked_master!=out_master.fill_value]
    S=masked_slave[masked_slave!=out_slave.fill_value]
    SM=masked_Smaster[masked_Smaster!=out_Smaster.fill_value]
    if len(P)==len(M)==len(S)==len(lay_all)==len(SM):
      track_list.append(track)
      date_list.append(master_data + '_' + slave_data)
      id_list.append(feat['properties']['FID'])
      baseline_list.append(abs(deltaSAR.days))
      Pv = P[lay_all < 249]
      lay_magg249 = lay_all[lay_all> 249]
      Mv=M[lay_all < 249]
      Sv=S[lay_all < 249]
      SMv=SM[lay_all < 249]
      #computation backscattering differences in decibel
      dif_pwr_m.append(10* math.log10(np.mean(SMv) / np.mean(Mv)))
      dif_pwr_s.append(10* math.log10(np.mean(SMv) / np.mean(Sv)))
      #coherence computation
      Fnumeratore = []
      Mv2 = np.sqrt(Mv)
      Sv2 = np.sqrt(Sv)
      for i, (fase, P_master, P_slave) in enumerate(zip(Pv, Mv2, Sv2)):
        numeratore = P_master * P_slave * (cmath.exp(1j * fase))
        Fnumeratore.append(numeratore)
      numeratore2 = np.mean(Fnumeratore)
      denominatore = cmath.sqrt(np.mean(Mv) * np.mean(Sv))
      gamma = numeratore2 / denominatore
      CC = np.absolute(gamma)
      CC_in.append(CC)
      # computation layover and shadow
      num=len(lay_magg249)
      denom=len(lay_all)
      def foo(num, denom):
        try:
          return num / denom
        except ZeroDivisionError:
          return 0
      percentuale = foo(num, denom)
      percentualeLayover_list.append(percentuale)
      Npixel_list.append(len(Pv))
d_out = {'track':track_list, 'date':date_list, 'id':id_list, 'percentuale_lay':percentualeLayover_list,
     'CC_in': CC_in, 'Npixel':Npixel_list,'intens_master':dif_pwr_m, 'intens_slave':dif_pwr_s,'baseline':baseline_list}
```

```
df = pd.DataFrame(d_out)
df_filt= df[df.percentuale_lay<th_lay]
df_filt=df_filt[df_filt.Npixel>th_area]
df_filt=df_filt[df_filt.CC_in.notnull()]
df_filt=df_filt[df_filt.intens_master.notnull()]
df_filt2=df_filt[df_filt.intens_slave.notnull()]
rows_list = []
for index, row in df_filt2.iterrows():
    if row['date'][4:6]=='09' or row['date'][4:6]=='08' :
        if row['date'][-4:-2]=='09' or row['date'][-4:-2]=='08':
            row['date']
            rows_list.append(row)
df_filt2 = pd.DataFrame(rows_list)
id=df_filt2.id
id2=id.drop_duplicates()
len(id2)
df_filt2['intens_masterAB'] = np.abs(df_filt2.intens_master)
df_filt2['intens_slaveAB'] = np.abs(df_filt2.intens_slave)
df_filt3=df_filt2[0:0]
for b in [6,12,18,24]:
    df_b = df_filt2[df_filt2.baseline == b]
    for i in id2:
        prov=df_b[df_b.id==i]
        #seleziono per ogni rg la track con piu pixel
        lenM=max(prov.Npixel)
        prov=prov[prov.Npixel==lenM]
        if len(prov)>0:
            selez=prov[prov['intens_masterAB']+ prov['intens_slaveAB'] == min(prov['intens_masterAB']+ prov['intens_slaveAB'])]
            df_filt3=pd.concat([df_filt3,selez])
plt.figure()
plt.hist(df_filt3.intens_slave, bins=80)
plt.title('backscattering difference of slave images')
df_veget=pd.read_csv(land_use)
df_filt3=pd.merge(df_filt3,df_veget,on='id', how='left')
df_filt3=df_filt3[np.logical_or(np.logical_and(df_filt3.perc_bosco==0,df_filt3.perc_prato<=0),df_filt3.id>9999)]
id=df_filt3.id
id2=id.drop_duplicates()
#classiifcation
df_filt6=df_filt3[df_filt3.baseline==6]
list_CC=[]
for i in id2:
    list_CC.append([float(df_filt6.CC_in[df_filt6.id==i])])
X_train=np.array(list_CC)
for b in [12,18,24,30,36,42,48,54]:
    df_b = df_filt3[df_filt3.baseline == b]
    list_CC = []
    for i in id2:
        list_CC.append([float(df_b.CC_in[df_b.id == i])])
    CCarr = np.array(list_CC)
    X_train=np.c_[X_train, CCarr]
gmm = mixture.GaussianMixture(n_components=2).fit(X_train)
labels = gmm.predict(X_train)
probs=gmm.predict_proba(X_train)
classi=[]
for f in labels:
    if f==0:
        classi.append('F')
    else:
        classi.append('A')
probab=probs[:,1]
probab=probab.round(4)
dict={'id':id2, 'CCclass':classi,'prob':probab}
df_classi=pd.DataFrame(dict)
```

Appendix B

Concerning the GB-SAR data processing (chapter 3), several tests were conducted to optimize the processing, especially the data selection. In detail, the data selection described in section 3.2.2 was developed by evaluating the results of the cumulative displacement of time series. This appendix shows the August 2018 time series obtained from different data selection procedures. The cumulative displacements inside the rock glacier and outside on stable areas are shown in the following graphs, including also the air temperature, the instrument temperature measured inside the radar head and the spring water temperature.

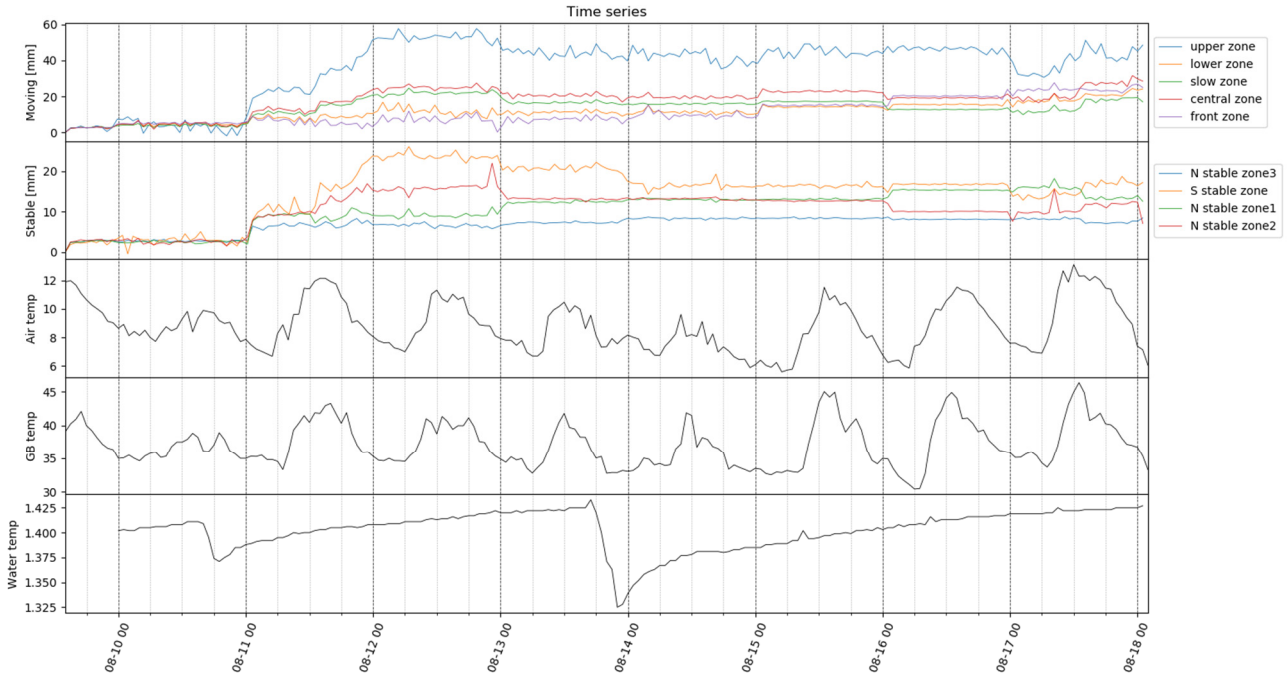

Figure B.1: time series obtained from the GB-SAR processing without data selection. All the images are used. Interferograms are computed through coherent sums of stacks of 11 images. Strong noise on stable areas is visible.

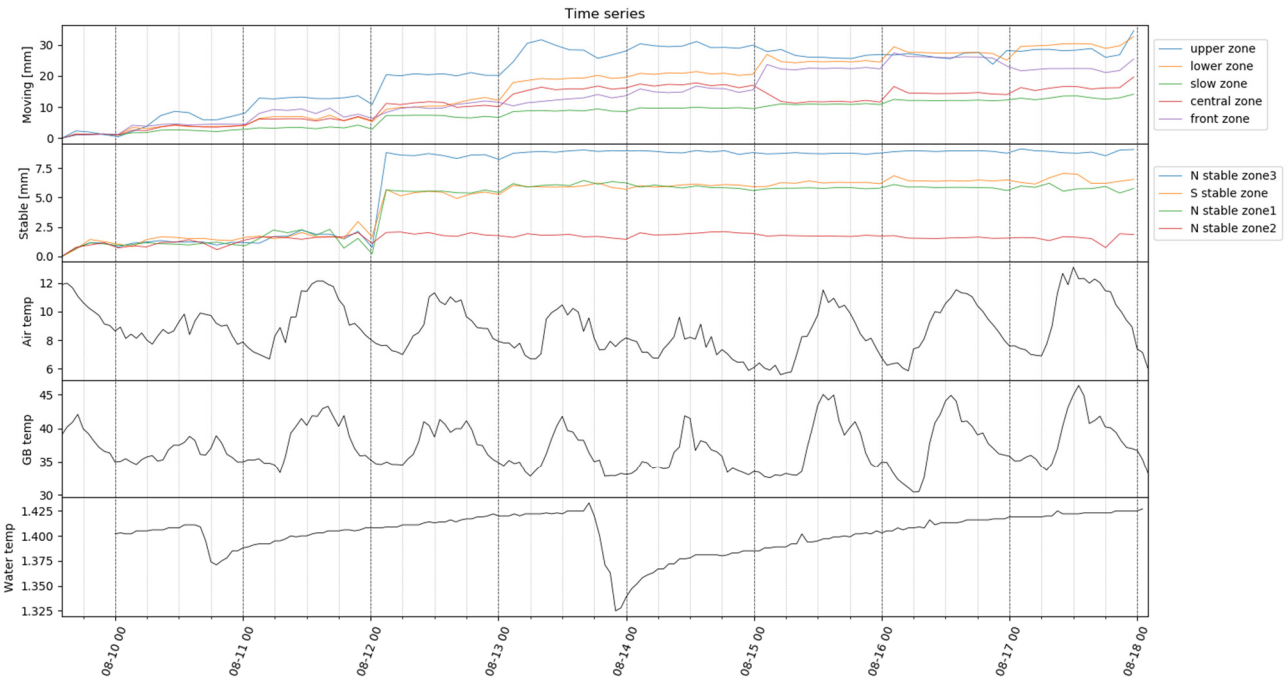

Figure B.2: time series obtained from the GB-SAR processing without data selection. All the images are used. Interferograms are computed through coherent sums of stacks of 30 images. Strong noise on stable areas is visible.

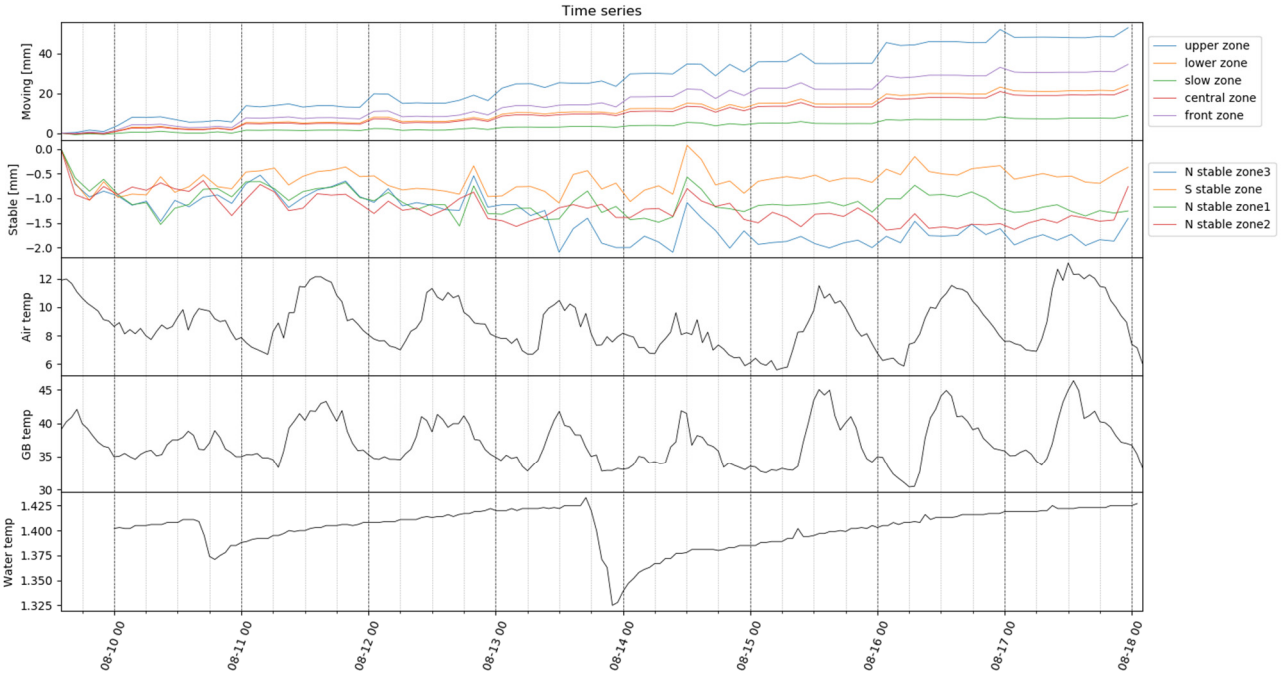

Figure B.3: time series obtained from the GB-SAR processing with data selection. The data section is conducted as described in section 3.2.2. However, stacks of 30 images are taken into account, and the coherent sum is not computed. The master image of the selected interferogram for each stack of 30 images is used to compute the final interferograms. Noise on stable areas is strongly reduced, and the "step-like" cumulative displacement inside the rock glacier is visible.

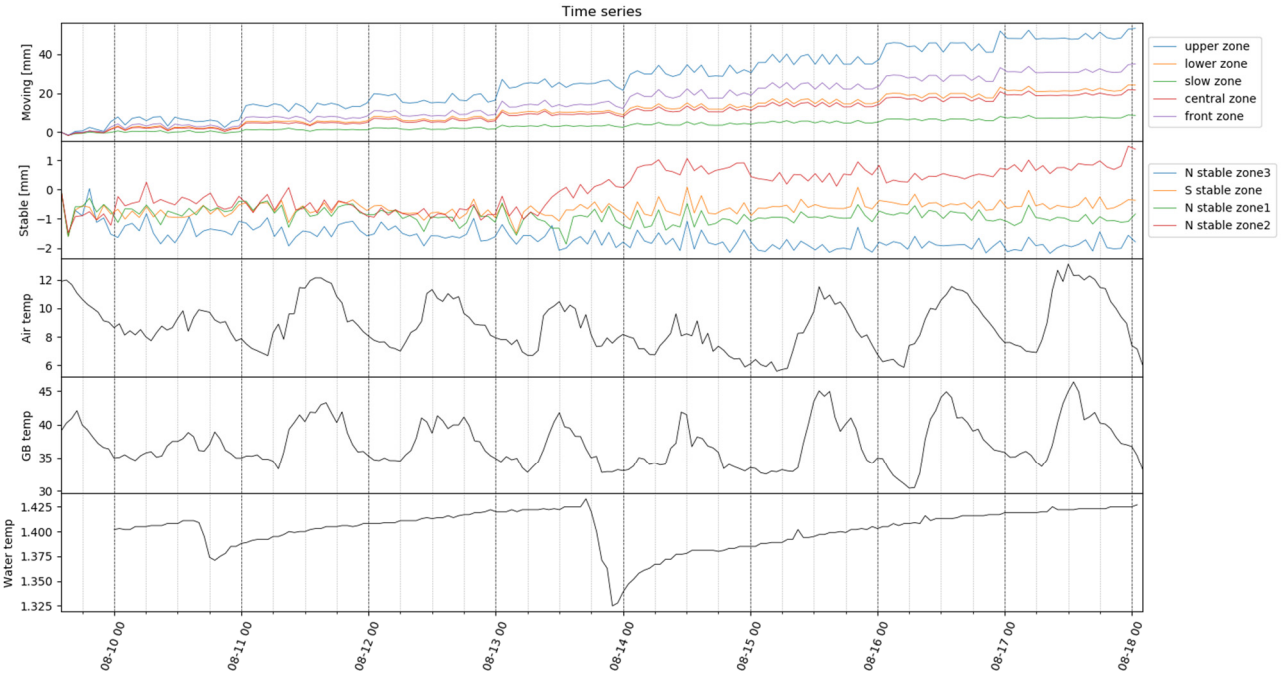

Figure B.4: time series obtained from the GB-SAR processing with data selection. The data section is conducted as described in section 3.2.2. However, stacks of 12 images are taken into account, and the coherent sum is not computed. The master image of the selected interferogram for each stack of 12 images is used to compute the final interferograms. Noise on stable areas is strongly reduced, and the "step-like" cumulative displacement inside the rock glacier is visible.

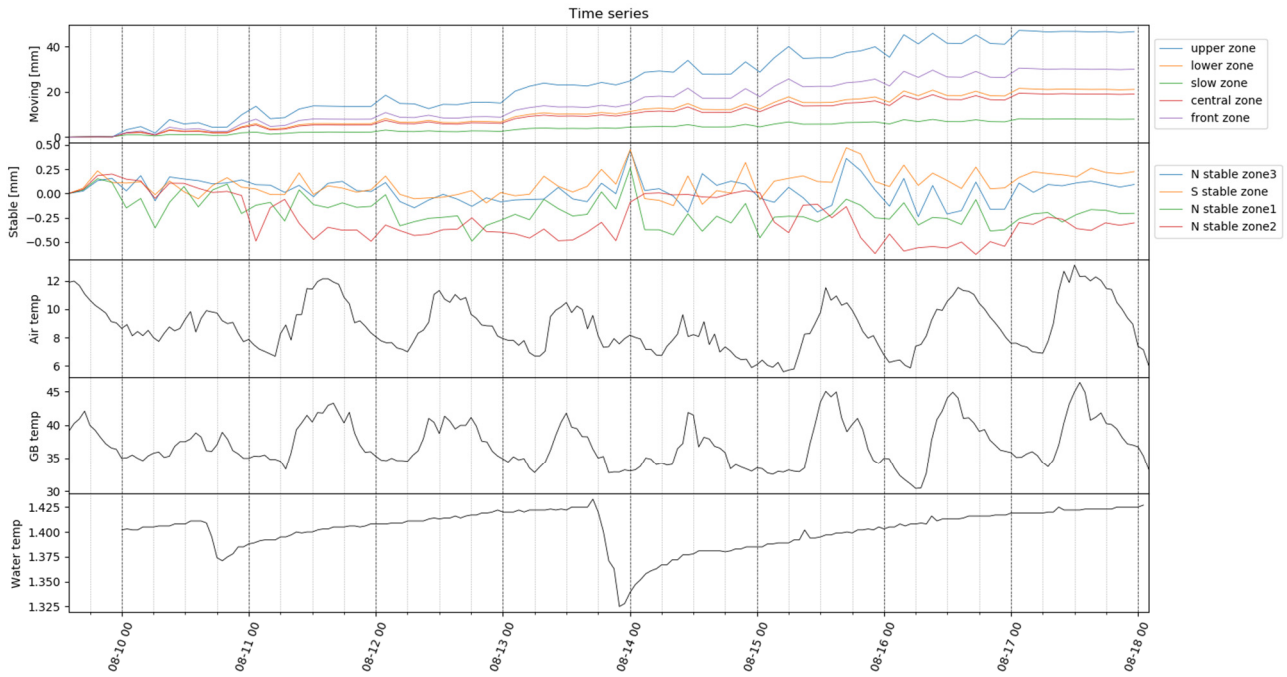

Figure B.5: time series obtained from the GB-SAR processing with data selection as described in section 3.2.2. The data section is conducted on stacks of 30 images. Noise on stable areas is further reduced, and the "step-like" cumulative displacement inside the rock glacier is visible.

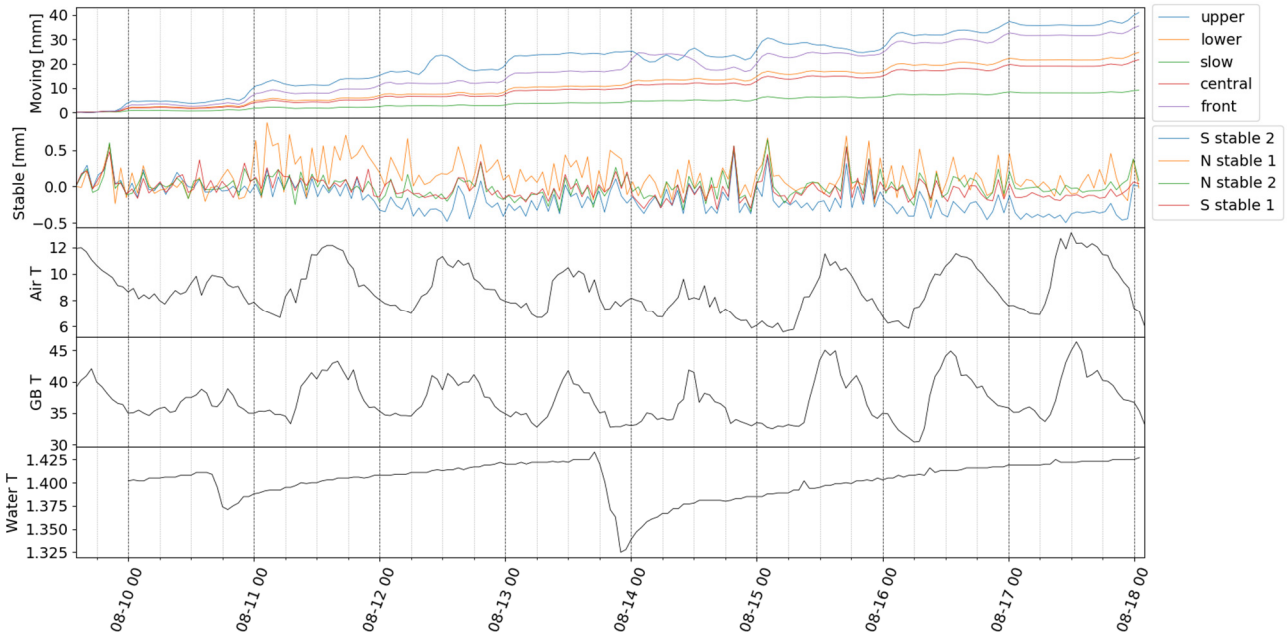

Figure B.6: time series obtained from the GB-SAR processing with data selection as described in section 3.2.2. The data section is conducted on stacks of 12 images. Noise on stable areas is further reduced, and the "step-like" cumulative displacement inside the rock glacier is visible.